Günter Krois, BSc.

Heavy Alkali and Alkaline Earth Metals on Cold Helium Droplets: First Comparison of Excitation Spectra

MASTER THESIS

For obtaining the academic degree
Diplom-Ingenieur

Master Programme of
Technical Physics

Graz University of Technology

Graz University of Technology

Supervisor:
Univ.-Prof. Mag. Dr.rer.nat. Wolfgang E. Ernst
Institute for Experimental Physics

Graz, September 2011

Zusammenfassung

Helium Nanotröpfchen stellen aufgrund ihrer außerordentlichen Eigenschaften, sie sind ultrakalt und suprafluid, eine einzigartige spektroskopische Umgebung dar. Zusätzlich erlauben Helium Nanotröpfchen vielfältige Pickup Möglichkeiten für den Einfang und die Untersuchung einzelner Fremd-Teilchen. Die vorliegende Arbeit widmete sich drei Aufgaben: Als erstes wurden Cäsium dotierte Heliumtröfchen mit Hilfe von resonanter drei Photonen Ionisations Flugzeit Massenspektroskopie untersucht. Als zweites Ziel wurde eine Pickupzelle inklusive Heizung und thermischer Abschirmung für den Pickup von Erdalkalielementen entworfen, gebaut und bis zu einer Temperatur von 520 °C getestet. Das neue Pickup System wurde anschließend erfolgreich in die bestehende Anlage eingebaut. Als letzte Aufgabe wurde diese Pickupzelle getestet indem mit ihrer Hilfe He Nanotröpfchen mit Strontium dotiert und anschließend untersucht wurden.

Abstract

Helium nanodroplets provide a unique spectroscopic environment due to their special characteristics: they are ultracold and superfluid. Furthermore they provide a confinement to isolate single particles and versatile pickup possibilities. This work had three objectives: Cs-doped He nanodroplets were investigated with spectroscopic techniques involving resonant three photon ionization and detection via time-of-flight mass spectrometry. As a second goal a new pickup cell, including its heating and shielding was designed, constructed, characterized to reach up to 520 °C. The new pickup system was successfully installed into the existing setup. Finally this pickup cell was tested by doping the helium nanodroplets with strontium atoms and investigating them with mass spectrometry and resonant two step ionization.

Deutsche Fassung:
Beschluss der Curricula-Kommission für Bachelor-, Master- und Diplomstudien vom 10.11.2008
Genehmigung des Senates am 1.12.2008

EIDESSTATTLICHE ERKLÄRUNG

Ich erkläre an Eides statt, dass ich die vorliegende Arbeit selbstständig verfasst, andere als die angegebenen Quellen/Hilfsmittel nicht benutzt, und die den benutzten Quellen wörtlich und inhaltlich entnommene Stellen als solche kenntlich gemacht habe.

Graz, am …………………………… ………………………………………………..
(Unterschrift)

Englische Fassung:

STATUTORY DECLARATION

I declare that I have authored this thesis independently, that I have not used other than the declared sources / resources, and that I have explicitly marked all material which has been quoted either literally or by content from the used sources.

…………………………… ………………………………………………..
date (signature)

Contents

CHAPTER 1

Introduction

Helium nanodroplets provide a close to perfect matrix to investigate various species, because they are ultra-cold (0.38 K) and superfluid, hence their interaction with the investigated species (guests) is very small. Spectroscopy of doped He nanodroplets is still a young technique, it was first developed in the 1990's and the effects of the helium droplets on their guests are still being investigated. Alkali (Ak) metals provide, due to their simple and well known structure, a good testing ground. Hence, our group has investigated Ak metal doped helium droplets for several years, consistently leading to new and interesting results. Very recently highly excited states of caesium (Cs) doped droplets have been investigated by LIF spectroscopy. In a next step, REMPI-TOF spectroscopy (cf. Chapter 4) was used to excite even higher states of Cs doped droplets up to the ionization threshold. This second step is one part of this thesis and its results are presented in Chapter 5 as well as in [31].

Since the effects of helium droplets on picked up alkali metals are well known by now, it is interesting to look at alkaline earth (Ake) metal doped droplets, which provide the next step in difficulty. Not a lot is known about Ake doped droplets and no highly excited states have been reported up to now. So the second and main goal of this thesis was to design and construct an oven and a pickup cell for Ake metals and to implement both into the existing setup (cf. Chapter 3).
As a last step, the pickup cell was characterized and tested by - for the first time in Graz - doping helium droplets with strontium (Sr) atoms. The results obtained in these experiments are presented in Chapter 7.

In the first Chapter of this work, theoretical background information is provided which is necessary to understand the results of the experiments. The Chapter covers a historical perspective of helium droplets, information about the characteristics of helium and the dopants used in the course of this work (alkali and alkaline earth metals) as well as a description of the generation of helium droplets and a short review of spectroscopic denotation of atoms and diatomic molecules. The Chapters 2 and 3 shortly describe the experimental setup and the detection techniques used. In the subsequent Chapters the results obtained with Cs doped helium droplets, the design and construction of an Ake metal pickup oven and pickup cell as well as the results obtained with Sr doped helium droplets are presented. Finally, a summary of the work and an outlook to future experiments is given.

CHAPTER 2

Theoretical Background

This Chapter provides a short but thorough overview of the theoretical background necessary to understand the results given in Chapters 5 and 7.
At the beginning a short historical perspective is used to learn how and why spectroscopy on helium nanodroplets was developed. The second Section will deal with helium and superfluidity, while the subsequent Section explains the formation of a helium nanodroplet beam in detail. The fourth Section gives information on spectroscopy of doped helium nanodroplets, focusing on alkaline earth metals. Then a short introduction to diatomic molecules is given, containing information, which is important to understand the results Chapters. The last Section provides insights into the function principles of pulsed lasers, since two of them have been used in the experiments (cf. Chapter 4).

2.1. A Short Historical Approach

In this Section, the reader will be led along the trail of ideas which finally resulted in the experiment of spectroscopy of doped helium nanodroplets. This will inherently demonstrate the advantages of this method and what scientists hope to achieve with it. Large parts of this Section are based on the introduction of André Conjusteau's PhD thesis [9].

Spectroscopy is a very well established method to investigate the basic structure of atoms and molecules. Various forms of this experimental method have been developed since it was first discovered in 1813 by Fraunhofer. However, common spectroscopic methods on atoms or molecules in free space do not allow to investigate unstable species and radicals. Whittle, Dows and Pimentel [69] proposed a solution to this problem in 1954 , following an idea of Vegard [68], who had suggested as early as 1924 that nitrogen caught in an inert gas is expected to behave as in free space. Whittle, Dows an Pimentel described their intentions as follows :

> The matrix isolation method proposed here involves accumulation of a reactive substance under environmental conditions which prevent reaction. The intent of the method is to trap active molecules in a solid matrix of inert material, crystalline or glassy. If the temperature is sufficiently low, the matrix will inhibit diffusion of the trapped molecule, thus holding the active molecules effectively immobile in a non-reactive environment.

They were indeed able to show that molecules which would usually react with each other could be isolated with this method. Thus ‘matrix isolation’ was born.
Milligan and Jacox further advanced the matrix isolation technique in the 1960’s. They used rare-gases as a host matrix and were able to generate and stabilize free-radicals within the matrix [39,40]. Until the 1980’s, ‘matrix isolation spectroscopy’ had - supported by the development of the laser - evolved into a well established method to interrogate various unstable substances and radicals. In modern matrix isolation experiments, the molecules to investigate (guests) are embedded in an inert matrix (host). This is done by mixing the host and guest materials in gas phase and deposit the mixture on a window where it can be investigated spectroscopically. The advantage of matrix isolation spectroscopy is that it allows a long term study of a relatively large quantity of the guest molecules, since they are bound by the stable host matrix. This in turn, allows an interrogation of usually weak transitions. The interaction of the guest molecules with the host matrix provides further possibilities. This interaction causes the selection rules to relax, which allows the investigation of usually forbidden transitions. The main disadvantages of this method are also due to these interactions of the guest molecules with the matrix, which cause the broadened and shifted spectral lines of transitions. In molecules, the rotational transitions can’t be resolved at all and vibrational lines are subject to large shifts.

Due to this disadvantage, the search for less perturbative matrices began. A promising species seemed to be helium: The two isotopes of helium reach there liquid phase only at 3.19 K for ^{3}He and at 4.21 K for ^{4}He and can not be solidified under ambient pressure, due to the weak interaction between the helium atoms. A special characteristic of Helium is that it has a second liquid phase in which it is superfluid. The transition happens at a temperature of 2.2 K for ^{4}He and at 2.6 mK for ^{3}He[1]. Hence using superfluid helium as a matrix would be highly interesting, because the interaction of this matrix with any guest would be as small as possible. Unfortunately, two effects prevent such experiments with the common matrix isolation approach: Mainly due to the very small interaction with the superfluid matrix, the guests are not isolated anymore but aggregate and secondly, due to the same reason, guests adsorb to the vessel walls. In the early 1990’s a way around the problems was found by Goyal, Schutt and Scoles [19, 20], who initially did research on argon clusters. In one kind of experiment, they doped the argon clusters with single molecules. They realized that this idea could be applied to helium as well. If one could dope one cluster or ‘droplet’ of helium[2] with only one guest atom or molecule, the problem of aggregation as well as the problem of adsorption to the vessel walls would be prevented, since there simply would be no other molecules to aggregate and no vessel wall to adsorb to. Hence spectroscopy on helium nanodroplets does effectively combine the advantages of matrix isolation and beam spectroscopy.

2.1.1. Recent Developments

Since the first experiments performed with helium nanodroplets as a host matrix by Goyal, Schutt and Scoles in 1992 [19], important results have been found:

- Rotational structures of guests have been resolved [23].
- The temperature of the droplets was experimentally found to be 0.38 K, independent of the droplet size [23].

---

[1] *Superfluidity* denotes a state of a liquid in which it does not show any viscosity and has infinite thermal conductivity.

[2] *here:* agglomeration of approx. 10^4 helium atoms, in liquid phase

- It was discovered that the effect of superfluidity occurs at a critical minimal cluster size of 60 atoms [22]. This experimental value is very close to the theoretical value of 64 atoms [55].

These are the effects which make helium nanodroplets 'the ultimate spectroscopic matrix' [35]. Due to the droplet temperature of 0.38 K, the guests are in their ground state, which simplifies the spectra. With the additional effect of superfluidity, they 'are the least perturbative matrix imaginable' [9]. The pickup process can be implemented very easily and allows an exact method to dope the droplets with a well controlled number of atoms or molecules.

2.1.2. Spectroscopy on Alkali Metal Doped He Nanodroplets

Alkali (Ak) metals provide a good testing ground for many applications. They have a simple structure and configuration, they are well known experimentally as well as theoretically and they are easy to excite with the help of lasers in the visible range. Hence alkali metals are ideal probands to investigate the effects of helium droplets on dopants.

The Princeton group was the first to dope helium droplets with Ak metals in the early 1990's [8]. They showed that alkali metals reside on the surface of the droplet in a small depression called 'dimple'. This is due to the very low interaction potential of Ak metals with helium. The first optical spectra of Ak metals doped helium droplets were successively presented by Stienkemeier et al. in 1995 [57]. They discovered that the $n^2\text{P} \leftarrow n^2\text{S}$ lines of alkali metals are broadened and shifted, however not as much as the lines of dopants which are immersed into the droplet.

To the present, investigations of alkali doped helium droplets have been performed in several groups, such as ours. Recent findings are that Rb [3] as well as Cs [62] stay on the droplet when excited to their first excited state $5^2\text{P}_{1/2}$ and $6^2\text{P}_{1/2}$, respectively. In one work of our group, Cs doped helium droplets were excited to Rydberg states, detected by LIF and REMPI-TOF spectroscopy and published in [31]. The measuring techniques and results presented in this paper will be treated in the Chapters 4 and 5.

2.1.3. Spectroscopy on Alkaline Earth Metal Doped He Nanodroplets

Alkaline earth (Ake) metals are interesting to investigate on helium nanodroplets because of their interaction with the droplet. While alkali metals are known to reside on the surface of the droplet and most other species are solvated into the center of the droplet, the situation is not unambiguously clear for all Ake metals. The configurations and spectra of Ake metals are well known and they have even been investigated in bulk liquid helium, which provides a good comparison for investigations on helium droplets.

Shortly after it was discovered that alkali metals reside on the surface of helium droplets Stienkemeier et al. performed experiments with alkaline earth metal doped droplets. For calcium, strontium [59] and barium [60], it was found that they also reside on the surface of the helium droplets, although embedded in a deeper dimple. For magnesium, the situation is not unambiguously clear up to present, even though several experiments have been performed [51].

For more detailed information of experiments done with Ake metal doped helium clusters and helium droplets in general see Ref [51] and the review articles Refs [58, 64].

As a summary, it can be said that Ake metal doped helium clusters were investigated in the late 90's until their location on the droplet was thought to be found. Only in recent years, the interest into this matter has been rising again, partly due to new theoretical methods [24, 51]. However, in total, the interactions of alkaline earth metals with helium droplets are not investigated in detail up to present. This is one reason why it was an objective of this thesis to extend the setup of our group to be able to dope helium droplets with alkaline earth metals.

2.2. Helium

Some of the characteristics of helium have already been mentioned in the historical approach above. In this Section we will have a closer look at these.
Helium appears in nature in form of two stable isotopes, ^{3}He and ^{4}He. However, only 0.000137 % of the natural helium are ^{3}He. To use it in experiments, this isotope has to be produced in a radioactive process, hence it is rare, expensive and hardly used in experiments. This also applies to experiments within this work. Since only ^{4}He has been used, in the remainder of this thesis, the term 'helium' always refers to this isotope if not denoted otherwise.

Helium is a special material. The de Broglie wavelength of helium at its boiling point under ambient pressure (4.22 K) lies in the range of the average atom distance between two helium atoms in a He_2 molecule (which is only true for helium). Due to this, helium shows quantum mechanical characteristics such as superfluidity. The special characteristics of helium can be seen in a phase diagram (cf. Figure 2.1). The evaporation point of ^{4}He is at 4.21 K. For ambient pressure, however, there is no melting point, because helium can not be solidified below a pressure of 25 bar, due to the weak interaction between the helium atoms. Helium has two liquid phases called Helium I and II, where the latter is the superfluid phase. The transition between the two phases is called λ-transition. For ^{4}He the transition happens at a temperature of 2.174 K at ambient pressure (for ^{3}He only at 2.6 mK).

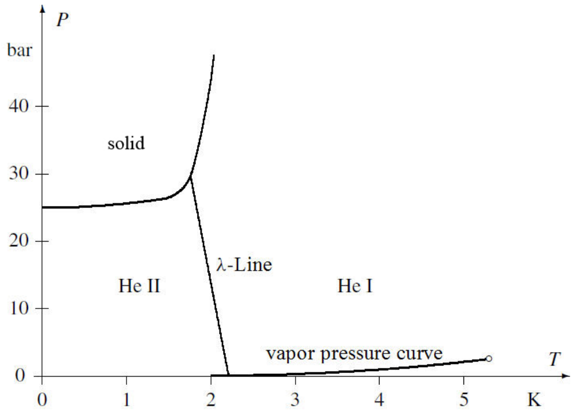

Figure 2.1.: Phase diagram of ^{4}He. Helium can not be solidified at a pressure below 25 bar and becomes superfluid at the so-called λ-transition, at 2.174 K (values given for ^{4}He, graphic modified from [15]).

2.2.1. Superfluidity

As mentioned above, superfluidity denotes a second liquid phase, in which the liquid does not have any viscosity and infinite heat conductivity. This phase is only well known for helium (^{3}He and ^{4}He) [1, 25]. However, there are theories and experiments which indicate a superfluid phase for H [21] and ^{6}Li [26]. In this Section, some information about the superfluid phase of ^{4}He will be presented, since the helium droplets used in the experiments below consist of this element.

^{4}He behaves like a common liquid for temperature above the λ-transition[3], which is at a temperature of 2.174 K (cf. Figure 2.1). Several theories deal with the description of superfluidity. The two-fluid model, formulated by Tisza [65] and Landau [33], states that He II is a mixture

---

[3] The transition is named after the λ shaped singularity in the specific heat at the transition.

of superfluid and normal helium, where the fraction of superfluid helium increases when the temperature decreases. Purely superfluid helium is only reached for $T = 0\,\mathrm{K}$. This explains why a torsion pendulum rotating in superfluid helium experiences friction while superfluid helium flowing through a capillary seems not to[4].

The quasi-particle model by Landau [33] is an expansion of the model above. As its name implies, it explains the phenomenon of superfluidity with the help of quasi-particles. It is only valid for a temperature range $\leq 1\,\mathrm{K}$ and breaks down at the λ transition. A simple way to describe this model has been reported by Feynman in Ref [14]: At $T = 0\,\mathrm{K}$ He behaves like a perfectly superfluid liquid. If we it heat up, the heat energy excites the helium. The quasi-particles involved in the excitation are - depending on their energy - called phonons, maxons or rotons. At lower energies, the excitations are few and will stay mainly within the liquid - it will still flow through a capillary without experiencing any viscosity, while some viscosity will show when a torsion pendulum is rotating in it. The dispersion curve of liquid helium is shown in Figure 2.2. The first part is linear, which indicates that sound waves (phonons) are excited at the lowest energies. The quasi-particles in the area of the maximum are called 'maxons' and those close to the minimum are called 'rotons'. If an object is flowing through superfluid helium, the only way for the object to transfer energy to the helium is by exciting it into states around this minimum and maximum, so to excite maxons or rotons. This requires a high velocity. The theory behind this would go beyond the scope of this work, however, the interested reader is referred to Refs [14, 33]. An informative article about the discovery of superfluidity has been written by Donnelly [12, 13].

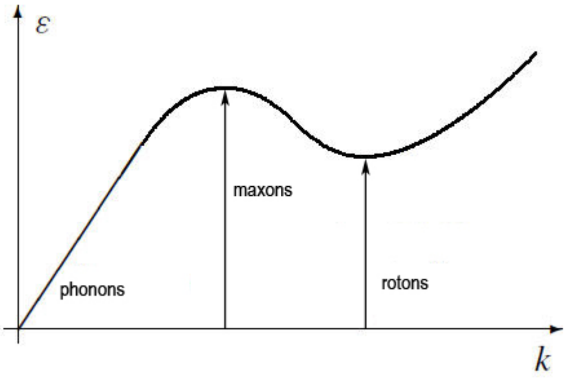

Figure 2.2.: Dispersion relation (energy ϵ as a function of momentum $p = \hbar k$) for ^{4}He with T≤1 K to explain the quasi-particle model of Landau (modified from [15]).

2.3. Helium Nanodroplets

This Section is about generating helium nanodroplets, their manipulation and their characteristics. The most important properties are stated in the beginning. The subsequent Sections describe the generation of He nanodroplets in a supersonic jet expansion in detail, review adiabatic expansion and deal with the formation of clusters, their size distribution and their doping.

---

[4] These experiments denote the discovery of superfluid helium and were published simultaneously by Kapitza [25] and Allen and Misener [1].

The term ‘helium nanodroplet’ is another word for (fluid) helium clusters. ‘Cluster’ denotes an agglomeration of 2 to about 10^5 atoms. They form the connection between atoms and macroscopic objects. The characteristics of a silver atom for example, is very different from a solid silver crystal.

The most important characteristics of helium clusters or nanodroplets used in the experiments below are:

- He nanodroplets consist on average of 10^4 ^{4}He atoms, which corresponds to a size of approx. $r = 50\,\text{Å}$ [66].
- The temperature of a droplet is $0.375\,\text{K}$, independent of the droplet size [23].
- The droplet is superfluid.
- The droplets are fully transparent from IR well into the VUV [8].

2.3.1. Beam Generation

Note: Large parts of this Section are based on [43]. Basically there are two ways to generate an atomic beam:

- Effusive beam: A cell is filled with the desired gas. The pressure outside of the cell is much lower than inside. The gas exits the cell through a small hole (aperture) and expands. With the correct size of aperture and pressure, molecular flow is guaranteed (see below for closer information). Effusive beams are easy to build and do not consume a lot of material. Their theory is well known, hence the parameters can be calculated exactly via kinetic gas theory. The velocity distribution is well defined, but broad and the intensity is rather low.
- Gas dynamic beam: The gas is expanded into vacuum through a small nozzle under high pressure, which leads to a high intensity beam with a narrow velocity distribution. The experimental effort, however, is higher and the parameters can not be calculated exactly. The helium droplets in our experiment are generated by supersonic jet expansion, which is a form of a gas dynamic beam.

Effusive beam

The pickup cell in this experiment is basically an effusive beam source, hence the theory of this method shall be explained shortly. As stated above, one important requirement for effusive beams is the connection between the size of the aperture of the gas cell and the pressure of the gas. We assume to have an ideal aperture, that means the thickness of the aperture is negligible compared to its diameter. We can calculate the parameters of the gas streaming (effusing) through the aperture, if the area of the aperture is small compared to the whole area of the gas cell walls. This ensures that the thermal equilibrium within the cell is maintained, even though the gas is effusing out of the cell. Also the pressure outside the cell has to be low to ensure molecular flow. In other words: The mean free path (Λ) of the gas particles has to be large compared to the diameter of the aperture. If this is the case, no collisions will occur close to the aperture. In this method, the beam is produced under conditions of thermal equilibrium and without collisions, hence it has a well defined velocity distribution, controllable by the temperature within the cell.

The velocity distribution of the gas within the cell is a Maxwell distribution:

$$f_{(v)}dv = 4\pi \left(\frac{m}{2\pi k_B T_0} \right)^{\frac{3}{2}} v^2 \exp - \frac{mv^2}{2k_B T_0} dv, \tag{2.1}$$

with the probability $f_{(v)}dv$ that a particle with mass m has a velocity within the interval $[v, v{+}dv]$. k_B denotes the Boltzmann constant and T_0 the equilibrium temperature.
The velocity distribution of the effusive beam is modified by a factor v, since the probability for a particle to leave the gas cell is proportional to its velocity. For closer explanation see Ref [43, 44, 52, 53].

Free-Jet Expansion

The helium nanodroplet beam in this experiment is generated by free-jet expansion or free supersonic beam expansion, which is a form of gas dynamic beam. That means the gas does not flow freely from a cell into a vacuum, but is pressed through a nozzle at high pressure. Please note that the theory of this method is a little lengthy and only a qualitative explanation will be given here. More information can be found in Refs [43, 44, 52, 53]. In order to simplify the explanation and also because it is the case with our experiment, we assume a short converging nozzle. Hence the friction and heat conductivity can be neglected. Figure 2.3 shows a sketch of a free-jet expansion.

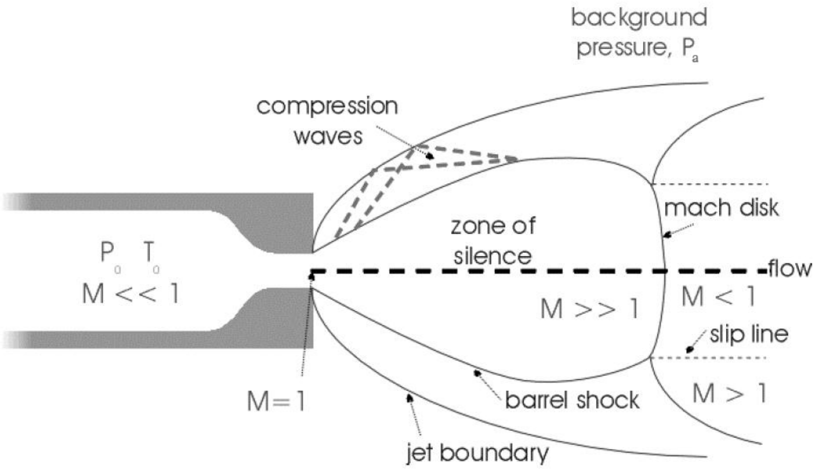

Figure 2.3.: Sketch of the principle of free-jet expansion. The gas is expanded into a vacuum through a nozzle under high pressure. The single variables are explained in the text below (from [42]).

The following abbreviations have been used in Figure 2.3:

T_0, P_0 ... Temperature and pressure of the gas within the cell which is at rest.
P_a ... Ambient (outside) pressure ($P_a < P_0$).
M ... Mach number, ratio of speed of the gas relative to the sonic speed in the medium.

The gas is accelerated towards the nozzle by the pressure difference $P_a - P_0$. If the pressure ratio fulfils the condition

$$\frac{P_0}{P_a} \geq \left(\frac{\kappa + 1}{2} \right)^{\frac{\kappa}{\kappa - 1}}, \tag{2.2}$$

where κ denotes the adiabatic exponent, the gas streaming through the nozzle reaches sonic speed at the nozzle exit ($M = 1$). If this is the case, the pressure at the nozzle becomes $P_0\left(\frac{\kappa+1}{2}\right)^{\frac{\kappa}{\kappa-1}}$, independent of P_a. The flow is then called 'underexpanded' (it is higher than P_a because of condition 2.2). Thus, the beam expands along the dashed lines in Figure 2.3. The velocity of propagation of the expanding beam increases with the width of the beam, finally exceeding sonic speed ($M > 1$). Due to this speed, the beam reaches pressures lower than P_a, which in turn causes shock waves (barrel shock) which change the direction of the supersonic beam and may reduce its velocity to subsonic speed ($M < 1$). This process causes the beam to decrease in diameter but increase in pressure. The shock wave travelling in the propagation direction of the beam with sonic speed ($M = 1$) is called mach disc and it is located at the position z_M:

$$\frac{z_M}{d} = 0.67\sqrt{\frac{P_0}{P_a}}, \tag{2.3}$$

where d is the diameter of the nozzle. The distance of the mach disc is at: z_M =3.7 cm, if values typical for the experimental setup of this work are used (P_0 =60 bar, P_a =$6 \cdot 10^{-4}$ mbar and d =5 μm). In order to extract the directed cluster beam and cut off the shock waves, a skimmer is installed in the experimental setup. The ideal position of the skimmer can be calculated by [4]:

$$\frac{z_S^{mm}}{d} = 0.125d\left[\frac{d}{\lambda_0}\frac{P_0}{P_a}\right]^{\frac{1}{3}} \tag{2.4}$$

with the average mean free path λ_0.

Two useful equations, for the final velocity (v_∞) and the mass flow rate $\dot{m}$ from the nozzle source shall be given here without further reference (for closer information see [52]):

$$v_\infty = \sqrt{\frac{k_B T_0}{m}\frac{\kappa}{\kappa-1}} \tag{2.5}$$

For our experiment (T_0 =15 K, $\gamma = 5/3$ and m =4 u), a value of v_∞ =400 ms is obtained for the final velocity.

$$\dot{m} = P_0 A\left[\frac{\kappa M}{R T_0}\left(\frac{2}{\kappa+1}\right)^{\frac{\kappa+1}{\kappa-1}}\right]^{1/2}, \tag{2.6}$$

where $\dot{m}$ is the mass flow rate, A denotes the minimum (throat) area of the nozzle, R the gas constant and M the molar mass.

2.3.2. Adiabatic Expansion

The expansion of the gas in the free-jet expansion can be assumed to be ideal [43, 52]. Let us first use an explanation based on kinetic gas theory and only then one based on thermodynamics.

In an adiabatic expansion, gas, per definition, expands into space (e.g., a vacuum chamber) without exchanging heat with its surroundings. This is approximately true if the expansion happens fast. So let us assume gas expands under pressure from a cell through a nozzle into a vacuum chamber, as it is the case with free-jet expansion, which is approximately adiabatic. The gas molecules exiting the nozzle, suddenly reach a space with a much smaller pressure. This causes the gas molecules to drift apart (i.e., expand). However, the expansion happens against the van-der-Waals forces, holding the gas molecules together. This means that the expansion needs energy, which the single molecules take from their kinetic energy, reducing the latter in the process. Since the kinetic energy of the particles is proportional to their temperature the process cools the gas.

Now for the mathematical part: As mentioned above, adiabatic means that the system does not exchange heat with the environment ($dQ = 0$), so the basic formula of thermodynamics connecting the inner energy (U), the heat (Q) and work (W) is

$$dU = \delta Q + dW \overset{\delta Q=0}{\rightarrow} dU = dW = -P_a dV = c_V dT. \tag{2.7}$$

The last relation is valid since $dU = c_V dT$, c_V is the specific heat for constant volume and the T Temperature. Thus we get:

$$dT = -\frac{P_a dV}{c_V} \tag{2.8}$$

When the gas is expanding, the change of volume is positive which makes the change of temperature negative according to equation 2.8 ($dV > 0 \rightarrow dT < 0$).

2.3.3. Formation of He Clusters

Now that we know how the expansion works, how do the He clusters form? The helium expanding out of the nozzle is still purely gaseous. In more technical terms, the start point of the adiabatic expansion is well within the gaseous region of the phase diagram. The cooling process proceeds along isentropes (isentrop - no change of entropy, e.g., an adiabatic reversible process). The temperature and pressure of the gas finally reach regions well within in the liquid phase of the phase diagram. As in macroscopic regions, this means that the helium condensates to droplets. The helium atoms still have a rather high kinetic energy, it takes about 1000 nozzle diameters [66] until the collisions cease. At this point the beam consists of single atoms and clusters (cf. Figure 2.4). The droplets continue to cool down along their path through the setup due to evaporative cooling (evaporating helium atoms take away the excessive energy), until they reach the final temperature of 0.375 K. The initial cooling rate of the droplets (during the adiabatic expansion) is very high (10^{11} K/s [67]) and decays exponentially. In order for the droplet generation to work properly, the nozzle has to be cooled, since the isentrope has to start at a rather low temperature to be able to cross the gas-liquid phase transition. The cooling rate is lower in this case[5].

---

[5] In the experimental setup used in this work, the nozzle was cooled with liquid helium to temperatures between 12-20 K depending on the desired cluster size.

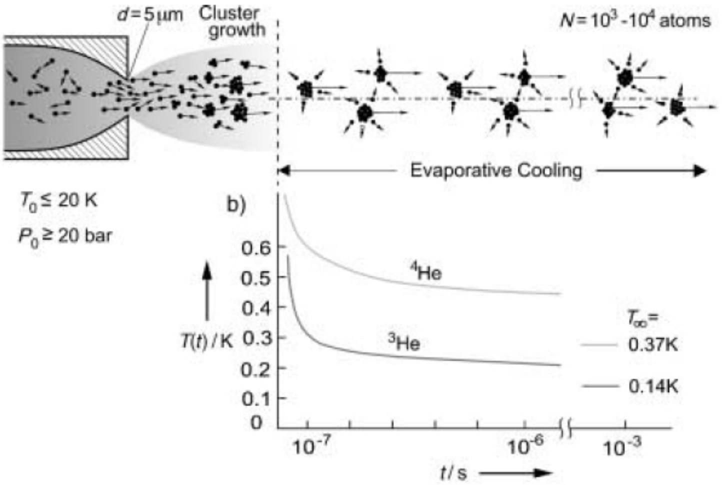

Figure 2.4.: Sections of the beam generation: The condensation starts shortly after the nozzle, after about 1000 nozzle diameters the collisions between the atoms cease (left part of the Figure); the droplets are then cooled down to their final temperature of 0.375 K by evaporative cooling -right part of the Figure (from [66]).

2.3.4. Size Distribution of He Clusters

The average size of the helium nanodroplets generated in this work is approx. 10^4 atoms. The size distribution is a log-normal distribution, the average droplet size corresponds approximately to the FWHM of the distribution. The probability density of the distribution is given by the following equation:

$$p_N(N) = \frac{1}{N\sigma\sqrt{2\pi}} \exp\left(-\frac{(\ln N - \mu)^2}{2\sigma^2}\right). \tag{2.9}$$

The average cluster size $\bar{N}$ is used for the average μ. The standard deviation σ can be obtained from the FWHM. Table 2.1 gives the cluster size for different temperatures [36].

Table 2.1.: Average cluster size ($\bar{N}$) in dependence of temperature (T). FWHM denotes the full width at half maximum (Data from [36]).

T / K	$\bar{N}$	FWHM
24	3170	2670
16	7220	7870
14	14400	15700

Table 2.1 shows that the size distribution broadens with increasing cluster size. Further, the cluster size increases with decreasing temperature. The velocity distribution is very small, according to [66] the ratio between FWHM (Δv) and velocity v is only $\Delta v/v \approx$0.01-0.03.

2.3.5. Doping He Clusters

The doping process developed by Scoles et al. [18] is easy to implement experimentally. The droplets fly through a cell containing a gas of the desired dopant. The pressure of the gas controls the number of guests picked up by the droplets. Species with a low vapour pressure, such as metals have to be heated (cf. Chapters below).

The probability to pick up n atoms satisfies a Poisson distribution:

$$P_k = \frac{\bar{k}^n}{n!} \exp^{-\bar{k}} . \tag{2.10}$$

The pickup is characterized by the average number of collisions $\bar{k}$. More information about pickup statistics can be found in Ref [42]. It is easy to imagine that the pickup process adds (kinetic) energy to the droplet, which is consequently set free again by evaporating helium atoms. According to [66], about 1600 helium atoms evaporate for every 1 eV of energy added to the droplet.

2.4. Spectroscopy

This Section gives a review of the most important facts of spectroscopy for this thesis, especially spectroscopic denotation. The first part shortly reviews spectroscopic denotation in simple atoms, because it is needed to understand the following Chapters. Since some helium droplet-dopant compounds can be seen as a diatomic molecule in the ‘pseudo-diatomic model’, the second part of this Section gives a short introduction to diatomic molecules and their spectroscopy. The last parts will then elaborate spectroscopy of doped helium droplets, including a more detailed view of alkaline earth metal doped helium droplets.

2.4.1. Atoms

Quantum Numbers

This paragraph provides a short re- and overview of the quantum numbers. Note: In this paragraph, we are only treating bare single atoms with no external field applied. The following quantum numbers define an electronic state (or its energy):

The principal quantum number $n = 1, 2, 3, ...$:
Classical: denotes the number of electron shell (the higher the number the larger the radius of the ‘shell’).
Quantum Mechanically: eigenvalue of $\hat{H}$, depends only on the radial coordinate, that means the distance between electron an nucleus. n mainly defines the energy of a level, since the energy is proportional to $1/n^2$.

The azimuthal quantum number $\ell = 0, 1, 2, ..., n-1$:
Commonly denoted with letters: $0 = S$, $1 = P$, $2 = D$, $3 = F$, which origin from spectroscopic characteristics of the lines: sharp, principal, diffuse and fundamental.
The azimuthal quantum number is derived from the Schroedinger equation and denotes the size of the orbital angular momentum of the electron: $|\vec{L_\ell}| = \sqrt{\ell(\ell+1)}\hbar$.

The spin quantum number $s = \pm 1/2$:
It can be seen as an angular momentum of the electron, however this is just a model view of an intrinsic characteristic of the electron.

Total angular momentum quantum number $j = l - s, l - s + 1, l - s + 2, ..., l + s$
Sum of the orbital $\vec{L_\ell}$ and spin angular momentum $\vec{L_s}$. As its name implies it denotes the size of the total electron angular momentum: $|\vec{L_j}| = \sqrt{j(j+1)}\hbar$.

If a system with more than one electron is considered the single momenta couple. Basically there are two ways, indicated in Figure 2.5. If the spin orbit interaction - so the interaction between the orbital and spin angular momentum - is weaker than the interaction between the electrons, the single orbital momenta will combine to a total orbital momentum $L = \sum_i \ell_i$ and the single spin momenta likewise to a total spin momentum $S = \sum_i s_i$ (LS-coupling). The total orbital and the total spin angular momentum will then add to a total electron angular momentum $J = |L \pm S|$, as shown in Figure 2.5 a).
If the spin-orbit interaction is strong the orbital momentum of each electron will couple with its spin momentum first, as indicated in Figure 2.5 b) (jj - coupling).

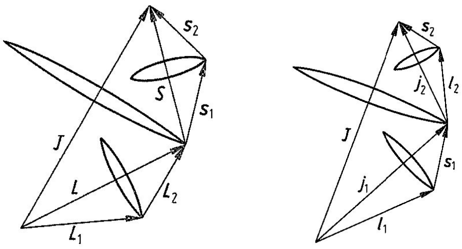

(a) (b)

Figure 2.5.: a) LS-couping in an atom - the spin orbit coupling is strong. b) jj-coupling in an atom - the spin-orbit coupling is weak (from [5]).

These coupling processes result in a splitting of the energy levels called ‘fine structure’. Note: for $\ell = 0$ (i.e., for S-states) no splitting will occur.

Spectroscopic Denotation

In order to label an energy level of an electron unambiguously, it is sufficient to give the quantum numbers n, ℓ and j. However, spectroscopists additionally give a parameter called multiplicity r:

$$r = 2S + 1,$$

which gives the number of states in the fine structure, i.e. the number of states an electronic state is split into by the spin-orbit coupling. An example for a definite label for a certain energy state of a bare atom without external electric or magnetic fields applied would be

$$3^2\mathrm{P}_{3/2},$$

where:

3 ... Value of the principal quantum number. n
2 ... Value of the multiplicity r.
P ... Value of the azimuthal quantum number $\ell = 1$.
3/2.. Value of total electron angular momentum quantum number j.

Selection Rules

Not all transitions are allowed, the following selection rules apply for optical transitions in a bare atom:

- $\Delta L = 0, \pm 1$ (single electrons: $\Delta \ell = \pm 1$)
- $\Delta J = 0, \pm 1$
- $\Delta S = 0$

The first two rules are due to the conservation of angular momentum. $\Delta \ell = \pm 1$ is due to the spin or momentum of photons. They belong to the group of bosons and have a spin of $s = 1$. When a photon excites an electron to a higher state it transfers its energy as well as its momentum to the electron, thus the momentum of the electron ℓ has to change by 1, hence $\Delta l = \pm 1$.
The rule for the spin $\Delta S = 0$ origins from the fact that the spin is not affected by the electric component of the electromagnetic field. For closer and mathematical descriptions see Ref [2].

Note: For molecules, matrices and doped helium droplets different selection rules might apply since the interaction between the single atoms relaxes the rules (cf. next Section).

2.4.2. A Short Introduction to the Basics of Diatomic Molecules

A monomer doped helium nanodroplet (i.e., a droplet with one guest atom) can be described by the so called 'pseudo diatomic model' if the atom is located on the surface of the droplet [56]. This model bases on the theory of diatomic molecules and sees the helium cluster as one atom of the molecule. It would go beyond the scope of this work to give a thorough description of the theory of diatomic molecules, the interested reader may refer to literature such as [10]. However, since the pseudo diatomic model is used to explain some results presented in this work, basic knowledge of diatomic molecules, especially their spectroscopic notation, is required. Hence a short introduction, mostly based on [10], is given here.

Diatomic Molecules in General:
The energy levels and transitions of molecules are much more complex than those of a bare atom, whose energy levels (and optical transitions) are mostly defined by electronic states. The energy states of molecules also depend on the geometry of the molecule and of the motions of its single atoms. Firstly the number of electronic states of molecules is much larger than for bare atoms. Secondly, as indicated in Figure 2.6, besides electronic transitions, vibrational and rotational transitions exist in a molecule. They origin from the oscillations of the atoms and rotations around its center of gravity. Vibrational and rotational lines, however, can not be resolved in our measurements, hence we will concentrate on the electronic states of diatomic molecules.

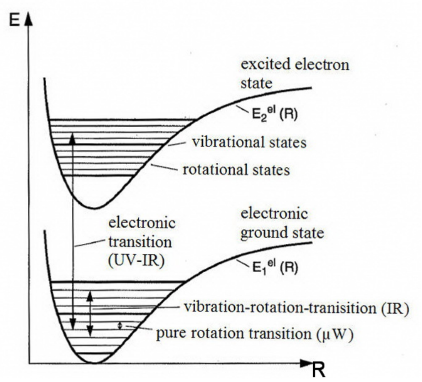

Figure 2.6.: Schematic of transitions in a molecule. Besides electronic transitions, vibrational and rotational transitions are possible (mod. from [10]).

The quantum numbers necessary to describe an electronic state in a molecule are very similar to those of a bare atom. As indicated in Figure 2.7 a) fine structure occurs in a molecule as in a bare atom due to the coupling of spin and orbital momenta. Figure 2.7 a) shows a simple example of a molecule with one electron and a low atomic number. The orbital angular momentum $\vec{\ell}$ and the spin momentum $\vec{s}$ couple with the molecular axis[6]. The projection of the spin momentum onto the z-axis is quantized as well, with the quantum number σ, which is $\sigma = \pm 1/2$ for molecules with one electron.

Figure 2.7 b) shows one possibility of the coupling of momenta in molecules with more than one electron, analogue to the coupling of momenta in a bare atom. Other ways of coupling are possible, however this is the only method used in this work.

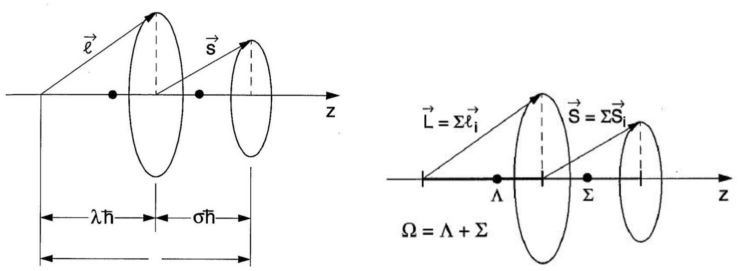

(a) (b)

Figure 2.7.: Projection of the orbital and spin angular momentum onto the molecular axis for a molecule with only a) one atom b) several electrons -Hund's *case (a)* notation (from [10]).

In case of Figure 2.7 b), the coupling of the total orbital momentum L to the molecular axis is stronger than to the total spin momentum S (i.e., low spin-orbit interaction), which results in a separation of L and S. Both precess independently around the molecular axis due to the momentum caused by the electric field of the nuclei. This means that L and S are not constant in time, which means that they are not 'good' quantum numbers anymore (they can't be used to define an electronic state). However the projection of L and S on the molecular axis - which is the temporal average of L and S - are constant. The quantum numbers of this projections are denoted as:

$$\Lambda = 0(\Sigma), 1(\Pi), 2(\Delta), ..., L$$

$$\Sigma = S, S-2, ..., -S$$

---

[6] In atoms with a high atomic number $\vec{\ell}$ and $\vec{s}$ would couple with each other first.

the quantum number of projection of the total electron orbital momentum then is:

$$\Omega = |\Lambda + \Sigma|$$

The values for Λ are denoted with capital Greek letters: $0 = \Sigma, 1 = \Pi, 2 = \Delta, 3 = \Phi$.
Note: Σ denotes $\Lambda = 0$ as well as the quantum number of the projection of the total spin momentum onto the molecular axis.

Spectroscopic Denotation

An electronic state in a diatomic molecule is defined by the notation:

$$X^{2S+1}\Lambda_{\Omega}.$$

where:

X ... corresponds the principal quantum number n, however since in molecules a higher n does not automatically mean higher a energy, a terminology has been introduced for the energetic sequence of electronic states $X, A, B, C, ...$, or $x, a, b, c, ...$ for states forbidden to excite from the ground state. However, in many cases X is not given at all.
$2S + 1$ ... Corresponds to the multiplicity r in a bare atom.
Λ ... Value of the quantum number of the projection of the total orbital momentum L onto the molecular axis.
Ω ... Value of the quantum number $\Omega = |\Lambda + \Sigma|$.

As an example Table 2.2 shows which molecular states are to be expected for each atomic state of a Cs doped helium droplet. Please note that only the state of the Cs atom is important here as opposed to common diatomic molecules where the states of both atoms are important.

Table 2.2.: Possible molecular states for combinations of one atomic state and a helium droplet.

Atomic state	Molecular state
S	$^2\Sigma_{1/2}$
P	$^2\Sigma_{1/2}$, $^2\Pi_{1/2}$, $^2\Pi_{3/2}$
D	$^2\Sigma_{1/2}$, $^2\Pi_{1/2}$, $^2\Pi_{3/2}$, $^2\Delta_{3/2}$, $^2\Delta_{5/2}$

Selection Rules

Due to the interactions between the atoms of a molecule, the selection rules for bare atoms (cf.Section 2.4.1) change. For closer and mathematical descriptions see [2]. For diatomic molecules the following rules apply:

- $\Delta\Lambda = 0, \pm 1$
- $\Delta\Omega = 0, \pm 1$
- $\Delta S = 0$

2.4.3. Alkali Metals on Helium Nanodroplets

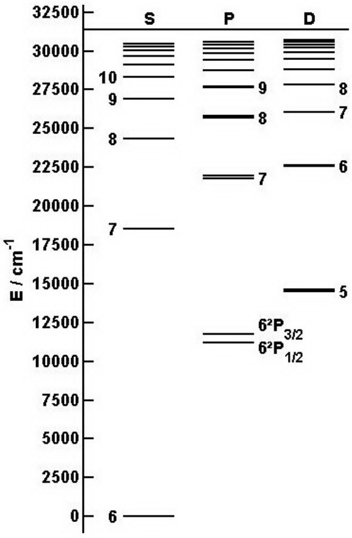

Figure 2.8.: Grotrian diagram for Cs.

Since this topic has been extensively covered in recent works of our group (e.g., [30, 45]), only the most important characteristics of alkali metals and alkali metal doped helium clusters are mentioned here.

Special care has to be taken when handling alkali metals, because they are very reactive, because they only have one valence electron. This fact simplifies their spectra, on the other hand. Figure 2.8 shows the sample of a Cs level diagram. Since alkali metals have only one valence electron, the spectroscopic denotation as explained in Section 2.4 applies to the bare atom (e.g., $6^2\mathrm{P}_{1/2}$ for the first excited state of caesium). A special characteristic of alkali metals is that they do not immerse into the droplet, but they stay on the droplet, forming a depression on its surface, called 'dimple'. This is due to the very low interaction potential of alkali metals with helium droplets. According to [27], it is only equal to 0.5-1.5 cm^{-1} per helium atom. Since alkali metals reside on the surface of the helium droplets the droplet-alkali metal compound can be described by the 'pseudo-diatomic model'. This changes the denotation and also the number of levels to expect. Note: Hund's *case (a)* notation is used if the droplet induced broadening is not larger than the spin-orbit coupling: This results in the variety of states given in Table 2.2. In higher states, the droplet induced broadening is larger than the spin-orbit coupling, hence the latter can be neglected, that means only Λ is given to denote a state (e.g., Σ, Π, Δ). Because the molecular notation is ambiguous, the states are denoted as in a bare atom with the molecular notation in brackets (e.g., $6^2S_{1/2}$ $(^2\Sigma_{1/2})$).

2.4.4. Alkaline Earth Metals

Since doping helium droplets with alkaline earth metals is the main objective of this thesis and is done for the first time in our group, this topic will be treated more extensively.

Alkaline earth (Ake) metals are all atoms in the second column of the periodic table. However, since beryllium (Be) is highly toxic and radium (Ra) is radioactive, they are not taken into account here, alkaline earth metals refer in the context of this work to magnesium (Mg), calcium (Ca), strontium (Sr) and barium (Ba).

General

The term ‘alkaline earth metals’ origins on the one hand from their high resources in the earth crust and on the other hand from their similar behaviour to alkali metals. However, Ake metals have a completed s-shell so they are less reactive than alkali metals.
All Ake metals build a thick oxide layer at atmosphere. The heavier elements are more reactive, Ca, Sr and Ba strongly react with water, creating inflammable gases. Hence, all those elements have to be treated with care and under an inert gas atmosphere (e.g., argon). For more information refer to the corresponding safety instructions of each element [54]. Table 2.3 summarizes the most important characteristics of alkaline earth metals [41].

Table 2.3.: Important characteristics of alkaline earth metals (from [41]).

Characteristic	Mg	Ca	Sr	Ba
atomic number	12	20	38	56
atomic mass (u)	24.3	40.08	87.62	137.33
density (g/cm^3)	1.74	1.54	2.63	3.62
melting point (°C)	650	838	771	726
boiling point (°C)	1107	1487	1384	1640

Spectroscopy

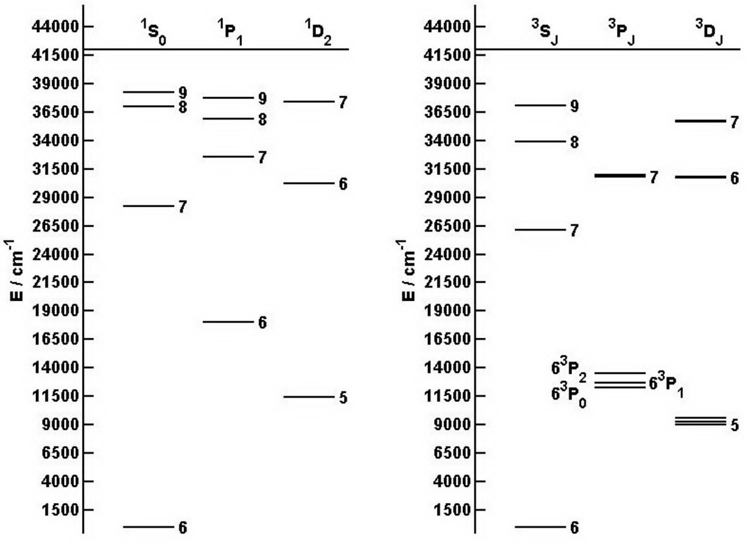

(a) (b)

Figure 2.9.: a) Ba singlet term level diagram b) Ba triplet term level diagram.

The fact that alkaline earth metals have two valence electrons makes their spectra more complex. While the multiplicity is always equal to $r = 2$ for alkali metals, it can be $r = 2S + 1 = 1, 3$ for alkaline earth metals since the spin quantum numbers of the two electrons can add to $S = 1$ (parallel) or subtract to $S = 0$ (anti-parallel). In the first case ($r = 1$ - singlet), only one energy state occurs for every L, hence the name singlet. This means that the anti-parallel spins cancel out and no spin-orbit coupling occurs (e.g., barium Figure 2.9 a).

The other possibility is that the spins are parallel and the total spin quantum number is $S = 1$. For S-states, still no spin-orbit splitting occurs, due to the radial symmetry of the S-state. However, for higher L, for instance P-states, every state is split into three levels (triplet), since the total angular momentum is $|L - S| \leq J \leq L + S$, which is in this example: $J = 0, 1, 2$ (e.g. barium Figure 2.9 b). However, the transition rule $\Delta S = 0$ forbids a transition from a singlet state to a triplet state.

Spectroscopy of Alkaline Earth Metal Doped Helium Droplets

As stated in the earlier presented historical perspective, not a lot of work has been done with alkaline earth metal doped helium clusters. This Section will give an overview of the work done up to now:

- Stienkemeier et al. [59] were the first to investigate Ca and Sr on helium droplets. They excited the lowest singlet transition and found that the spectra are broadened and blue-shifted. The broadening increases with the droplet size, but converges to a third of the broadening in bulk helium. Compared to alkali metals, the shift as well as the broadening are much larger, but smaller than compared with bulk helium experiments. The location of Ca and Sr on the droplet was not clear at that point.
- Shortly after the first work on Ake metals doped helium clusters, Stienkemeier et al. [60] investigated barium on helium droplets. They found the same behaviour as for Ca and Sr.
- The first investigation of Mg doped He droplets was published by Reho et al. [50]. They found the shifts and broadening of the Mg spectra to be close to those measured in bulk liquid helium. Hence they concluded that Mg is solvated into the droplet. Some theoretical calculations were also performed in this paper in order to determine the location of Mg atoms on He droplets, however no definite answer was found.
- Ren et al. [51] used another theoretical method to clarify the location of Mg on He droplets. Their work give a good overview of the work done on Mg doped He droplets. According to their calculations Mg resides on the surface of the droplet as Ca, Sr and Ba, however embedded in a deeper dimple.
- Overviews and summaries about work on (Ake metal doped) He droplets can be found in References [8, 58, 64, 66].

In sum this means that Ca, Sr and Ba reside in a dimple on the surface of the He droplet, however it is deeper than with alkali metals. No higher excitations than the lowest singlet transition have been investigated by now, so the spectra of Ake metals on He droplets are still unknown. Excitation of a triplet state from the ground or other singlet states are forbidden due to the selection rule $\Delta S = 0$. The interaction of the Ake metals with the droplet might allow such transitions, but we expect this probability to be so small that it can be neglected. So we do not take triplet states into account, which means that the molecular denotation is sufficient (only the Λ values are given).

2.5. A Short Introduction to Pulsed Lasers

There are two main forms of generating pulsed laser light: mode-locking and Q-switching. The latter technique is used in the *Coherent Indigo S* lasers system, hence this Section gives a qualitative description of this technique. Most of the information given here has been taken from [29], where more details as well as quantitative descriptions can be found.

2.5.1. Q-Switching

The term 'Q-switching' origins from 'switching' the quality factor of the cavity (Q). In other words, the cavity is made opaque and transmissive in turns - which basically means that the resonator is turned off and on. If it is off no lasing happens, hence the upper laser level is not depleted and a higher population inversion can build in the lasing medium. If the cavity is made transmissive again, the higher population of the upper laser state results in a considerably higher photon density.

Design of Q-Switches

Q-switches have to make the cavity opaque and transmissive. So the switching process has to be fast and exact, the opacity has to be maximized to prevent photon leakage. There are four construction methods :

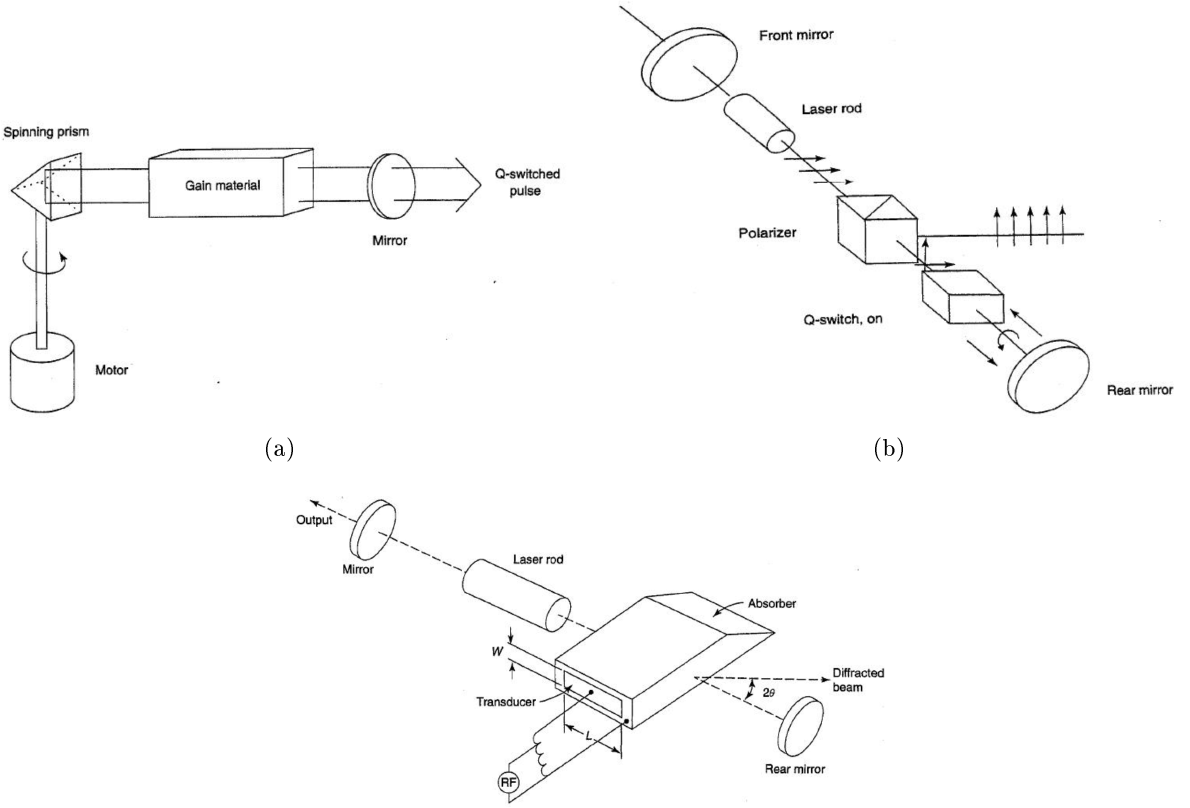

(a) (b) (c)

Figure 2.10.: Different designs for Q-switches a) mechanical b) electroopitc c) acousto-optic (from [29]).

Mechanical Q-Switch

Figure 2.10 a) shows the concept of a mechanical Q-switch. The rear mirror of the cavity is exchanged with a roof prism mounted on a motor. The motor rotates at a very high speed (up to 50000 rpm). A reflection back into the cavity, and hence laser pulse generation, only occurs for certain angles of the prism.

Electrooptic Q-Switch

Figure 2.10 b) shows the concept of an electrooptic Q-switch. In this method, an electrooptic crystal and a polarizing beam splitting cube are inserted into the cavity, commonly between a linear polarizer and the rear mirror. The birefringence of these crystals change with an applied electric field.

At first the laser beam passes through the beam splitting cube (cf. description of the Glan-Taylor prim in Section 4.3) and the electrooptic crystal which changes the polarization of the beam from linear to right circular. The beam is then reflected from the rear mirror, which changes its polarizations to left circular. When it passes again through the electrooptic crystal, its polarization is changed back to linear but perpendicular to its initial polarization. At this polarization, the laser beam is reflected out of the cavity by the beam splitting cube. When no voltage is applied to the electrooptic crystal it is not birefringent and hence does not change the polarization of the beam. In this case, the beam travels along the cavity unchanged.

Acousto-Optic Q-Switch

Figure 2.10 c) shows the concept of an acousto-optic Q-switch. This method uses an acousto-optic modulator (AOM) within the cavity of the laser. An AOM consists of a material whose index of refraction changes when it is excited by acoustic waves. As indicated in Figure 2.10 c), when the AOM is turned on, the laser beam is reflected out of the cavity, that means the resonator is turned off. This is the technique used in the *Coherent Indigo S* system (cf. [45]).

Dye Q-Switch

This method uses a dye cell commonly mounted on the rear mirror of the cavity. Certain dyes show nonlinear absorption characteristics, which means that they absorb a certain part of the laser light at low intensities, which reduces the cavity transmission. At a certain intensity, the absorption decreases, which increases the transparency of the cavity.

CHAPTER 3

Experimental Setup

In this Chapter, the apparatus including the laser setup will be explained. The interested reader might also refer to [42], where the whole setup is described in much more detail, although it is not completely up to date anymore. Figure 3.1 shows a photo of the apparatus. However, the CAD drawing in Figure 3.2 provides a clearer view of the laboratory and the experimental setup. The most important parts have been denoted and will be explained in the subsequent Sections:

- Source chamber.
- Pickup chamber.
- Detection chamber.
- Laser setup, including the Excimer pumped, pulsed dye laser (*Lambda Physik FL3002*) and the Nd:YVO3 pumped, pulsed Ti:Sa laser (*Coherent Indigo S*)

The CAD drawing in Figure 3.2 also provides a good opportunity to visualize the mode of operation of the He nanodroplet setup and the detection system: The He nanodroplet beam is produced in the source chamber. It is then guided through the pickup chamber (where the pickup processes happen) into the detection chamber where its path ends at the quadrupole mass spectrometer at the end of the chamber. The laser beams of the corresponding lasers, in this case the *Lambda Physik FL3002* pulsed dye laser and the *Coherent Indigo S* pulsed Ti:Sa laser are guided via mirrors into the chamber through one of the four windows on the side of detection chamber. To make sure that the laser beams cross the He nanodroplet beam, they are guided out of the detection chamber through four other windows. A laser table and an optical platform allow further implementation of beam manipulation devices, such as a Glan-Taylor prism to overlap the two laser beams (cf. Section 4.3).

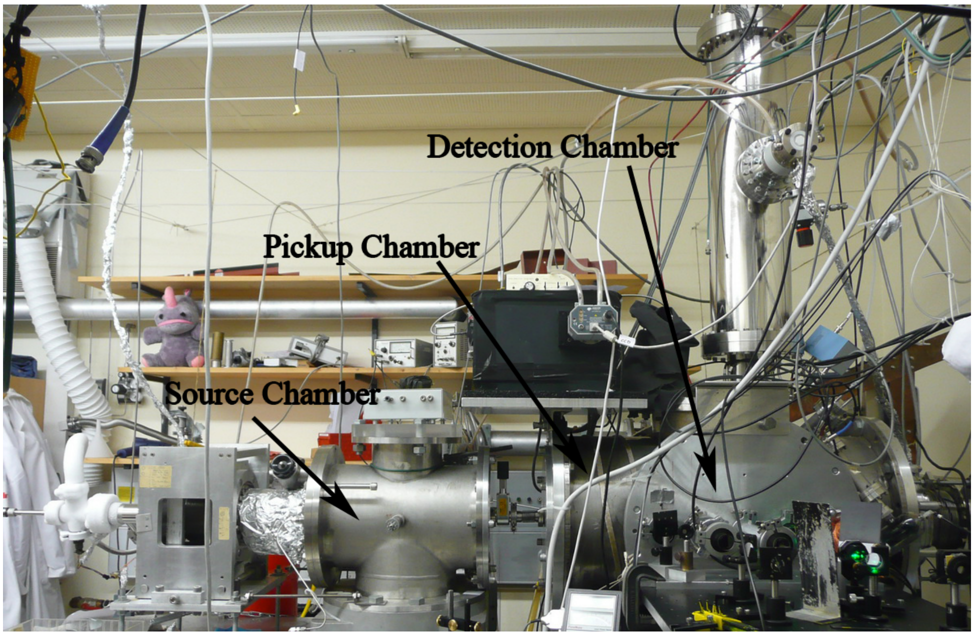

Figure 3.1.: Photo of the vacuum apparatus, consisting of the source chamber, the pickup chamber and the detection chamber.

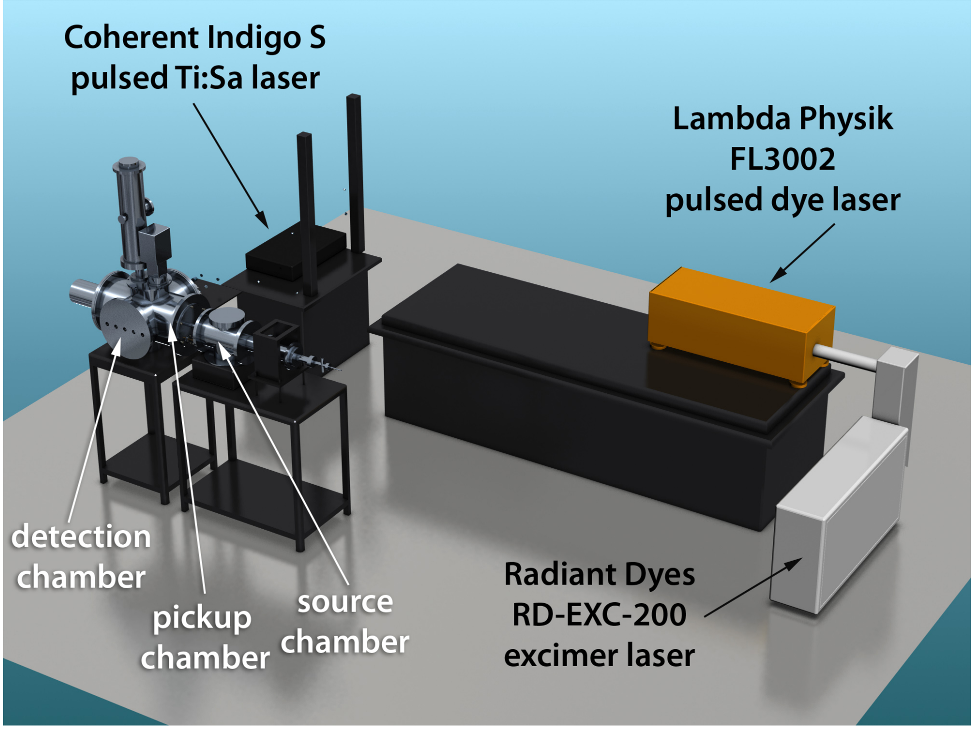

Figure 3.2.: CAD-drawing of the laboratory, showing the vacuum apparatus as in Figure 3.1 as well as the laser setup for the REMPI-TOF experiment.

3.1. Source Chamber

In the source chamber the helium nanodroplet beam is generated by cooling gaseous helium and expanding it through a nozzle into vacuum. The chamber is evacuated by a set of pumps (an *Edwards E2M 80* rotary vane, an *Edwards EH 1200* roots and a *Leybold D1 6000 10B; Kat.Nr. 22676* oil diffusion pump) and held at a pressures of about 10^{-6} mbar when there is no He cluster beam and at a pressure of about 10^{-3} mbar when the beam is established.

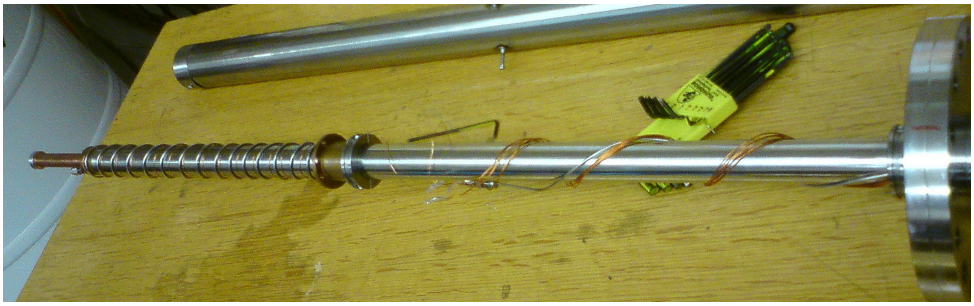

(a)

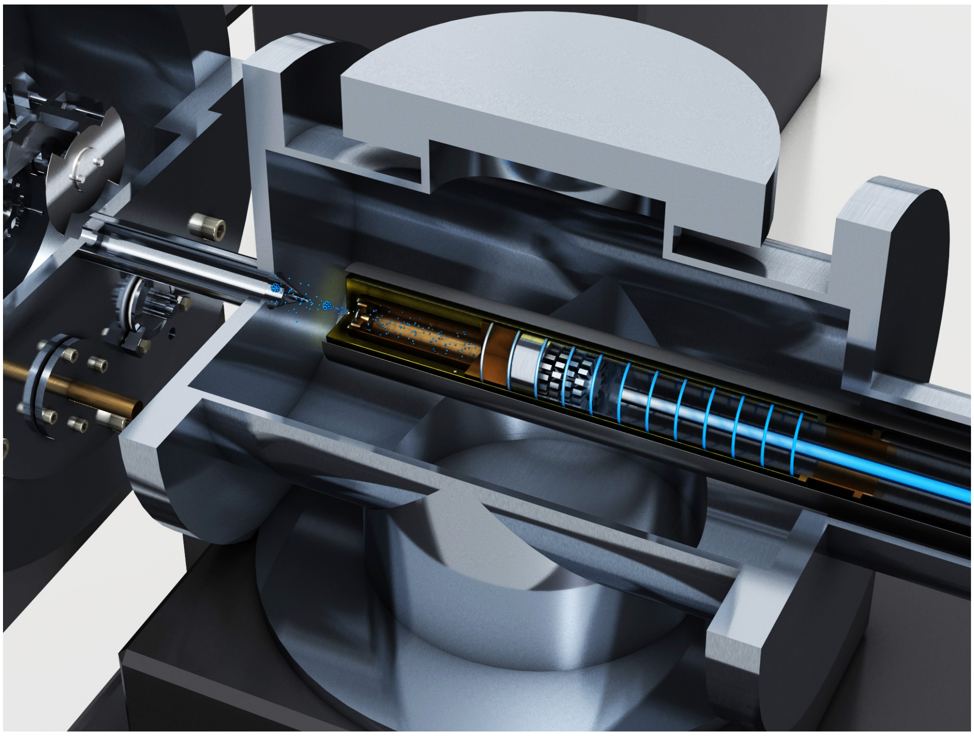

(b)

Figure 3.3.: a) Photo of the cooling rod and the nozzle at its end. b) CAD drawing of the source chamber: cooling rod, the heat exchanger and the nozzle are visible.

The gaseous high purity helium used to produce the beam is cooled by the right part of the rod shown in Figure 3.3 b). As indicated in the Figure, it consists of two high quality steel pipes fitted into each other and of a heat exchanger at its end. Liquid helium from a dewar flows through the inner pipe, cools down the heat exchanger and flows back through the outer pipe into the helium recovery system. The design of the heat exchanger increases its interaction time with the helium, hence making the cooling more efficient. A heater wire is wound around the heat exchanger, allowing to control the temperature of the nozzle exactly.

The high purity helium used to produce the droplet beam flows through the small tube wound around the cooling rod into the nozzle holder, mounted directly onto the heat exchanger. On its way through the tube and the nozzle holder, which serves as a gas reservoir, the helium cools down to a temperature of ≈14 K. A heater wire and a temperature sensor are connected to the heat exchanger, the temperature of the nozzle is controlled by a *Lakeshore 330 Autotuning* controller. The cooled high purity helium gas then expands through the 5 μm nozzle into the source chamber and cools down further. The pressure of the helium gas and the temperature of the nozzle determine the size of the droplets (e.g., a pressure of 60 bar and a nozzle temperature of 14 K leads to an average droplet size of 10^4 atoms). The helium droplet beam is guided from the source chamber into the pickup chamber through a 400 μm skimmer. The skimmer has two main tasks: Firstly, to separate the two chambers - the pressure in the source chamber is higher due to the helium background and contaminated by backstreaming diffusion pump oil - and secondly to cut off the helium background from the cluster beam.

3.2. Pickup Chamber

This chamber, depicted in Figure 3.4, contains the various pickup cells which hold the materials the droplets are doped with. The pickup is evacuated by a set of pumps (a *Leybold Trivac D10 BHV Kat.Nr. 11580* rotary vane pump and a *Leybold Kat.Nr. 85673* turbo molecular pump) and held at a pressure in the lower range of 10^{-7} mbar.

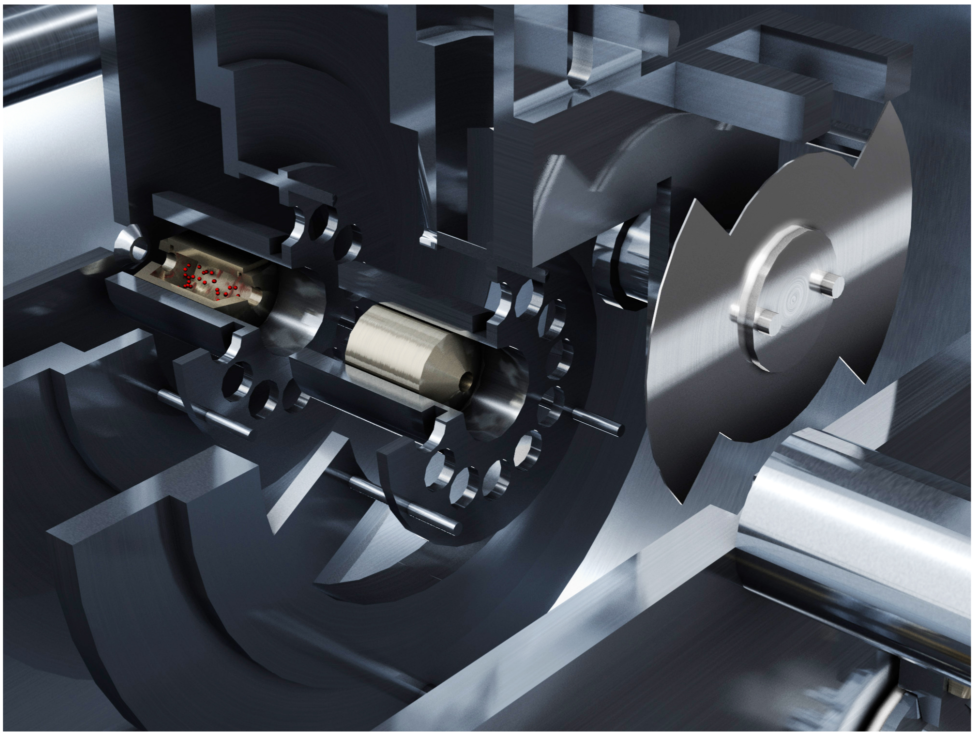

Figure 3.4.: CAD Drawing of the pickup chamber, showing the chopper and the two pickup devices for gases (right side of the picture) and alkali metals (left side of the picture).

Note: This Section only explains the old setup of the pickup chamber, that means without the alkaline earth metal pickup cell, which has been designed, constructed and installed in the course of this work (cf. Chapter 6 for a detailed description).
The setup of the pickup chamber is quite simple. The helium nanodroplet beam passes a cell containing the material which should be picked up. In the current setup, the cell is a cylindric high quality steel can. In order to make the pickup process work, a certain vapour pressure of the material within the pickup cell must be maintained. Ref [37] gives an equation and the respective constants for a list of 'metallic elements' to calculate the vapour pressure of these materials as a function of temperature. Figure 3.5 shows this function for the alkali metals caesium and rubidium. Previous experiments of our group have been performed with these two materials.

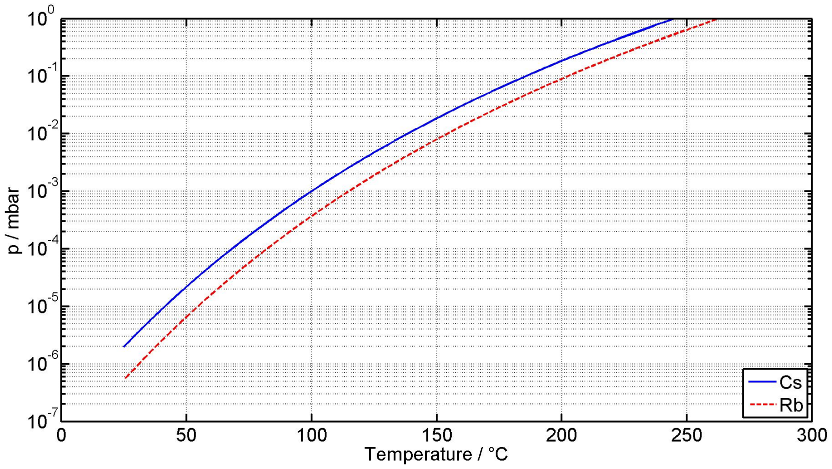

Figure 3.5.: Vapour pressure of the alkali metals caesium and rubidium as a function of temperature (data from Ref [37]).

To efficiently dope helium nanodroplets with alkali metals, a vapour pressure in the range of $10^{-3} - 10^{-4}$ mbar proved to be ideal, in the experience of our group. For caesium this pressure is reached at 90 °C and for rubidium at 120 °C, hence the pickup cells have to be heated. The cells shown in Figure 3.4 are heated by a thermocoax wound around the high quality steel cylinder holding the pickup cell. A thermocouple is attached to the cylinder so that the pickup temperature can be controlled by a *Micromega* controller. As indicated in Figure 3.4, the pickup chamber holds - from right to left: A chopper, a gas pickup cell and an alkali metal pickup cell. The chopper is used to chop the droplet beam so that a detector will detect the droplet beam and the background signal when the chopper is open and only the background signal (mainly due to the atomic beam out of the pickup cells) when the chopper is closed. This provides a simple possibility to extract the background from the actual measuring signal by building a difference signal. The gas pickup cell is a simple high quality steel can connected to a leak valve outside of the apparatus by a pipe. This provides an easy way to dope the helium droplets with different gases, such as hydrogen. Since the gas pressure can be controlled by the gas flow, this cell obviously needs no heating.

3.3. Detection Chamber

The detection chamber is only separated from the pickup chamber by a high quality steel sheet metal holding a 5 mm skimmer. Hence the vacuum conditions are similar in both chambers. The detection chamber is pumped by another set of pumps (a *Leybold Trivac D16B Kat.Nr. 91265-1* rotary vane pump, a *Leybold Turbovac TMP 600C*, a *Varian 949-9452* diaphragm pump and a *Pfeifer TMU-064 DN 63CF-F-1* turbomolecular pump) and held at a pressure in the upper range of 10^{-8} mbar. Figure 3.6 shows a CAD drawing of the pickup and detection chamber.

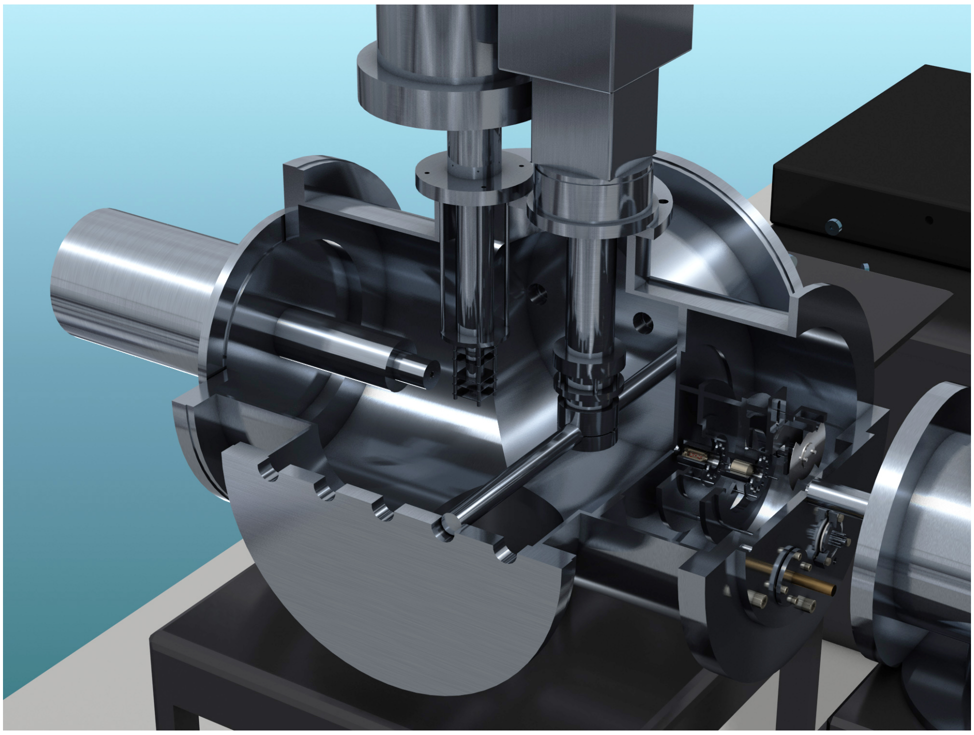

Figure 3.6.: CAD drawing of the detection chamber, showing the QMS (at the left end of the chamber), the TOF mass spectrometer (in middle of the chamber) and the photomultiplier for LIF measurements (at the right side of the TOF mass spectrometer), as well as the side windows for the laser beams.

As its name implies, all measurements take place in this chamber, hence it holds various measuring devices:

- A quadrupole mass spectrometer (QMS) of the type *Extrel C50-Q* is mounted at the back end of the chamber.
- A Time-of-flight mass spectrometer (TOF) of the type *Jordan D-850 AREF* is mounted on top of the chamber (see [30] and also further below).
- A photomultiplier (PMT) (cf. [42]) is mounted on top of the chamber for LIF measurements.
- The PMT can be exchanged by a spectrograph.
- The sides of the chamber hold four small windows each, through which laser light can interact with the droplet beam.
- An ionization manometer is mounted to monitor the pressure.

Details and closer explanations of the devices listed above can be found in the given references, in the following only the devices used for the experiments presented in this thesis are explained in detail.

3.3.1. Time-of-flight Mass Spectrometer

Figure 3.7 shows a CAD drawing of the Time-of-flight (TOF) mass spectrometer, type *Jordan D-850 AREF*, mounted on top of the apparatus. A detailed description of this device can be found in [30].

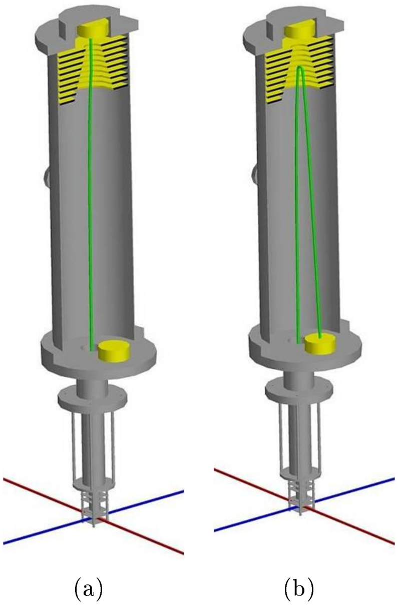
(a) (b)

Figure 3.7.: CAD drawing of the Time-of-flight mass spectrometer and its two different operation modes: a) linear mode and b) reflectron mode.

The principle of operation of a Time-of-flight mass spectrometer is rather easy to understand: The blue beam in Figure 3.7 resembles the droplet beam, the red one the laser beam. A high voltage is applied to the two field plates above and below the droplet beam. In the experiments below, mostly 1000 V for the lower and 700 V for the upper plate are used (for the reflectron mode, cf. Figure 3.7 b). Let us assume the laser beam ionizes the helium droplet. Due to the potential difference of the plates, the ions are accelerated upwards. Another plate, which is grounded, is mounted some way above the upper plate, thus the ions are further accelerated. If the TOF spectrometer is used in linear mode the ions hit a detector after flying some distance in a field-free zone. Since heavier ions are harder to accelerate, they are flying slower, hence have a different flight time. This relationship can be expressed in the following equation:

$$t = L\sqrt{\frac{m}{2eU_B}} \tag{3.1}$$

where:

t ... time of flight;
L ... flight distance;

m ... mass of the ion;
e ... electron charge;
U_B... Potential at the position of the ion.

The time of flight is measured by the device and all other variables are constant, hence the mass of the ions can be calculated.

If the TOF spectrometer is used in the ‘reflectron’ mode, additional plates at the top end of the spectrometer are supplied with high voltage in such way that the ions are repelled from the top and are reflected back downwards at a slight angle. At the base of the TOF spectrometer, they hit another detector. This mode elongates the flight time of the ions, thus improving the mass resolution. Note: This mode is not possible for very high masses.

In order to properly use the TOF mass spectrometer a pulsed laser has to be used to ionize the atoms since the time of flight measurements need a definite start point, which in this case is the start time of each laser pulse.

3.4. Laser Setup

Our laboratory is equipped with extensive laser systems. In Table 3.1 the different types of lasers available and their wavelength range are displayed.

Table 3.1.: Specification of the available laser systems:
λ... Wavelength range of this type of laser in the corresponding mode or with the corresponding dye.
P_{max}... Maximum power of the corresponding laser system.
SHG... second harmonic generation;
THG... third harmonic generation;
pumped by... pumping laser;

Type	**Name**	**Mode**	**λ / nm**	P_{max}		**pumped by**
Excimer	Radiant Dyes RD-EXC-200	pulsed	308	240	mJ	
Nd:YAG	Coherent Verdi V10	cw; SHG	532	10	W	
Nd:YAG	Coherent Verdi V18	cw; SHG	532	18	W	
Nd:YVO4	Coherent Evolution 15	pulsed; SHG	532	3	mJ	
Ti:Sa	Coherent 899 Ring Laser	cw	740-920	5	W	Verdi V18
Dye	Coherent 699 Ring Dye Laser					
	DCM	cw	632-690	1.6	W	Verdi V10
	Rhodamin B / Kiton Red	cw	588-644	1.5	W	Verdi V10
	Rhodamin 6G	cw	569-608	2.2	W	Verdi V10
	Rhodamin 560 (110)	cw	543-560	1	W	Verdi V10
Ti:Sa	Coherent Indigo-S					
		pulsed	750-920	1.6	W	Evolution 15
		pulsed; SHG	375-460	0.5	W	Evolution 15
		pulsed; THG	250-307	0.05	W	Evolution 15
Dye	Lambda Physik FL3002					
	Coumarin 307	pulsed	480-525	8	mJ	Excimer
	Coumarin 153	pulsed	520-575	6	mJ	Excimer

In the measurements presented in Chapters 7 and 5, mostly the Indigo (Nd:YVO4 pumped, pulsed Ti:Sa laser) and the Lambda Physik laser systems (Excimer pumped, pulsed dye laser) have been used. The Indigo System has been explained thoroughly in [45], hence only the Lambda Physik system will described in detail in this work.

3.4.1. The *Radiant Dyes RD-EXC-200* Excimer Pump Laser

This Section offers a short description of the excimer pump laser. A manual for how to operate it and for how to perform the most important maintenance tasks can be found in Appendix A.2, since the manual of the laser [48] has been found to be written in a not very user-friendly way.

Working Principle of Excimer Lasers

An excimer laser in general uses a noble-gas halogen mixture like (in this case) XeCl as an active medium. The name derives from ‘excited-dimer’, referring to the active medium. A dimer usually denotes a molecule of two identical atoms - hence excimer is not the correct term for lasers using a noble-gas halogene mixture anymore, which is why they are also called exciplex lasers. The special characteristic of the molecules used in this lasers is that they are not stable in their ground state, but only in an excited state - this ensures a population inversion of high quality since there are no molecules in the ground state at all. The laser transition is activated by a high voltage discharge. Since this discharge cannot be maintained continuously this kind of laser can only be operated in pulsed mode.

The *Radiant Dyes RD-EXC-200* Excimer Laser

Most of the information given in this Section has been taken from [48]. The *Radiant Dyes RD-EXC-200* uses a XeCl gas mixture as an active medium. It consists of:

- HCL (4.5) 4 mbar, 0.125-0.13%
- XE (4.0) 60 mbar, 1.875-1.8%
- NE (4.5) 3136 mbar, 98.00%, rest
- Sum: 3200 mbar, 100%

Where the numbers in brackets give the quality of the corresponding gas.

The housing of the laser holds the high voltage equipment and the discharge chamber on the one hand as well as the power supply and the control electronics on the other hand. The first two parts are separated by a shielding wall and the control electronics is additionally shielded by a metal box.

ATTENTION: In the discharge electronics, high voltage of up to 30 kV is produced and stored in capacitors. As explained later, it might be necessary to open the laser housing. However never open the shielding wall and act with extreme care whenever opening the housing.

For further description of the laser operation, trigger manipulation and gas exchange see Chapter A.2, as well as the instruction manual [48].

Specifications:

Active Medium ... XeCl gas
Wavelength ... 308 nm
Max. pulse energy ... 240 mJ
Pulse duration ... 26 ns
Beam dimension ... 10x25 mm
Max. repetition rate ... 100 Hz

3.4.2. *Lambda Physik* Pulsed Dye Laser

In the course of this work, especially for the REMPI-TOF spectroscopy (cf. Section 4.2) a *Lambda Physik FL 3002* pulsed dye laser has been used. This Section will shortly describe the working principle and advantages of dye lasers in general and then go into detail about the *Lambda Physik FL 3002*.

Dye Laser - A General Description

A dye laser system uses an organic dye as a lasing medium. The dye is mostly a liquid solution which is either pumped through a nozzle, creating a dye jet which crosses the pump beam, or it is pumped through a cuvette inserted into the pump beam path. The laser transition in the dye can be excited or pumped by cw or pulsed lasers, as well as by incoherent light sources. No general information about the laser transition in dyes can be given, since a wide range of dyes, made of very different substances, exist, not all of them using the same transitions. However most of them use molecule transitions.

The big advantage of a dye laser system is that the lasing medium can be exchanged very easily by simply filling another dye solution into the dye-pump. Each dye can be tuned over a certain range of wavelength, which is usually in the order of several tens of nanometers. According to our experience, when pumped by the pulsed excimer laser *RD-EXC-200*, Coumarin 153 and Coumarin 307, which have been used in the experiments below, cover a wavelength range of 525-575 nm and 480-520 nm, respectively. The output wavelength and the range of wavelength for each dye also vary with the type of the pump laser. Different setups of dye lasers are available for cw as well as for pulsed mode. In sum, dye lasers are ideal in experiments where a wide range of wavelength is needed.

The *Lambda Physik FL 3002*

This laser has been built in 1988. Despite its age no problems at all occurred in the course of this work. It is easy to use and to maintain, and the manual [32] is, although a little lengthy, written in an understandable manner and contains all the information to set up, maintain and operate the laser. Hence, this Chapter will only go into detail about the special features and the working principles of this laser, rather than its operation. Some short notes about the most important operation modes can be found at the end of this Section. A routine for how to set up the laser and to optimize its power has been added in the Appendix A.3 - the appendix provides a shorter description than in the manual and is enriched with some personal experiences.

First, some important technical specifications are given:

- Oscillator Design: Littrow-type oscillator with 600 lines/mm - grating in 3rd-8th order.
- Bandwidth: $0.2\,\mathrm{cm}^{-1}$ or with build-in etalon $0.04\,\mathrm{cm}^{-1}$.
- Wavelength Range XeCl pumped: 332-860 nm.
- Peak power: up to 20 MW, depending on pump source and dye.
- Average power: up to 10 W, depending on pump source and dye.
- Frequency Stability: $<0.5\,\mathrm{cm}^{-1}/°\mathrm{C}$ without etalon and $<0.01\,\mathrm{cm}^{-1}/°\mathrm{C}$ with etalon.
- Pulse width and amplitude stability are similar to pump laser.

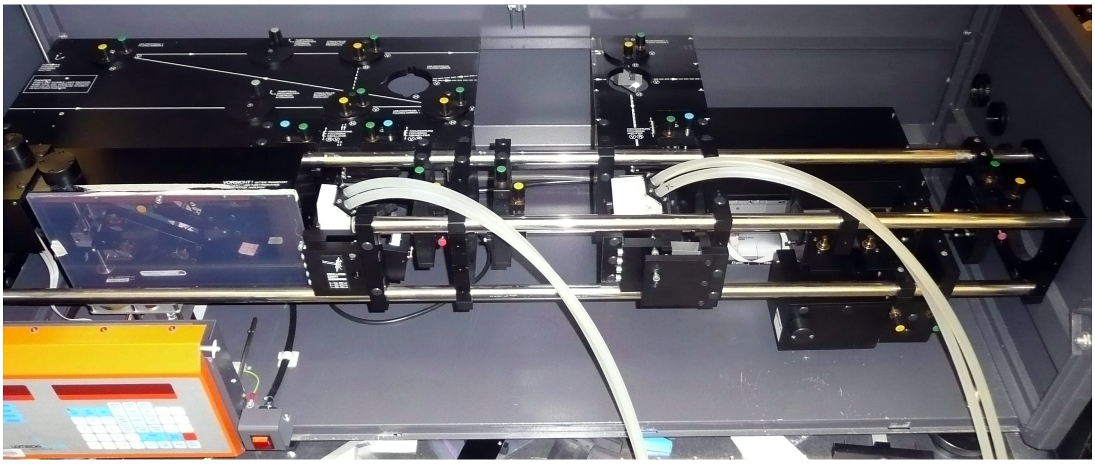

(a)

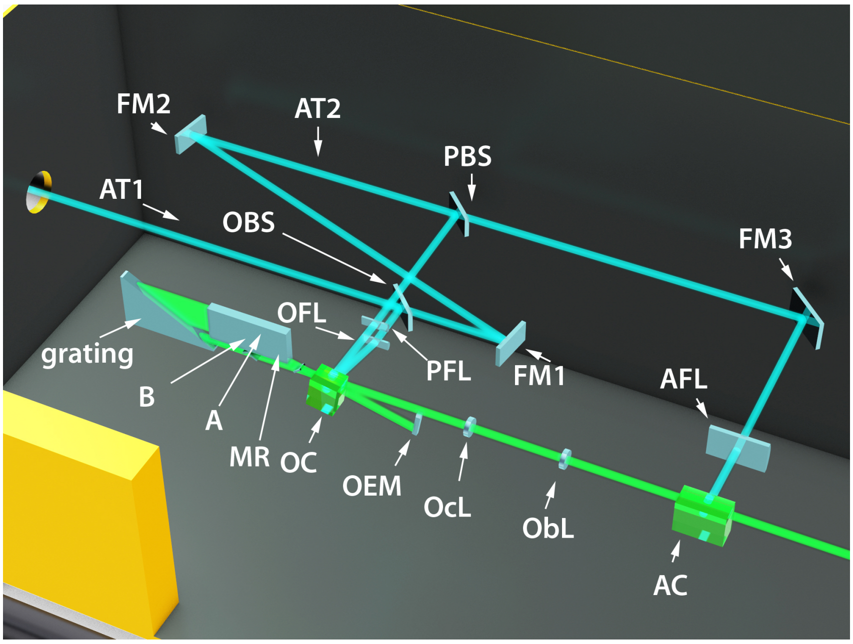

(b)

Figure 3.8.: Photo a) and CAD drawing b) of the *Lambda Physik FL 3002* pulsed dye laser system. This laser uses a two step amplification explained in the text above and a servo-motor driven Littrow-configuration grating to tune the wavelength.

For an easy explanation of the *Lambda Physik FL 3002* setup, let us follow the pump beam along its path through the laser, with the help of Figure 3.8 b):
The excimer laser pump beam enters on the left side of Figure 3.8. Firstly a small part (approx. 10 %) of it is split off by the oscillator beam splitter (*SPM1*) and guided through the oscillator focusing lens (*OFL*) into the oscillator/preamplifier dye cuvette (*CV1*). This part of the pump beam starts the lasing process in the dye. The resonator is, in this case, between the grating (*GRA*) on the left side and the oscillator cavity end-mirror (*OCEM*).

The Detail Box

The Resonator:

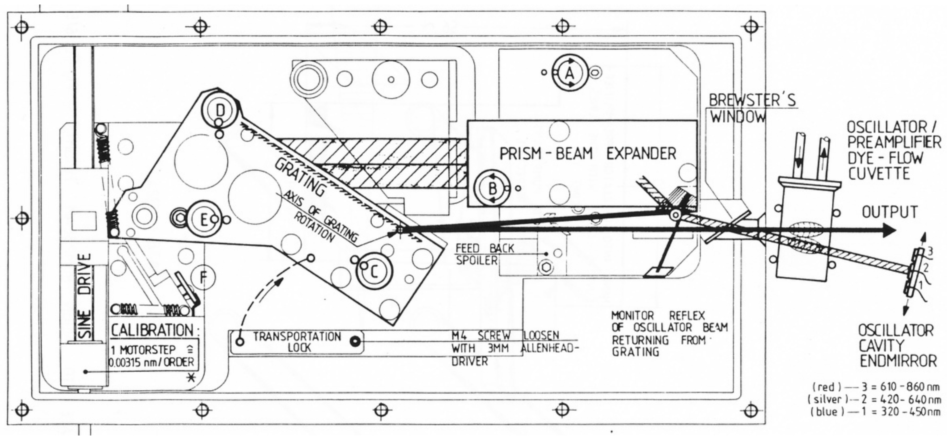

Figure 3.9.: Sketch of the resonator of the *Lambda Physik FL 3002* pulsed dye laser, showing the grating, the prism beam epxander, the flow cuvette and the cavity end mirror (from [32])

Figure 3.9 shows a sketch of the resonator. The pump beam excites the laser transition in the flow cuvette (*CV1*). The dye laser beam is reflected on the right end of the resonator by the cavity end mirror (*OCFM*) - which can be adjusted, depending on the dye used, to different wavelength ranges: Blue: 320-450 nm, silver: 420-640 nm, red: 650-860 nm. The beam is guided back through the cuvette (*CV1*) - indicated by the lower, hatched line - into the prism beam expander (*PBE*). This denotes a set of prisms used to widen or expand the beam so that it covers a large area of the grating - indicated in the sketch by the broad, hatched line leaving the prism beam expander on the left side and reaching the grating, which is aligned in a 'Littrow configuration' (the interested reader may refer to Appendix A for a detailed explanation).

The extraction of the laser beam from the resonator happens at the lower right corner of the prism beam expander. Another small prism, which is indicated in Figure 3.9 by a small, hatched area, allows some of the laser light to be reflected directly onto the axis of rotation of the grating - in this point the optical path does not change when the grating is rotated - and back into the flow cuvette at the height where the preamplifier beam hits the cuvette. Another small part of the beam is reflected by the prism on a small square below the prism beam expander, serving as a 'monitor reflex' to adjust the laser path through the resonator.

The second part of the pump beam, passing through *SPM1*, is reflected by the folding mirrors *FM1* and *FM2* and then split by the preamplifier beam splitter (*SPM2*). 10 % of the reflected light is again focused into the cuvette (*CV1*) by the preamplifier focusing lens (*PAFL*) at the height where the laser beam passes through the cuvette (cf. explanation above). The pump laser beam creates a population inversion at this point in the dye. The dye laser beam from *CV1* then causes a stimulated emission, hence this step works as an amplification (cf. explanation below).

The last part of the pump beam, which passes through mirror *SPM2*, is reflected by the folding mirror *FM3* and focused through the amplifier focusing lens (*AFL*) into the amplifier cuvette

(*CV2*), another dye-flow cuvette. This is the second step of the laser amplification. The amplifier cuvette resembles a second gain medium which is pumped (i.e., a population inversion is created) by the pump beam coming from *FM3*. In contrast to the actual gain medium, the stimulated emission in the amplification gain medium is not triggered by internal effects, but rather by an external signal, that means in this case the laser light coming from the first cuvette (*CV1*), this further amplifies the light.
Between the resonator output (*OCFM*) and the amplifier cuvette (*CV2*), a lens combination consisting of an ocular lens (*OCL*) and an objective lens (*OBL*) has been built in. This system acts as a Galilean telescope and expands the laser beam coming from the oscillator/preamplifier cuvette (*CV1*) to fill the cross Section of the amplifier cuvette (*CV2*). It also steers the laser beam along the optical bench. At the very end of the beam path, an iris diaphragm has been installed to cut off scattered light.

Operation:

Two important and basic operation modes of the laser have been used in the experiments and will be shortly described here. Both are quite straight forward to use. The on-off switch is located at the bottom of the control panel at the right side. See [32] for more information.

- To set the laser to a certain wavelength, press ‘SET’, enter the wavelength in nm and press ‘EXE’.
- To scan the laser over a certain range of wavelength, press ‘CONT SCAN’, enter the start wavelength, the final wavelength and the step width, always followed by ‘ENTER’ (three additional options can be set ‘DELAY’ - time the laser pauses after each scan, ‘SCAN’ - the number of scans which will be taken and ‘STOP SCAN’ - switch to manual) - the scan is started by pressing ‘EXE’. To pause and start the scan again, press ‘STOP/ CONT SCAN’, to stop the scan and restart from the beginning press ‘BREAK’ to stop and ‘EXE’ to start again, with the settings entered before.

CHAPTER 4

Detection Techniques

This Chapter explains the two detection methods used to obtain the results presented in Chapter 5. The emphasis lies on the REMPI-TOF mass spectrometry since this method has been used to obtain most of the results presented in Chapters 5 and 7.

4.1. LIF Spectroscopy

Laser Induced Fluorescence spectroscopy is a well established spectroscopic method, using laser light and a detector such as a photomultiplier (PMT).

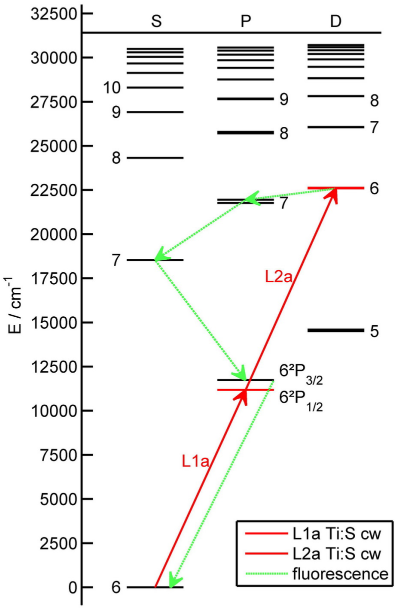

Figure 4.1.: Schematics of Laser Induced Fluorescence spectroscopy on the example of a free Cs atom. The valence electron of the caesium atom is excited from its ground state $(6^2S_{1/2})$ to upper states $(6^2P_{1/2}$ and $6^2D_{3/2})$ in two steps by two Ti:Sa lasers, denoted by the red arrows. The excited state is not stable and the electron relaxes back into its ground state via various fluorescence channels. One of the possible channels is denoted by the green arrows.

Figure 4.1 shows a sketch of the principle of this method on the example of a bare caesium atom, excited with two Ti:Sa laser. The laser light excites the valence electron of the caesium atom from its ground state ($6^2\mathrm{S}_{1/2}$) to the first excited state ($6^2\mathrm{P}_{1/2}$). In order to do so, the laser needs to have exactly the energy of the transition (in this case 1.39 eV corresponding to a wavelength of 894.6 nm or $11178.27\,\mathrm{cm}^{-1}$) and the transition has to be allowed (cf. Section 2.4.2).
The excited state has a certain lifetime and the electron will relax back into lower energy levels after some time. The lower energy levels to which the electron can relax to, depend on the one hand on the electronic transition rules - not all transitions are allowed - and on the other hand on the kind of atom. In the example shown in Figure 4.1, the electron in the $6^2\mathrm{P}_{1/2}$ state has been further excited to the $6^2\mathrm{D}_{3/2}$ state. The electron can now relax back into the ground state ($6^2\mathrm{S}_{1/2}$) through different fluorescence channels (e.g., $6^2\mathrm{D}_{3/2} \rightarrow 7^2\mathrm{P}_{3/2} \rightarrow 7^2\mathrm{S}_{1/2} \rightarrow 6^2\mathrm{P}_{3/2} \rightarrow 6^2\mathrm{S}_{1/2}$). Some other channels are allowed, but some are forbidden by transition rules, cf. Section 2.4.2. Each relaxation of the electron to a lower energy level releases a photon of exactly the energy of the difference between the two levels. The fluorescence photon is detected by a photomultiplier. Since the wavelength of the laser is known, the energy difference between the two levels is known.

Since laser light is highly monochromatic, this method allows a very exact investigation of the electronic energy levels. For bare atoms, even the hyperfine structure can be investigated by slightly tuning the wavelength of the laser. Tuning over a larger range of wavelength leads to the excitation of other (higher or lower) energy levels. The tuning range depends on the laser type. As explained in Chapter 2, the transitions of atoms on helium atoms are broadened, hence the hyperfine structure of the levels can in general not be resolved. However, LIF spectroscopy is a good method to measure the shift of transitions of atoms on the helium droplet as compared to bare atoms.

4.2. REMPI-TOF Spectroscopy

Resonance Enhanced Multi Photon Ionisation Time-Of-Flight spectroscopy is a spectroscopic method using laser light of two pulsed lasers and a time-of-flight mass spectrometer as a detector. In the case of the following description, the method can also be called R3PI TOF, referring to resonant-3-photon-ionization.

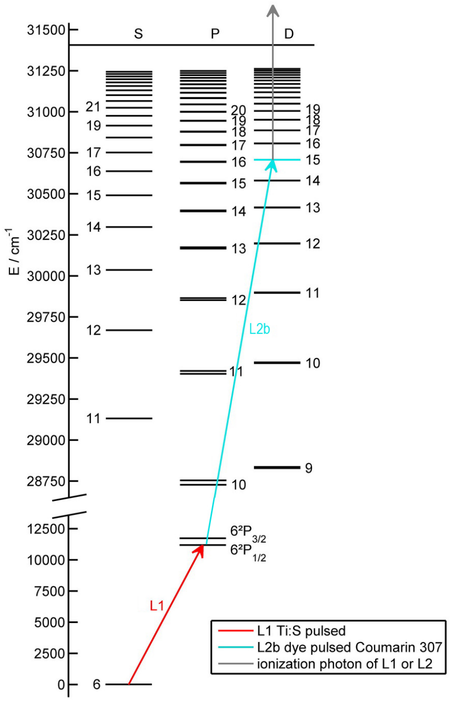

Figure 4.2.: Schematics of Resonance Enhanced Multi Photon Ionisation Time-Of-Flight mass spectroscopy on the example of a bare Cs atom. Two pulsed lasers, denoted by the red and cyan arrows, are used to excite the valence electron of the caesium atom from its ground state ($6^2S_{1/2}$) via the first excited state ($6^2P_{1/2}$) into a highly excited state ($15^2D_{3/2}$). In the next step, a photon of one of the two lasers ionizes the caesium atom (denoted by the grey line). The ion is detected by the TOF mass spectrometer.

With this technique, the investigated atoms are ionized in several steps by laser light. Figure 4.2 shows an example of the REMPI-TOF scheme applied to a bare Cs atom. In the first step, one laser (*here:* pulsed Ti:Sa) excites the electron to a higher state ($6^2P_{1/2} \leftarrow 6^2S_{1/2}$), the second laser (*here:* Lambda Physik pulsed dye) is scanned and excites the electron from the first excited level to a very highly excited level (e.g., $15^2D_{3/2} \leftarrow 6^2P_{1/2}$). From here another photon of one of the two laser excites the electron over the ionization threshold, hence ionizing the atom. The ion is detected by the multi channel plate (MCP) of the TOF in reflectron mode.
The second step of this scheme only happens if the second laser can excite a high level, that means if the wavelength of the laser matches the energy difference between the first excited level ($6^2P_{1/2}$) and the upper energy level (e.g., $15^2D_{3/2}$) and the transition rules are fulfilled. Hence, when scanning the second laser, a peak shows when the laser excites an upper level.
In case this method is applied to atoms on helium droplets, additional effects such as line broadening due to the interaction of the atom with the droplet as well as different transition rules have to be taken into account.

4.3. Setup

Figure 4.3 shows the laser setup for the REMPI-TOF experiments. The single elements have been described in Chapter 3, page 23.

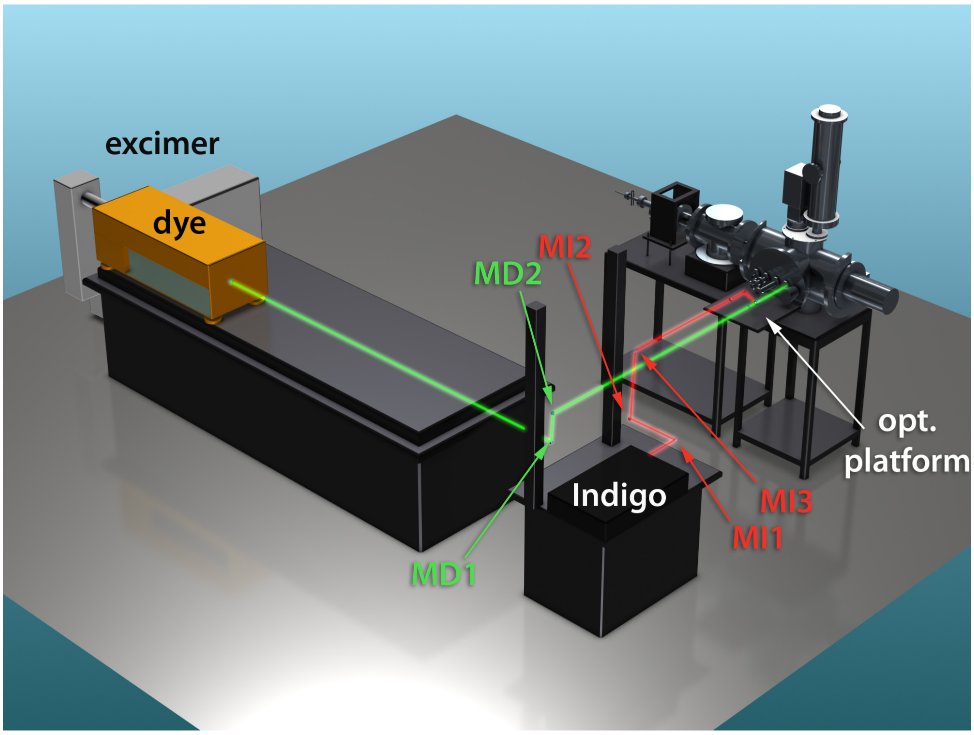

Figure 4.3.: CAD drawing of the laboratory setup including the source, pickup and detection vacuum chambers as well as the lasers used for the REMPI-TOF experiment. These are the Excimer pumped pulsed dye laser and the Nd:YVO4 pumped, pulsed Ti:Sa laser (Indigo). MI1-MI3 and MD1-MD2 denote the laser mirrors for the dye laser beam (green line) and the Ti:Sa laser beam (red line).

Two pulsed lasers were be used to perform the a REMPI-TOF spectroscopy. On the one hand because the TOF mass spectrometer need start pulse at which the time of flight measurements start. The Nd:YVO4 pumped pulsed Ti:Sa laser, in the following text denoted as ‘Indigo’ and the Excimer pumped pulsed dye laser, called ‘Lambda Physik’ in the following, were used.

The beam of the Lambda Physik laser was guided via two mirrors (MLP1 and MLP2) onto the optical platform (cf. Figure 4.4) at the level of the entrance windows of the detection chamber. The mirrors are of the type *Edmund Optics, TechSpec Precision Broadband Laser Mirrors, V45-596.* According to their specifications, they have reflectivity of >99 % at a wavelength of 400-700 nm and their damage threshold lies at: At 10 J/cm^2 for 10 ns pulse (and at 500 kW/cm^2 cw).

The laser beam of the Indigo was guided onto the optical platform (cf. Figure 4.4) via the mirrors MI1-MI3 (all MI mirrors are of the type *Thorlabs BB1-E02* according to [45]). At the platform, the beams were further manipulated. The Indigo beam polarization was turned by 90 ° by a $\lambda/2$ waveplate (L2P) and then reflected via mirror MI4 into the Glan-Taylor prism at an angle of 70 °. The prism is of the type *Bernhard Halle Nachf. GmbH; PGH15.* According to its specifications, its spectral range is 350-2700 nm, the damage threshold is 300 MW/cm^2 for ns pulses.

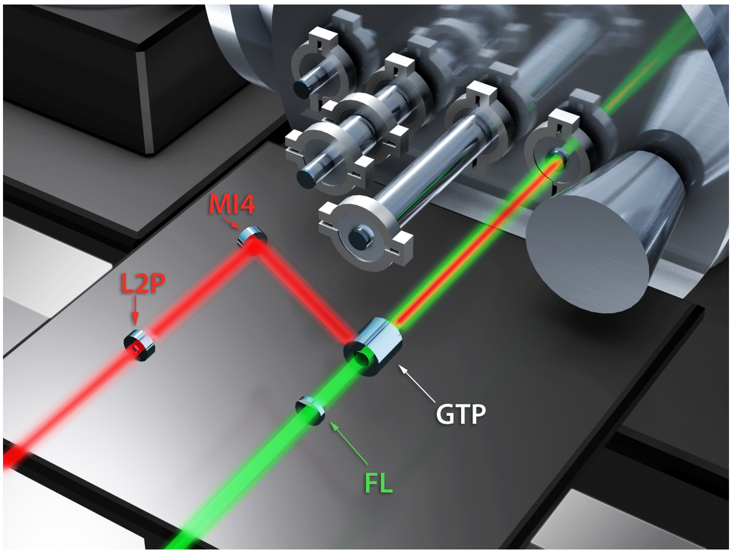

Figure 4.4.: Close-up of the optical platform denoted in Figure 4.3. The following optical devices are labelled: L2P denotes the $\lambda/2$ wave-plate, MI4 a mirror for the Indigo laser beam (red line), FL denotes the focusing lens for the Lambda Physik laser beam (green line) and GTP denotes the Glan-Taylor prism.

The laser beam of the Lambda Physik laser had a diameter of around 0.5 cm at the location of the Glan-Taylor prism, because it is slightly divergent at the dye laser output. Thus it had to be focused. Tests showed that the best signal was achieved with a lens with a focal length of 2 m, positioned at a distance of ≈74 cm from the helium beam axis.

The beams are overlapped with a Glan-Taylor prism and then enter the detection chamber through a glass window and cross the helium nanodroplet beam at an angle of 90 ° right between the extraction field plates of the TOF mass spectrometer.

The Detail Box

Glan-Taylor Prism

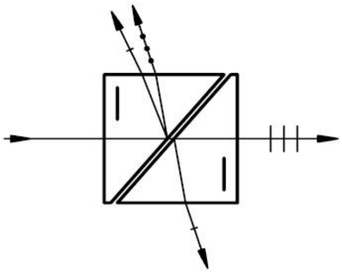

Figure 4.5.: Sketch of a Glan-Taylor prism (from Ref [6]).

A Glan-Taylor prism consists of a set of two calcite prisms separated by an air-gap and it is used as a polarizing beam-splitter. Common beam splitting cubes are cemented together (by Canada balsam or synthetic polymers), their advantage is that a beam is split into two halves, one going straight through the prism, the other being reflected back at a 90 ° angle, depending on their polarization. However, these prisms are not suitable for pulsed lasers since they would burn the cement. Glan-Taylor prisms are separated by an air-gap (cf. Figure 4.5), hence they can also be used for pulsed lasers.

The prisms are made of a birefringent material (e.g., calcite), that means they have a different refraction index for different polarizations. In the Glan-Taylor prism, the s-polarized beam is totally reflected by the internal surface of the first prism. The p-polarized beam is partly transmitted through the prism and partly reflected by both prism surfaces at the air-gap.
Note: The term 'S-polarized' origins from 'senkrecht', German for 'perpendicular', and denotes a wave polarized perpendicular to the plane of incidence which is spanned by the propagation vector of the wave and the surface normal vector of the reflecting surface. Correspondingly, p-polarized origins from 'parallel' and denotes the beam polarized parallel to the plane of incidence.
Considering the working principle of the Glan-Taylor prism, it can also be used to overlap beams, by guiding an s-polarized and a p-polarized beam into the prism.

Overlapping of Laser Beams:
The local overlapping of two laser beams is straight forward: An additional mirror was installed between the Glan-Taylor prism and the chamber. This mirror reflected the two beams onto a sheet of paper, mounted at the same distance from the mirror as the helium beam approximately would be. The two beams can simply be overlapped by alternately blocking one laser beam and adjusting the folding mirrors (e.g., MI3 and MD2). The focus of the dye laser beam can be adjusted the same way, by checking with a sheet of paper where the beam focus is along its path and measuring the distance from the mirror to the focus.

More of a problem is the temporal synchronisation of the two laser beams, since both are pulsed. The Indigo has a pulse duration of 30 ns and a repetition rate of 5 kHz, while the pulse duration of the dye laser is 26 ns and the repetition rate used was 100 Hz.
It proved that the best way to synchronize the beams is to trigger the Excimer pump laser with the Indigo laser. However, since the frequency of the Indigo laser is much higher than the fre-

quency of the dye laser, an electronic trigger unit was built by the in-house electronic workshop. This trigger is fed with the signal of the Indigo laser and creates two short TTL pulses with a frequency of 100 Hz. These output signals of the trigger unit function as an external trigger for the charge and discharge of the capacitors in the Excimer laser (cf. Section 3.4.1 and Appendix A.2 for more information).

This way the external trigger unit synchronizes the laser beams. Additionally, the phase shift of the input signal and the output signal of the trigger unit can be adjusted in 10 ns steps. The signal of the external trigger has to be delayed by $\approx 4\,\mu$s because the start signal and the actual starting point of the Indigo laser are not simultaneous.

CHAPTER 5

Results of Spectroscopy on Cs doped Helium Nanodroplets

Previous to this work Florian Lackner [31] has investigated Cs doped helium nanodroplets with LIF spectroscopy. He achieved to excite Cs from the 7P states up to the 10D (Δ) state, by either direct or two photon excitation. The upper limit of the excitation was limited by the cw dye-laser wavelength (Nd:YAG SHG pumped Rh 560).
In the course of this work, we successfully used REMPI-TOF spectroscopy to further excite Cs doped helium droplets from the 10P (Π) states to the ionization threshold. States up to the 20S state could be resolved. The combined results of these experiments has been published in [31]. In this Section, the achieved results with the help of REMPI-TOF spectroscopy will be explained.

The measuring techniques as well as the setup have been explained in the Chapters 3 and 4, however some details have to be added: The working principle of REMPI-TOF spectroscopy has been presented above. Its application is shown in Figure 5.1, which gives, in combination with Table 5.1 a detailed description as to which lasers were used for which excitation.
As a short reminder: For the REMPI-TOF experiment the laser beam of the Excimer pumped pulsed dye laser *Lambda Physik FL3002* - 26 ns pulse duration, 100 Hz repetition rate - and the laser beam of the pulsed Ti:Sa laser *Coherent Indigo S* - 30 ns pulse duration, 5 kHz - were overlapped (Glan-Taylor prism) and synchronized (home made trigger). A *Jordan D-850 AREF* time of flight mass spectrometer was used for the ion detection. A time-resolved counter type *Stanford Research SR 400*, triggered by the home made trigger device, was used to count the pulses of the MCP of the TOF mass spectrometer. The best signal was obtained for a mass range of Cs-He$_n$ (n=1-8).

Table 5.1.: Summary of the lasers used in the experiment. The wavenumbers and the observed transitions in the spectrum in Figure 5.2 are given. For the sake of clarity, atomic nomenclature is used. The total angular momentum is only denoted for the $6^2P_{1/2}$ state.

laser	active medium	mode	wavenumber (cm^{-1})	observed transitions
L1a	Ti:S	cw	fixed: 11197	$6^2P_{1/2} \leftarrow 6^2S$
L1b	Ti:S	pulsed	fixed: 11197	$6^2P_{1/2} \leftarrow 6^2S$
L2a	Ti:S	cw	11300-13500	$6^2D \leftarrow 6^2P_{1/2}$, $8^2S \leftarrow 6^2P_{1/2}$
L2b	DCM	cw	14500-16100	$8^2P \leftarrow 6^2P_{1/2}$, $7^2D \leftarrow 6^2P$, $9^2S \leftarrow 6^2P_{1/2}$
L2c	rhodamine 6G	cw	16400-17500	$9^2P \leftarrow 6^2P_{1/2}$, $8^2D \leftarrow 6^2P_{1/2}$, $10^2S \leftarrow 6^2P_{1/2}$,
L3	Ti:S	pulsed	21000-22850	$7^2P \leftarrow 6^2S$
L4a	Coumarin 153	pulsed	17500-19150	11^2P states to 14^2S state
L4b	Coumarin 307	pulsed	19150-20400	14^2P states to the ionization threshold

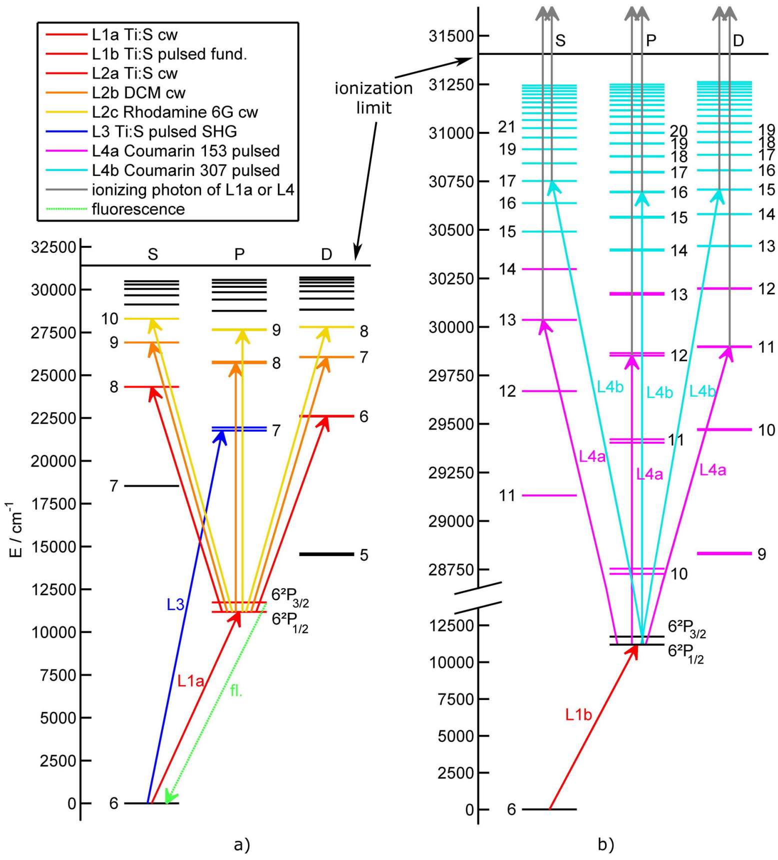

a)

b)

Figure 5.1.: Energy level diagram of the bare Cs atom a) LIF excitation. The arrows refer to the lasers used for the corresponding transitions. The type of laser is described in the legend and further in Table 5.1. For the second excitation the lasers L2a, L2b and L2c were used, indicated by the colour code. Laser L3 indicates the direct excitation of the 7P states (blue arrow). Fluorescence light is detected from the $6^2P_{3/2} \rightarrow 6^2S_{1/2}$ transition (dashed green arrow), with the help of a filter and a photomultiplier tube (PMT). b) REMPI-TOF excitation. As before, the arrows refer to the lasers used for the corresponding transitions. The levels have been colour coded, all levels of one color have been excited with the same laser dye. The gray arrows denote the ionizing photon.

Figure 5.2 shows the complete absorption spectrum of Cs doped helium nanodroplets obtained with the aforementioned methods. The green and red curves have been obtained with LIF spectroscopy, where the first denotes states excited directly and the latter denotes states excited with two photons via the non-desorbing $6^2\mathrm{P}_{1/2}$ ($^2\Pi_{1/2}$) state. The signal of the two photon excitation is a difference signal of the signal obtained with both lasers and the signal obtained with the second laser L2 only (exciting from the $6^2P_{1/2}$ state upwards). States from the 7^2P states up to the 10^2D (Δ) state have been investigated with LIF spectroscopy, however they are only plotted up to the 10^2S state.
The blue curve shows the result of the REMPI-TOF measurements, where again the $6^2\mathrm{P}_{1/2}$ ($^2\Pi_{1/2}$) state was used as a first excitation step. The results of this method have been connected to the LIF spectrum and cover the range from the 10^2P states to the ionization threshold.
The straight lines refer to the literature values of the corresponding states of a bare Cs atom. The red points denote bare Cs lines measured during the experiment, because some Cs atoms fall of the droplet and hence account for a bare atom signal. The zero point of the vertical axis is the energy of the bare-atom $6^2\mathrm{P}_{1/2}$ state. The dashed line indicates the ionization threshold of bare Cs, corrected for the electrical field between the TOF mass spectrometer extraction field plates.

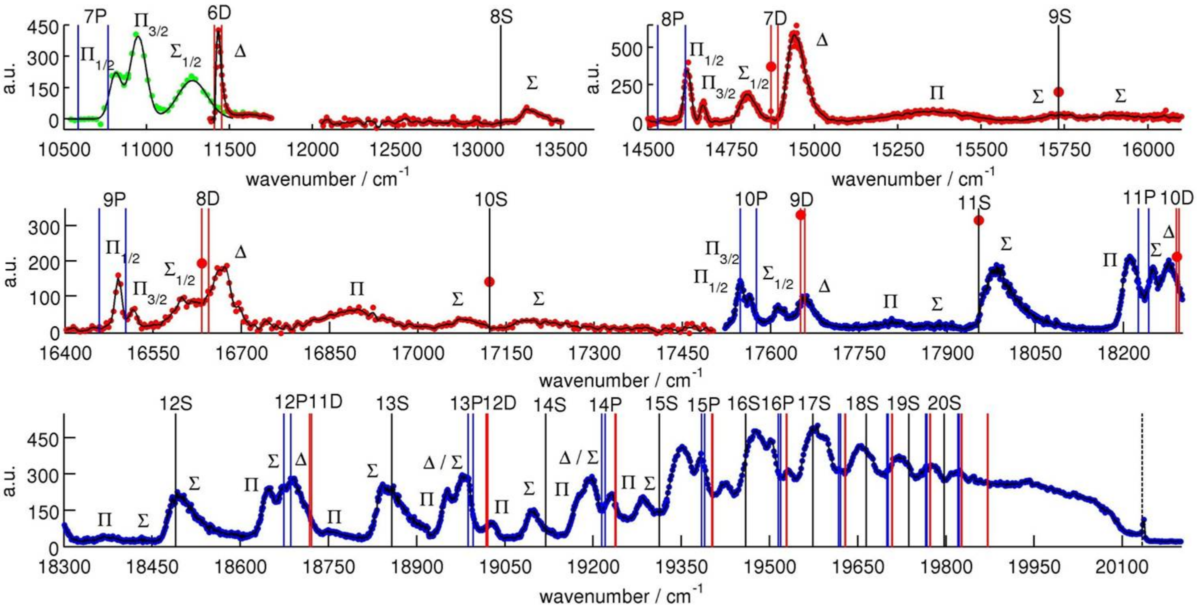

Figure 5.2.: Absorption spectrum of Cs doped helium droplets obtained with LIF and REMPI-TOF measurements. The green line denotes directly excited states with LIF spectroscopy, the red line two photon excited states with LIF spectroscopy and the blue line denotes states excited with REMPI-TOF spectroscopy. The straight lines are literature values for corresponding bare atom Cs states. The red points denote bare Cs states measured during the experiments. The zero point of the vertical axis is the energy of the $6^2\mathrm{P}_{1/2}$ state. The dashed line indicates the ionization threshold of bare Cs, corrected for the electrical field between the TOF spectrometer extraction plates.

Deducing from results with Rb doped helium droplets [61], the second excitations step, from the $6^2\mathrm{P}_{1/2}$ ($^2\Pi_{1/2}$) state upwards can be viewed as an excitation from the lowest vibronic state [62]. However, the Cs atom is still weakly bound to the helium when excited into the $6^2\mathrm{P}_{1/2}$ ($^2\Pi_{1/2}$) state, so the starting point for further excitations lies lower in energy by a few wavenumbers than the bare atom $6^2\mathrm{P}_{1/2}$ state.

Interpreting the results

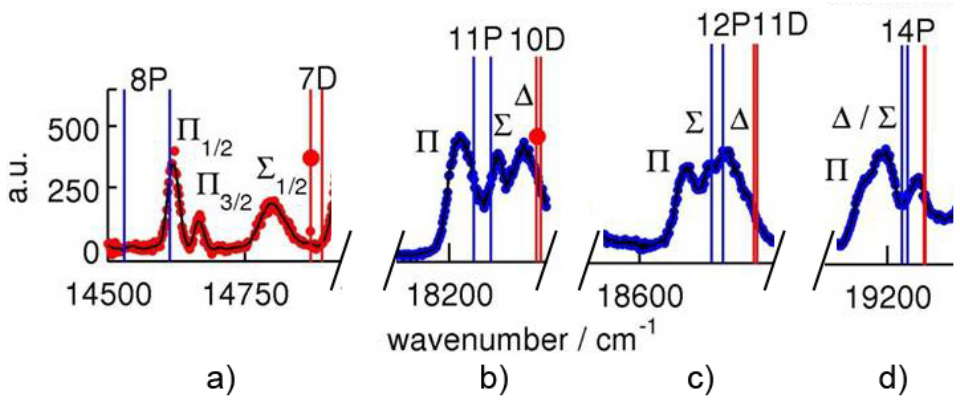

Figure 5.3.: Cs doped He droplets: examples of the spectrum of Cs doped He droplets depicted in Figure 5.2 to display the increasing broadening and merging of the peaks for higher excitations.

General:
As can be seen in Figure 5.3 a), the peaks are blue-shifted and broadened. For higher excitations (cf. Figure 5.3 b-d) the peaks merge. Hence we also change the denotation from Hunds *case (a)* used in Figure 5.3 a) to the molecular denotation (spin-orbit coupling is neglected, since the droplet induced broadening is larger) used in Figure 5.3 b)-d). The pseudo diatomic model describes the results in Figure 5.2 very well. Besides the fact that the peaks can be assigned to the corresponding diatomic states, it is further confirmed by transitions only possible in molecules. For instance according to the electric dipole selection rules for bare atoms ΔL$= \pm1$ transitions with ΔL=0 are forbidden. This changes for diatomic molecules, where the selection rules are $\Delta\Lambda = 0, \pm1$ and $\Delta\Omega = 0, \pm1$. In a diatomic molecule, it is hence possible to excite from the $6^2\mathrm{P}_{1/2}$ ($^2\Pi_{1/2}$) state into upper nP (Π, Σ) states, which is not possible in bare atoms. nP states obviously appear in the spectrum in Figure 5.2, which further confirms the pseudo diatomic model. Note that the blue shift of lower excitations changes to a red shift for higher excitations. We will look at this more closely further down in this Section.

S States:
The largest difference between LIF and REMPI-TOF spectroscopy is visible at the S states of the spectrum. With LIF spectroscopy the S (Σ) peaks are very weak in intensity and hence hard to detect. Their intensity even decreases for higher excitations. This is because the higher the excitation, the more fluorescence paths are possible, that means more possibilities exist for the excited atom to relax back into the ground state without being detected (only the fluorescence light from the $6^2\mathrm{P}_{3/2} \rightarrow 6^2S_{1/2}$ emission is detected by a PMT via an optical filter - max. transmission $\lambda = 8521\,\text{Å}$, FWHM$= 4\,\text{Å}$). With the REMPI-TOF method every excited state which can be ionized is detected. The S (Σ) peaks detected with the REMPI-TOF method are higher in intensity and can be resolved up to the 17^2S (Σ) state.

P States:
Corresponding to the pseudo diatomic model explained in the theory above (cf. Chapter 2), the lower P states split into three states: $^2\Pi_{1/2}$, $^2\Pi_{3/2}$ and $^2\Sigma_{1/2}$. This allows us to use Hund's *case (a)* for their labelling. Figures 5.3 a)-d) show the P states for increasing principle quantum

number n. For higher n, the peaks begin to merge. At the 11^2P state the spin-orbit coupling is already lower than the droplet induced broadening, hence the notation is changed from Hund's *case (a)* to molecular notation and only the Λ value is given. The trend to merge continues and for very high excitations such as the 14^2P state, the Δ and Σ peaks can not be distinguished anymore and the Π peak is only visible as a shoulder of the Δ/Σ peak.

D States:
For the D states the droplet induced broadening is always larger than the spin-orbit induced splitting, hence they are all labelled with the molecular notations. As described by the pseudo diatomic model, the D states split into three states (neglecting the spin orbit splitting): Δ, Π and Σ. Their order of energy has been chosen on basis of calculations [7] to be $\Delta < \Pi < \Sigma$. For the Π and Σ states, however, the energetic order is not unambiguously clear [38,46,61]. For an unambiguous allocation of the states further theoretical investigations are necessary.
With the help of the REMPI-TOF method D states up to the 13^2D, state could be resolved.

Blue and Red Shift:
As mentioned above, the shift of energy goes from a blue-shift for lower excitations to a red-shift for higher excitations. This is depicted in Figure 5.4, which shows the shift of the peaks of Cs doped helium droplets compared to the bare atom state (0-line). The plot has been created by Gauss-fitting the on droplet peaks of the spectrum and measuring the distance between the centers of the Gaussians to the corresponding bare atom line. As can be seen, the change from blue- to red-shift with increasing excitation happens for all types of states. For S states at n>12, for P states at n>9 (Π) and n>11 (Σ) and for D states at n>9 (Δ) and n>11 (Π). The reason for the change in shift is not yet definitely known. From the experiments, one can conclude that at low excitations the interaction between the Cs and the helium droplet is repulsive, whereas for high excitations the Cs*-He potential has an attractive character. This means for higher excitations that it is easier to excite the Cs on the droplet than it would be with a bare atom. It is clearly visible in Figure 5.4 that the red shift of all states converges to the same value, which is the ionization threshold of Cs on the droplet.

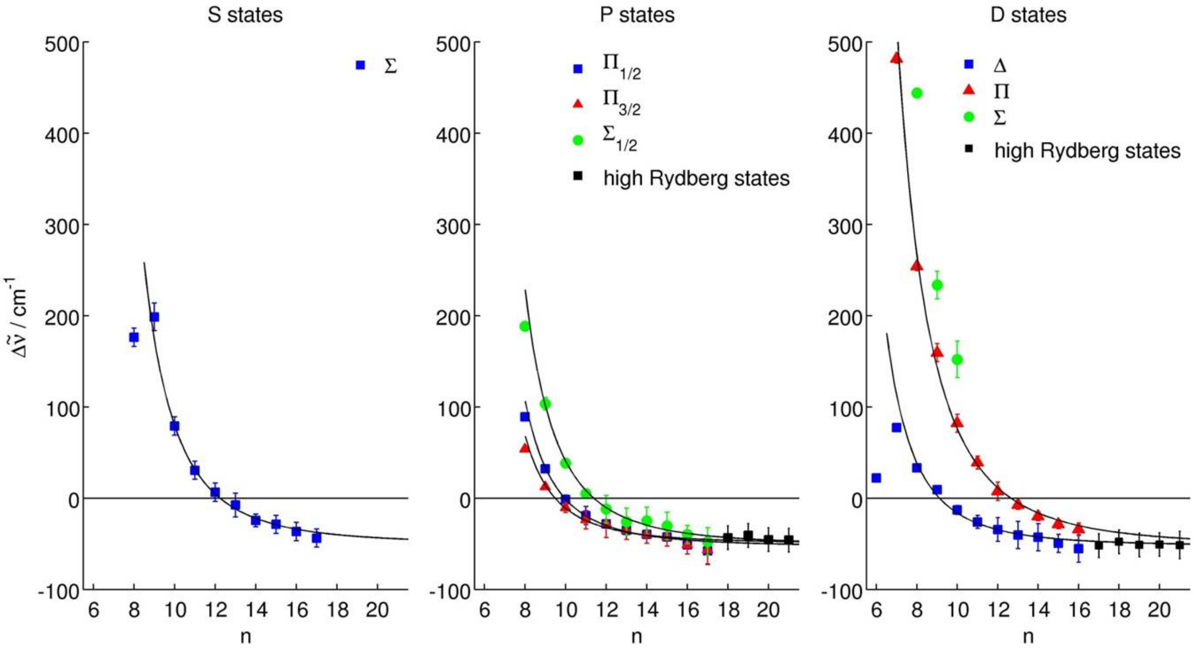

Figure 5.4.: Cs doped He droplets: spectral trends of the peaks. At low excitations the peaks of the Cs on the helium droplet are blue-shifted compared to bare Cs. For higher excitations the shifting decreases and finally crosses the excitation energy for bare Cs (i.e., it becomes red-shifted).

CHAPTER 6

Construction and Assembly of an Alkaline Earth Metal Pickup Cell

This Section explains the design, construction and assembly of a pickup cell for alkaline earth (Ake) metals in detail. It is structured as follows: First an overview of the requirements on the new setup is given. Then a simulation and first estimation of the necessary heating power is presented. After a short description of the test setup, the two approaches made to meet the requirements are discussed. The subsequent section describes the final setup and give the characterization results. The last two Sections give an overview of different methods of heating within a vacuum over a large temperature range and describe the installation of the new pickup system into the apparatus.

As mentioned above, in order to dope helium nanodroplets with atoms, a certain vapour pressure of the dopant has to be maintained within the pickup cell. For instance, for caesium and rubidium monomer (i.e., single atom) pickup the ideal (empirically determined) vapour pressure is in the range of $10^{-3} - 10^{-4}$ mbar. The temperature necessary to reach this pressure is ≈90 °C for Cs and ≈120 °C for Rb.
Figure 6.1 shows the vapour pressure as a function of temperature of the Ake metals magnesium (Mg), calcium (Ca), strontium (Sr) and barium (Ba)[1].

As can be seen in Figure 6.1, the necessary temperatures to reach a pressure of 10^{-4} mbar are considerably higher than for alkali metals. The required temperatures for the respective elements are:

- Mg: 320 °C
- Ca: 452 °C
- Sr: 393 °C
- Ba: 483 °C

---

[1] In this context these four elements are meant by 'alkaline earth metals', because beryllium (Be) is toxic and radium (Ra) is radioactive, hence they have not been taken into account here.

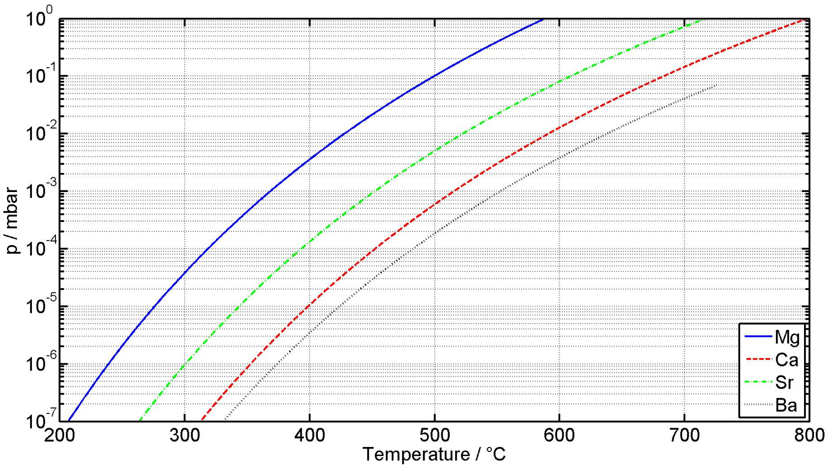

Figure 6.1.: Vapour pressure of the alkaline earth metals magnesium (Mg), calcium (Ca), strontium (Sr) and barium (Ba) as a function of temperature. Data from [37].

Since the alkali metal oven was not built to reach these temperatures, a new cell - including the heating system ('oven') - had to be designed, constructed and implemented in the existing apparatus described in Chapter 3. The requirements to the new setup were:

- The heating had to be designed to reach at least 600 °C, since there would probably be a temperature gradient between the oven and the pickup cell. Furthermore, the temperature for monomer pickup can not be determined exactly from the vapour pressure and the dopants might form an oxide layer which has to be removed by overheating, before a pickup is possible.
- The basic design was constrained by the existing apparatus and the suspension of the old pickup cell. Additionally, since the new cell should fit as a third cell between the alkali and the gas pickup cell, it had to be very small.
- The Ake metal pickup cell had to be thermally shielded to avoid heating of the environment, such as the other pickup cells, especially the alkali cell, which would lead to an undesired mix of elements.
- The new cell should have a faster temperature response than the old cell, which needed up to an hour to reach a temperature of 100 °C.

6.1. Simulation

The first step, before starting to design a new pickup system was to calculate how much heating power is necessary to reach the required temperatures and how hot the surrounding would get in the process of heating. In this case, it is sufficient to only take thermal radiation into account, because the other effects can be neglected within a vacuum. Especially for this simulation, which should only provide a rough estimation of the heating power necessary to maintain the required temperature. The heating power is, neglecting all other effect, equal to the radiation losses of the oven. Note that a heating system needs to provide more power than necessary to hold the heated object at the final temperature, to provide reasonable heat up times and cover potential losses. The radiation heat transfer between two objects (e.g, oven and chamber wall) can be calculated with the following equation [17]:

$$\dot{Q}_{rad} = \frac{\sigma(T_1^4 - T_2^4)}{\frac{1}{\epsilon_1} + \frac{A_1}{A_2}\left(\frac{1}{\epsilon 2} - 1\right)} A_1, \tag{6.1}$$

where $\dot{Q}_{rad}$ is the radiant power in $\mathrm{Wm^{-1}K^{-1}}$, ϵ_n are the emissivities of the materials of the objects 1 and 2[2], $\sigma = 5.67 \cdot 10^{-8}\,\mathrm{Wm^{-2}K^{-4}}$ is the Stefan-Boltzmann constant, T_n are the temperatures of the objects and A_n are the surfaces of the heated bodies[3]. Please note that the last factor of A_1 has the effect that the radiant power is not given in $\mathrm{W/m^2}$, but related to the actual size of the oven and hence given in W. The indices 1 and 2 in equation 6.1 refer to the two bodies between heat is exchanged, where body 1 is the hotter and body to the cooler.

The blue curve in Figure 6.2 shows the radiant power of a copper block (the pickup oven) with a surface of $A = 5.5 \cdot 10^{-3}\,\mathrm{m^2}$ as a function of temperature[4]. The problem is to find the correct values for the emissivities of the materials (copper and high quality steel). For instance, for copper the literature values range from 0.02-0.2 depending on its surface (polished-roughened) [37]. Assuming the worst case and because of the construction (explained below) the emissivity of the copper oven was set to $\epsilon_{ov} = 0.5$ and the emissivity of the high quality steel chamber wall to $\epsilon_w = 0.7$. The red curve in Figure 6.2 shows the result of the radiant power of a copper oven as a function of temperature, where the values described above were used in equation 6.1. At a temperature of $T_{ov} = 520\,\mathrm{C}^\circ$ the oven will radiate with approximately $\dot{Q}_{ovw} = 61\,\mathrm{W}$.

---

[2] The emissivity is a material constant which gives the ratio of the radiated energy of a certain material relative to that of a blackbody.

[3] Equation 6.1 simplifies to the commonly known: $\sigma\epsilon(T_1^4 - T_2^4)A_1$ for $A_2 >> A_1$. This is the case for the oven and the wall, but not for the oven and the radiations shield (see below).

[4] The surface size of the oven used in Section 6.4 has been used here.

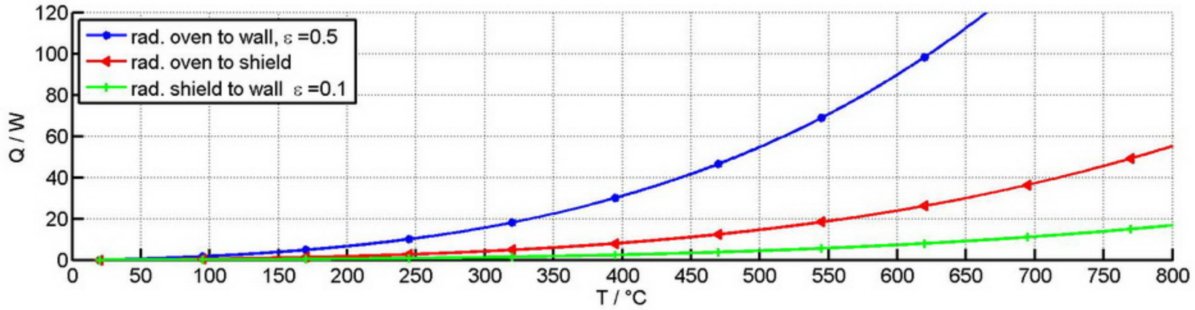

Figure 6.2.: Simulation of the temperature behaviour of the pickup oven described in the subsequent sections. The blue curve shows the radiant power between the oven and the chamber wall, the red curve shows the radiant power between the oven and the radiation shield and the green curve shows the radiant power between the radiation shield and the chamber wall.

An oven of this temperature will heat up its surrounding as well. Since the vacuum chamber in which the pickup oven had to be installed also contains heat sensitive electronic devices (e.g., the chopper motor) the oven had to be thermally shielded. This had the additional advantage of further reducing the heating power necessary to keep the oven at its temperature. This is because the radiation shield (RS) reflects some of the radiated heat of the oven back. Figure 6.2 shows the radiation power between the oven and the RS (red curve, $\dot{Q}_{ovrs}$) as well as the radiation power between the RS (made of polished copper) and the chamber wall (green curve, $\dot{Q}_{rsw}$) as a function of temperature. The corresponding emissivities were set to: oven: $\epsilon_{ov} = 0.5$, radiation shield: $\epsilon_{rs} = 0.1$ (polished copper) and chamber wall: $\epsilon_w = 0.7$ (cf. Ref [37]). The temperature and radiation power of the RS can be easily calculated, using the fundamental physical law, that a body will exchange heat with its environment until an equilibrium temperature forms. For the radiation shield this means that its temperature will settle at an equilibrium state where the radiation heat transfer to the shield (from the oven) is equal to the transfer away from the shield (to the wall), because the temperature of the oven and the wall can assumed to be constant.

$$\dot{Q}_{ovw} = \dot{Q}_{rsw} \tag{6.2}$$

For an oven temperature of $T_{ov} = 520\,\mathrm{C}^\circ$ this equilibrium temperature is still $T_{rs} \approx 260\,\mathrm{C}^\circ$ (cf. Figure 6.2). This can still be an issue for the surroundings of the oven. To cool the radiation shield it was planned to connect a thick copper cable to it[5] and conduct a part of the heat of the radiation shield via the copper cable and a feedthrough to the atmosphere side. The heat transfer of a copper cable can be calculated with following equation:

$$\dot{Q}_{trans} = \lambda A / l \Delta T, \tag{6.3}$$

where $\dot{Q}_{trans}$ is called heat flow rate, λ is the heat conductivity of a certain material in $\mathrm{Wm}^{-1}\mathrm{K}^{-1}$, A is the cross section of the conductor, l its length and ΔT the temperature difference between both ends of the conductor.

Using a length of $l = 0.4\,\mathrm{m}$ a heat conductivity of $\lambda = 240\,\mathrm{W/m}^{-1}\mathrm{K}^{-1}$ (low end for copper) and a cross section of $A = 75\,\mathrm{mm}^2$, gives a conducted heating power for the copper cable of about $\dot{Q}_{co} = 9\,\mathrm{W}$. The calculated heat radiation power of the radiation shield at $T_{ov} = 520\,\mathrm{C}^\circ$ is $\dot{Q}_{rs} \approx 4\,\mathrm{W}$, this means the copper cable could conduct all the heat of the radiation shield. However, the cooling of the shield by the copper cable affects the equilibrium condition between the oven, the shield and the wall, hence the copper cable leads to a new equilibrium condition.

---

[5] Copper has been chosen here because it has a very high heat conductivity.

The exact calculation is intricate and hence has not been done here, because a much easier estimation can be taken. If the copper cable is theoretically able to conduct all the heat of the radiation shield (i.e., $\dot{Q}_{ca} > \dot{Q}_{rs}$), the equilibrium condition changes from equation 6.2 to:

$$\dot{Q}_{ovw} = 2\dot{Q}_{rs}, \tag{6.4}$$

However, this is only valid as long as $\dot{Q}_{ca} > \dot{Q}_{rs}$. Using the new equilibrium condition, one can easily calculate the new heat from of the radiation shield by modifying equation 6.1. This calculation leads to a new temperature of the radiation shield of $T_{rsca} = 175\,\mathrm{C}^{\circ}$ if it is cooled by a copper cable.

6.1.1. Comparison with the Results

To show the quality of the simulation and calculation above, the results obtained with the final setup, explained in Section 6.7, will be compared with the theoretical results given above. At a measured oven temperature of 520 C° the temperature of the radiation shield was measured to be 183 C° without the copper cable connected and 94 C° with the cable connected. The heating power to hold the oven at this temperature was approximately 22 W.
The calculated heating power is too low (≈17 W, cf. Figure 6.2). This is due to the effect of the emissivities. The emissivity of the radiation shield (ϵ_{RS}) has a large influence on the heating power of the oven, but not on the temperature of the radiation shield (because it cancels out in the calculation). For instance, if ϵ_{rs} is set from 0.1 to 0.2, the calculated heating power increases to ≈24 W, which is close the actual value.

A comparison of the shield temperatures shows that the calculated temperatures (≈260 C° without and ≈190 C° with copper cable) are too high. They are affected by the emissivity of the oven (ϵ_{ov})[6].

Knowing how the emissivities influence the results, one can back-calculate to the emissivities which lead to the real results. This leads to $\epsilon_{ov} = 0.26$ and $\epsilon_{rs} = 0.26$ - these ϵ result in a heating power of ≈21 W and a temperature of the radiation shield of 194 C° without the copper cable and 140 C° with the copper cable connected. The latter temperature is still too high, but the other values are very close to the actual results. Surprisingly the emissivities are worse than those given for a roughened copper surface, even though the elements have been polished. However, a thin oxide layer may have built. This increases the emissivity considerably (literature values go up to $\epsilon = 0.88$ for copper with a thick oxide layer) [37].

It also has to be considered that the calculations above can only provide a rough estimation, because a lot of effects have not been taken into account. For example, the temperature of all elements is also partly conducted by their suspension.

In sum, the calculations provided only a rough estimation, especially because of the hard-to-estimate material properties (ϵ). However, the estimation served its purpose well and gave a first idea about the temperatures involved and heating power needed.

---

[6] The emissivity of the wall does not have any influence, because its influence is nearly nullified by the surface size of the wall in relation to the surface sizes of the oven and the RS.

6.2. Test Setup

Since the new pickup oven had to be thoroughly tested and characterized before it could be installed into the experimental setup, a test vacuum setup was constructed (cf. Figure 6.3).

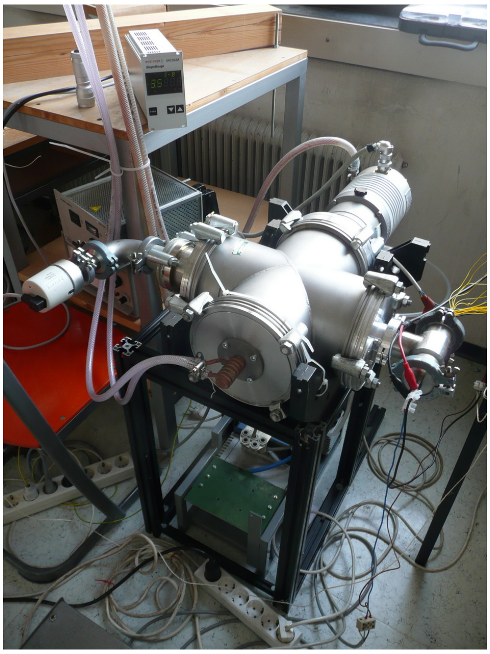

Figure 6.3.: Photo of the test vacuum apparatus.

The apparatus was pumped by a *Balzers MD 4 T* diaphragm vacuum pump and a water-cooled *Balzers TPH 180 H* turbo molecular pump, which both were controlled by a *Balzers TCP 310* electronic drive unit (the whole system is called *Balzers TSH 180 H - Turbo Molecular Pumping Units for corrosive gas processes*). According to the *Balzers Component Full Range Gauge* (as a display unit a *Pfeiffer Single Gauge TPG 261* was used) the lowest reached pressure within the vacuum chamber which could be maintained was in the lower range of 10^{-8} mbar.

The test suspension of the pickup simply consisted of an aluminium sheet metal holding the flange and the gas pickup with three M3 thread bars. Instead of an actual alkali metal pickup cell, a high quality steel plate was mounted at the back end of the alkaline earth metal pickup, referred to as ‘alkali metal dummy cell’ in the following.

The test setup of the oven (cf. subsequent Sections) had thermocouples connected to every vital point. One of the thermocouples was connected to the *Eurotherm* PID controller[7] used to control the temperature of the oven via a solid state relay[8]. All thermocouples were properly isolated and guided to the front of the setup (right end in Figure 6.3, where the temperature

---

[7] A PID controller is an electronic circuit control consisting of three elements (proportional-integrative-derivative) which adjust the actual value to the desired value. Each element has different characteristics and one parameter to adjust, these parameters define the behaviour of the controller (slow/fast approach, strong/little overshooting). A closer explanation can be found in the corresponding manuals. The parameters of the controller used for the setup in this work have been set by autotune (i.e., by the controller itself) at a temperature of 520 °C (the parameters are temperature depended).

[8] A solid state relay is basically an electronic switch. The SSR used in this work switches AC at the zero crossing of the voltage. By switching the supply current of a device on and off for a certain number of periods the power of the device can be controlled. Hence SSRs are commonly used as a link between controller and the load.

was low enough to connect the thermocouples to plugs and to connect them with common wires to the feedthrough (in this case a 15pin SubD plug, adhered to the mounting with epoxy resin). On the atmosphere side, the thermocouples were connected via another wire and plug to the respective thermocouple thermometers - a *Voltcraft K204 Datalogger* and a *Center 300 Type K Thermometer*.

6.3. The First Approach: Heater Cartridges

In a first approach, to reach all the requirements given above, a copper cylinder heated by heater cartridges was used. Our group successfully used heater cartridges in an experiment under the same conditions, although only up to 200 °C. According to their specification they would bear up to 700 °C, if the temperature is dissipated properly. In the first setup, three (*RS-Components*) heater cartridges with an effective power of 200 W[9] at a nominal voltage of 220 V, were press-fitted into the oven (see photo an CAD drawing in Figure 6.4). As a temperature control, a *Eurotherm 2116* controller connected to a *Crydom D2410* solid state relay was used. The high quality steel pickup cell was made to fit easily into the oven. The thermal shielding and suspension are explained in Section 6.5.

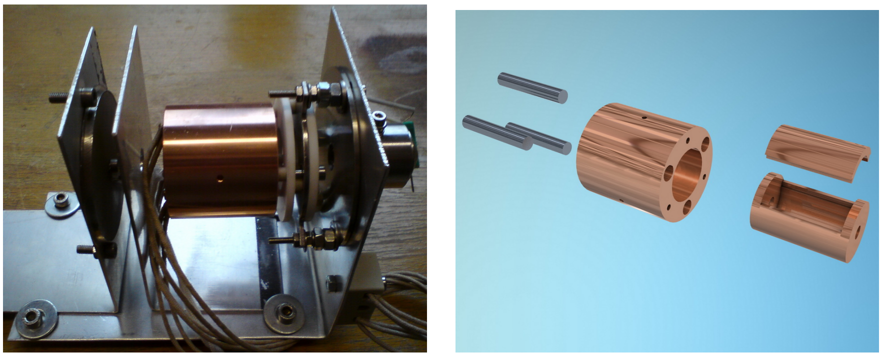
(a) (b)

Figure 6.4.: Photo (a) and CAD drawing (b) of the first setup of the alkaline earth metal pickup cell and its heating. Three heater cartridges were press-fitted into a copper block, serving as oven. The cell was made to fit into the cylinder easily. An *Eurotherm 2116* controller connected to a *Crydom D2410* solid state relay were used as a control unit.

First tests in a test vacuum apparatus at pressures in the range of $10^{-8} - 10^{-7}$ mbar and oven temperatures of up to 250 °C worked well. However, it was not possible to reach 500 °C, due to a short-circuit to ground. Several other experiments were made, using different control parameters at the *Eurotherm* controller. Unfortunately, all attempts ended up in a short-circuit, that means in a damage of one of the heater cartridges. The following explanation for this problem was found:

As can be seen in Figure 6.5, the heater cartridges consist of a heater wire (wound up to a coil) and a high quality steel shell. As an isolation material, magnesium oxide sand was pressed between the steel shell and the wire. The problem which caused the short-circuit to ground and subsequently the short-circuit was that the high quality steel shell was not sealed vacuum

---

[9] According to the simulation above (cf. Section 6.1), this power exceeds the necessary power to hold the oven at a temperature of 500 °C by far, however, for a fast heating more power is required and these cartridges were the best solution considering power, price and size.

proof. Hence, when in a vacuum, the cartridges would gas out and since air is a good heat conductor and vacuum a bad one, this decreased the heat conduction from the heater wire to the steel wall. The temperature feedback for the controller unit was connected to the oven, not to the heater wire itself, hence the controller unit did not slow down, or switch off the oven. As a consequence, the temperature of the heater wire could not be dissipated properly and at a certain temperature (≈350-450 °C) the heater wire burnt, leading to a short-circuit. However, this effect only showed slowly, especially at the lower end of the temperature range (≈350 °C). Only after several operation hours a connection in the range of MΩ between the heater wire and the shell of one cartridge could be measured. With further use the resistance of this connection decreased, ending in the destruction of the heater cartridge (a closer explanation is given in Section 6.10).

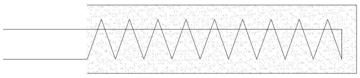

Figure 6.5.: Schematics of a heater cartridge.

6.4. The Second Approach: Thermocoax

A thermocoax (proper name) consists of a heater wire within a high quality steel shell and a MgO isolation. The main difference to heater cartridges - beside the fact that it comes in a wire instead of a cartridge - is that the ends can be sealed by hard soldering. The company guarantees the contacts to be vacuum proof up to a pressure of 10^{-6} mbar. This would not be sufficient for our experiment because the pressure in the pickup chamber is in the range of 10^{-8} mbar. However, our group made positive experiences in another experiment with a thermocoax in a vacuum with a pressures in the range of 10^{-11} mbar.

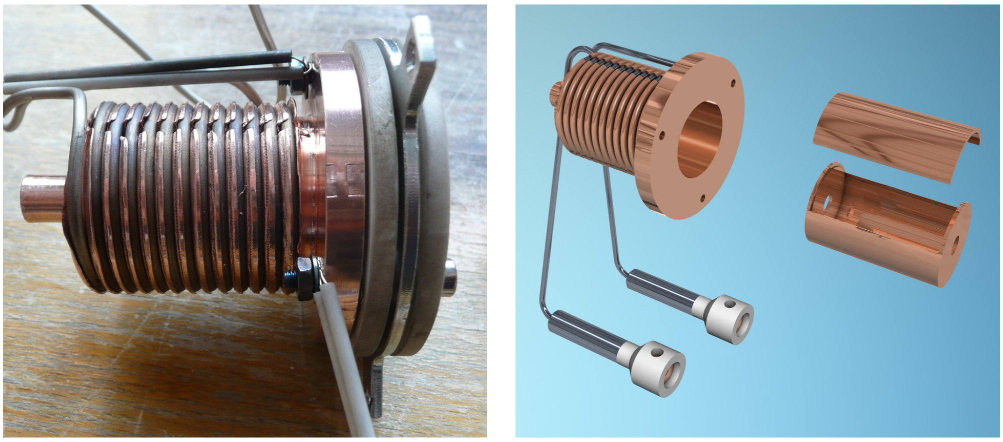

(a) (b)

Figure 6.6.: Photo (a) and CAD drawing (b) of the setup of the alkaline earth metal pickup cell using a thermocoax as a heater. The heater wire was pressed into a flute and wound around the oven. The cell fitted into the cylinder easily. As a controlling unit, an *Eurotherm* controller connected to a *Crydom D2410* solid state relay was used.

6.4.1. New Setup

The new design for the oven is shown in Figure 6.6. A flute was lathed into the copper cylinder serving as oven, then the thermocoax was press-fitted into the flute and wound around the oven. As a last step, the bar between two adjoining flutes was bent an pressed over the thermocoax. This technique provides a good thermal contact without using extra material such as brazing solder, which might evaporate at high temperatures and possibly spoil the vacuum and the pickup process.

Two small gaps have been milled into the oven before the thermocoax was mounted, to prevent air enclosures. An infrared camera *Marke Flir Typ i5* was used to check if these gaps produce hotspots, since the thermocoax has no connection to the copper at the gaps. Measurements at atmospheric pressure showed that the thermocoax at the gap was only slightly hotter (≈10 °C - cf. Figure 6.7), which is not posing a risk.

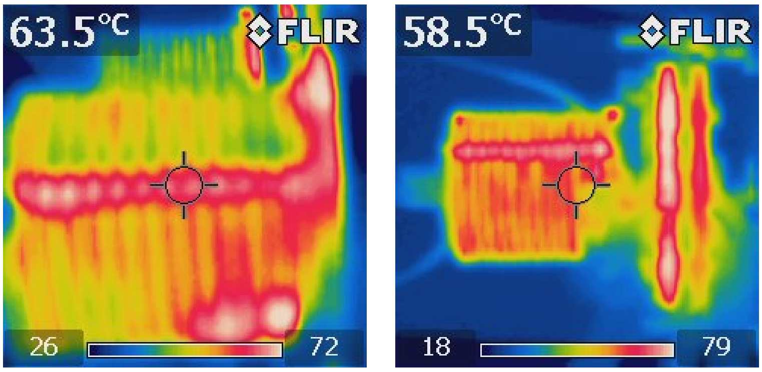

(a) (b)

Figure 6.7.: Photo of the alkaline earth metal pickup setup in the test setup (cf. Section 6.2) with an infrared camera in order to detect hotspots. As can be seen, the thermocoax is hotter above the gap, which has been milled into the oven to prevent air enclosure. However, a comparison to the scale at the bottom of each picture shows that the temperature difference is only around 10 °C, which is not critical. Note that the temperature values given in the scale are not very exact in absolute terms, they depend strongly on the absorption coefficient (i.e., on the material and its finishing).

6.4.2. Thermocoax Specifications

The specifications of the thermocoax used for this setup are: *Thermocoax SEI20/100*. This means the thermocoax is a high quality steel wire with a length of 2 m and a diameter of 2 mm. The heated part is 1 m long, the rest are non-heated 'cold ends'. At the end of these, two *CFG 20* connectors have been hard-soldered by the company workshop. These are ceramic connectors, suitable for vacuum.

6.4.3. Power Supply

The thermocoax also required a separate power supply (cf. Figure 6.8). The specifications state that the thermocoax has a resistance of 3.1 Ω, that means with a voltage of 40 V, a power of 500 W[10] is reached. Thus, while still using the *Eurotherm* controller and the solid state relay,

---

[10] This is, according to the simulation in Section 6.1 much more power than necessary to hold the oven at a temperature of even 500 °C, but for a fast heating more power is required and the chosen thermocoax was the best solution considering power, price and size.

an adjustable voltage supply had to be used to find the best power settings (i.e., the minimal power necessary to reach and hold 500 °C). This turned out to be ≈21 V resulting in a maximum heating power of ≈150 W.
To prevent the thermocoax from overheating, the maximum heating power of the controller was limited to 75 %, hence limiting the maximum power to 100 W. Measurements described in detail below showed that around 15 % (corresponding to ≈22 W) of the maximum heating power were necessary to hold the oven at a temperature of 520 °C in the final setup.

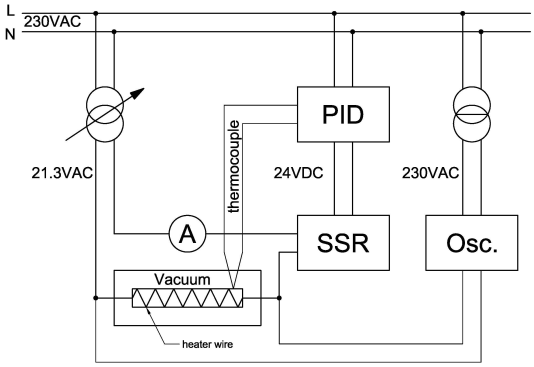

Figure 6.8.: Wiring diagram of the test setup of the alkaline earth metal pickup cell. The temperature of the thermocoax was controlled by a *Eurotherm* PID controller via a solid state relay. As a power supply a regulating transformer adjusted to 21.3 V was used. An ampere-meter was used to monitor the current and an oscilloscope was connected via an isolating transformer to monitor the voltage (cf. Section 6.10.4).

6.5. Thermal Shielding

The thermal shielding is very important to this experiment, since the alkaline earth metal pickup cell is mounted close to the alkali metal pickup cell, due to lack of space (cf. Figure 6.16). If the latter was heated by the thermal radiation of the first, it would lead to uncontrolled and undesired pickup of alkali metal atoms. Temperatures in the range of 80 °C are already enough to cause caesium to evaporate, while around 480 °C are needed to achieve the necessary vapour pressure of barium. Additionally, the suspension of the pickup cell should be thermally shielded as good as possible, in the first place, in order not to heat up the whole chamber and secondly to shield the gas pickup.
Please note: In this chapter the temperatures of the single elements of the setup are given in absolute values. Of course an uncertainty applies to all these values, mainly because of the uncertainty of the thermometer and the mounting of the thermocouples, but also because of other minor effects. The overall uncertainty of all temperature values given is in the range of ±3 °C.

The following steps were taken and proved to work best in order to thermally shield the Ake metal pickup cell properly (the abbreviations given in the listing below correspond to the labels in the Figure 6.9):

- The whole cell was shielded by a radiation shield (ORS) (called ‘oven shield’ in the following) in form of a polished copper cylinder put over the oven (Ov). This shield was connected by a 70 mm^2 copper cable to a copper feedthrough at the chamber wall (cf. Figure 6.10).

- In direction of the alkali metal cell (AkC) an additional radiation shield (AkRS) made of polished copper was installed.
- The suspension (Fl) of the oven was thermally decoupled by two MACOR discs (Mc) (ceramics used for electrical an thermal shielding - heat conductivity of 1.4 $\mathrm{W m^{-1} K^{-1}}$ [37]), which pinch the flange. Thus, the screws which hold the oven do not touch the flange. The MACOR discs also serve as a thermal shielding for the gas pickup cell (GasC).
- Between the MACOR discs, the oven and the flange spacers of high quality steel have been inserted, since they have a low heat conductivity (in the range of 15-90 $\mathrm{W m^{-1} K^{-1}}$ [37] depending on the alloy). The spacers create a small distance between the single elements of the setup and since the whole setup is operated within a vacuum, the single elements are thermally shielded by vacuum, which obviously does not conduct heat.

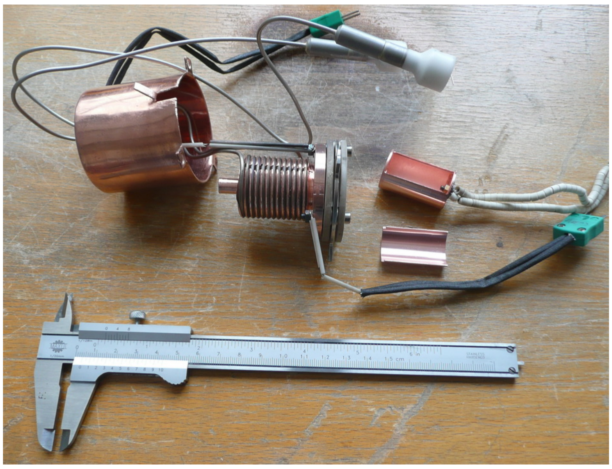

(a)

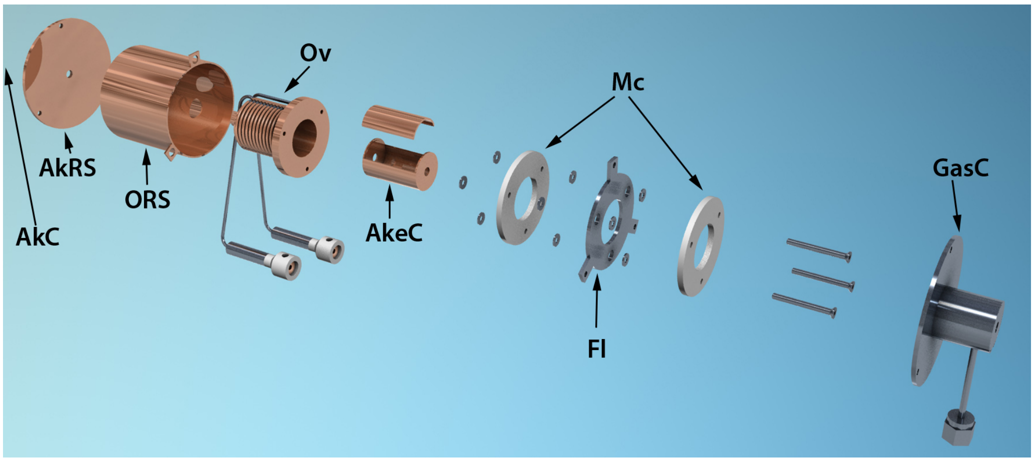

(b)

Figure 6.9.: Photo (a) and CAD drawing (b) of the alkaline earth metal pickup cell and its thermal shielding in an exploded view. Labels: AkC - alkali metal pickup dummy cell; AkRS - radiation shield for AkC; ORS - thermal shielding for the oven; Ov - oven; AkeC - alkaline earth metal pickup cell; Mc - MACOR discs; Fl - flange; GasC - gas pickup cell with suspension.

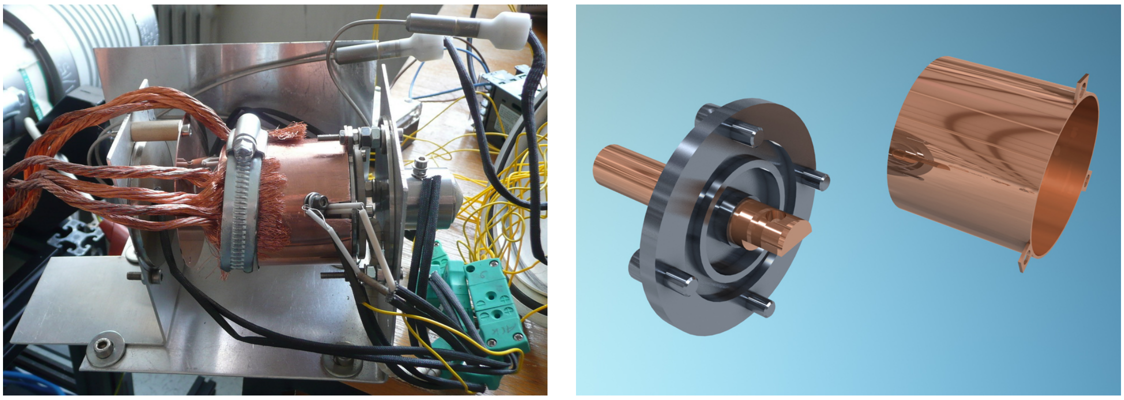

(a) (b)

Figure 6.10.: Photo (a) and CAD drawing (b) of the copper radiation shield, connected by a copper cable to dissipate the heat, as well as the feedthrough and the water-cooling of the copper cable (i.e., the radiation shield).

Influence of the shielding

Figures 6.11, 6.12 and 6.13 show the effects of the different shielding elements. The given temperature values have been obtained from the graph at a time of 180 min, the temperatures only change by 0.1 °C in 10 min at this point and can hence be considered as final temperatures. Some of the temperature recordings were not taken long enough, in that case an exponential fit (equation given in the graphs) was applied and the final temperature has been obtained from the fit. Again a general uncertainty of approximately ±3 °C applies to all values.
Figure 6.11 shows the temperature curve of the flange with and without the MACOR disc between the oven and the flange. As can be seen, the temperature without the disc is considerably higher, a final temperature of 185 °C is reached. With the MACOR disc installed, the final temperature is 116 °C.

Figure 6.12 shows the temperature curve of the oven shield with and without the copper cable attached to it. Note that the water-cooling has not been switched on during the record of this curve. The mass and the superb heat conductivity of the copper cable (around 300 $\mathrm{Wm^{-1}K^{-1}}$ depending strongly on the quality of the cable) alone were able to cool the radiation shield by 50 % since the final temperature of the shield with the copper cable attached is 94 °C, while without the cable it reaches up to 183 °C.

Figure 6.13 shows the temperature curve of the alkali metal pickup cell with and without the additional polished copper radiation shield mounted between the alkaline earth metal pickup cell and the former. Again the effect is considerable, without the radiation shield the alkali metal pickup cell reaches a temperature of 92 °C, while it only reaches 62 °C with the radiation shield installed. The flaw in the curve is due to a change of thermocouple thermometers which was necessary because of technical problems. However, the fit still resembles the curve and hence the final temperature.

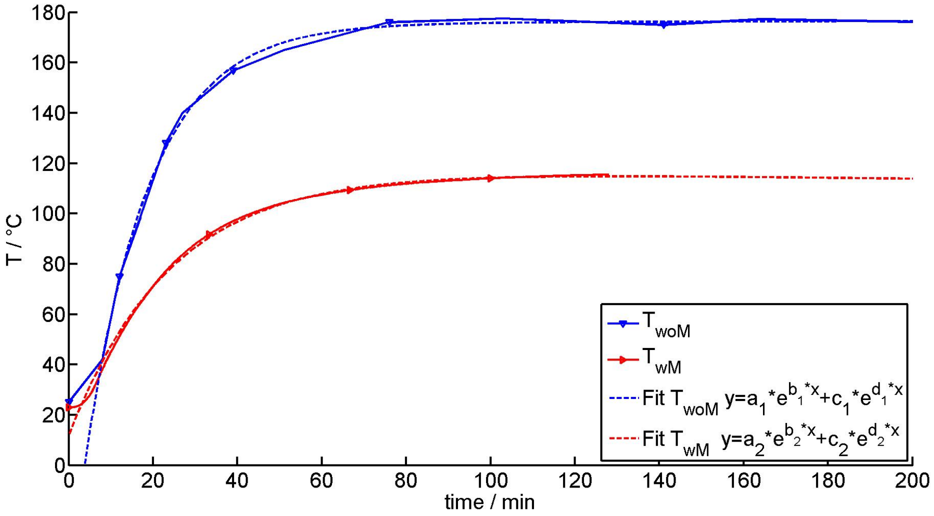

Figure 6.11.: Effects of the MACOR disc: temperature curve of the flange with and without the MACOR disc.

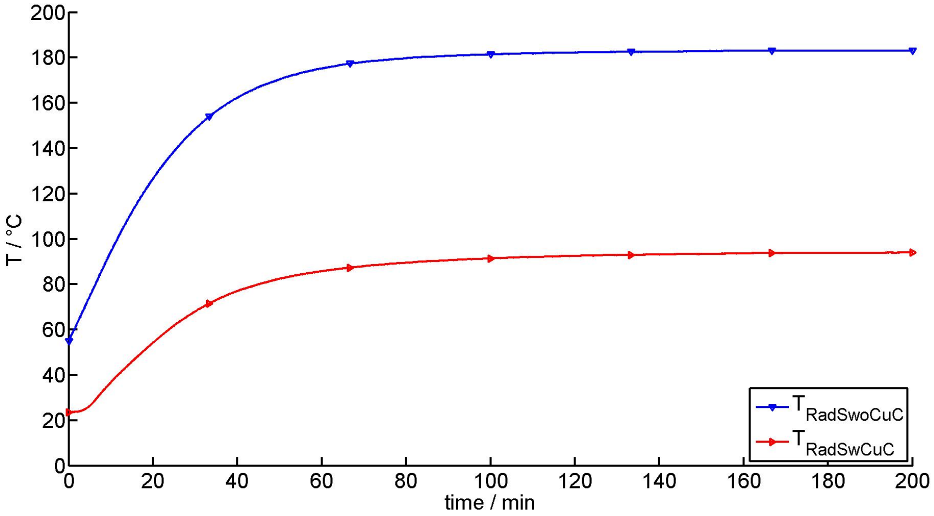

Figure 6.12.: Effects of the copper cable: temperature curve of the oven shield with and without the copper cable.

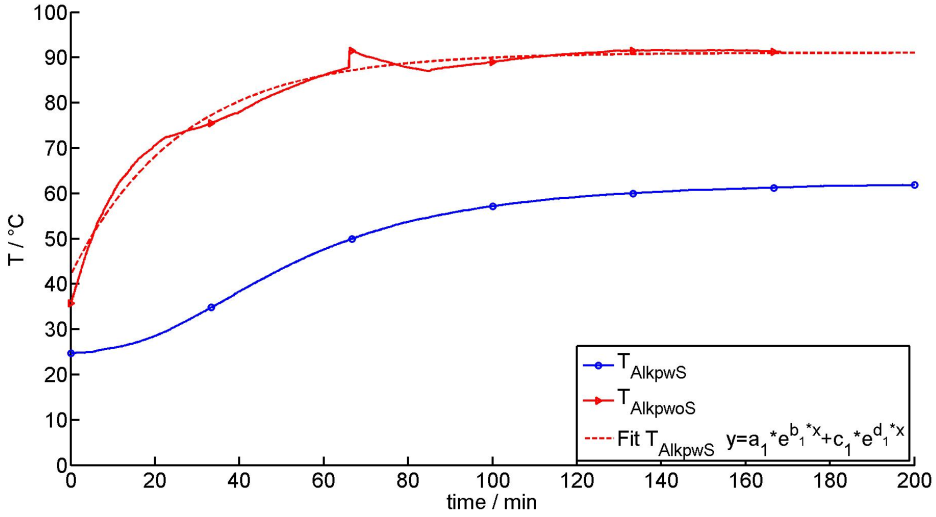

Figure 6.13.: Effects of the alkali shield: temperature curve of the alkali metal pickup cell with and without the additional radiation shield mounted in front of it.

6.6. Pickup Cell

The heat conductivity between the oven and a high quality steel cell is very inefficient, as can be seen in Figure 6.14. While the oven reached the predetermined temperature of 520 °C within minutes, the pickup cell itself needed nearly 90 min. Even though this response time was much better than with the old pickup cell, which needed about the same time to reach 100 °C, further improvement was attempted by making the pickup cell thinner and of copper. As can be seen in graph 6.14, this improved the response time considerably.

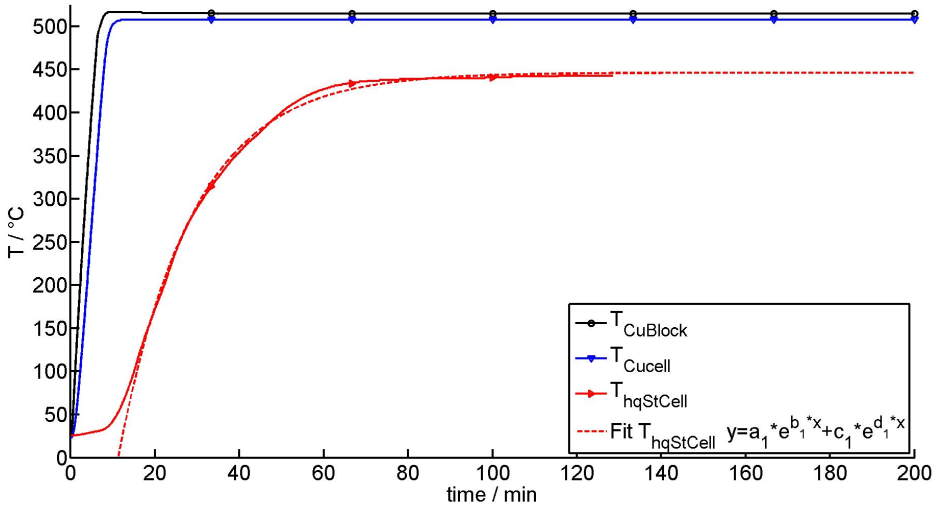

Figure 6.14.: Comparison of the temperature curve of a pickup cell made of high quality steel with 3 mm thick walls and a copper pickup cell with 1.5 mm thick walls. Both are given in respect to the temperature curve of the heated copper block. It can clearly be seen that the response time of the copper cell is considerably faster.

6.7. Results

Several test runs have been performed with this setup at various temperatures and durations. As a conclusion, it can be said that this setup easily reaches 520 °C in 12 min, using a heating power of 100 W and around 22 W to hold the temperature. Figure 6.15 shows all recorded temperatures of the final setup.

The final setup includes, as shown in an exploded view in Figure 6.9 (the given abbreviation refer to the labels in the Figure) :

1. The oven was connected to the flange via two MACOR (Mc) discs.
2. High quality steel washers were used as spacers between the oven (Ov) and the MACOR disc, as well as between the MACOR and the flange (Fl) on both sides of the flange.
3. A radiation shield (ORS) was put over the whole setup.
4. A 70 mm^2 copper cable was connected to this radiation shield to conduct the heat to a feedthrough (cf. Figure 6.10).
5. An additional radiation shield (AkRS) was installed to further shield the alkali metal pickup cell (AkC).

The parameters used for the heating in the final setup are: supply voltage $U = 21.3\,\mathrm{V}$ corresponding to 150 W maximum heating power; maximum heating output of the controller 75 % (limiting the maximum heating power to 100 W).

The temperature recordings given in Figure 6.15 and in Table 6.1 show the final temperatures for the single elements of the final setup.

Table 6.1.: Final temperatures of the single elements of the alkaline earth metal pickup setup, an overall uncertainty of ±3 °C applies:
T_{final}... final temperature of the respective element in degrees Celsius;
t... time needed to reach the final temperature in minutes;

Element	T_{final}	t
	°C	min
Copper block	514	10
Alkaline earth metal pickup cell	508	13
Flange	116	152
Radiation shield (can)	94	170
Gas pickup cell	73	152
Alkali Metal Pickup cell	62	143

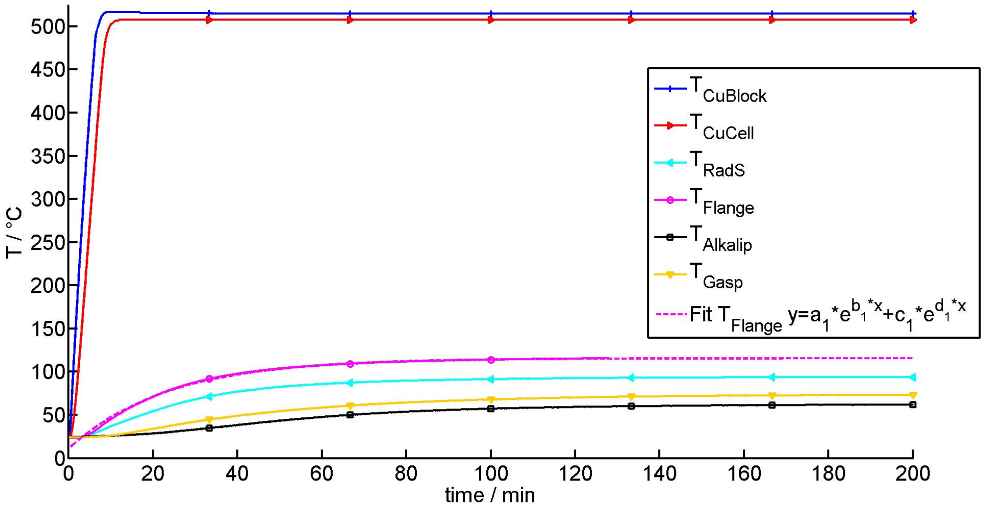

Figure 6.15.: Diagram of all recorded temperature values over time. The final temperatures of the single elements are given in Table 6.1.

6.8. Installation

Finally the tested and characterized Ake oven was installed into the experimental setup described in Chapter 3. Figure 6.16 shows a photo and a CAD drawing of the installed setup. The new configuration now holds three pickup cells: a gas pickup cell, an Ake metal pickup cell and a Ak pickup cell (listed along the beam direction).

The alkali shield was mounted on the M3 thread bars holding the alkali metal pickup, the rest of the setup was mounted on the M3 thread bars which were holding the gas pickup cell before. The gas pickup cell and its suspension were mounted in front of the Ake metal pickup cell (closer to the source chamber). Both feedthroughs for the copper cable and the electrical feedthrough (*VACOM, type: OBFMK*) were added to the front flange of the pickup chamber. Two thermocouples were connected to the oven in the final setup (one for the *Eurotherm* controller and one to be able to double-check the oven temperature).

As a power supply the same system is used as described in Section 6.4.3. The parameters of the *Eurotherm* controller unit have been set by autotune at a temperature of 520 °C (the parameters are temperature depended), to: Pb=14, ti=60, td=10, which correspond to the parameters of the three elements of the proportional-integrative-derivative (PID) controller (the extra parameters Lcb and Hcb have been set to ‘Auto’).

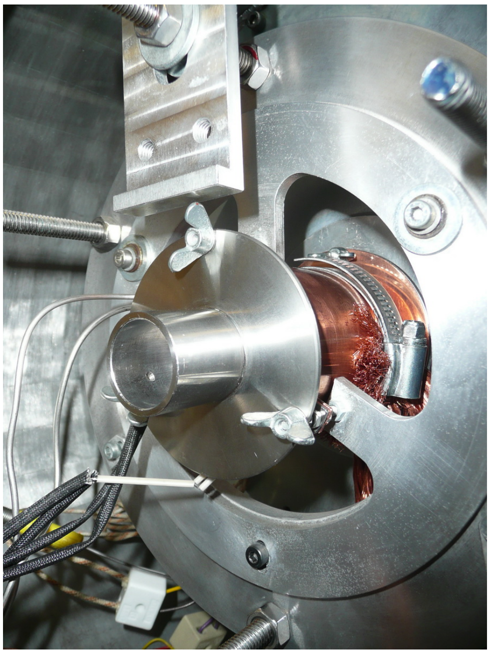

(a)

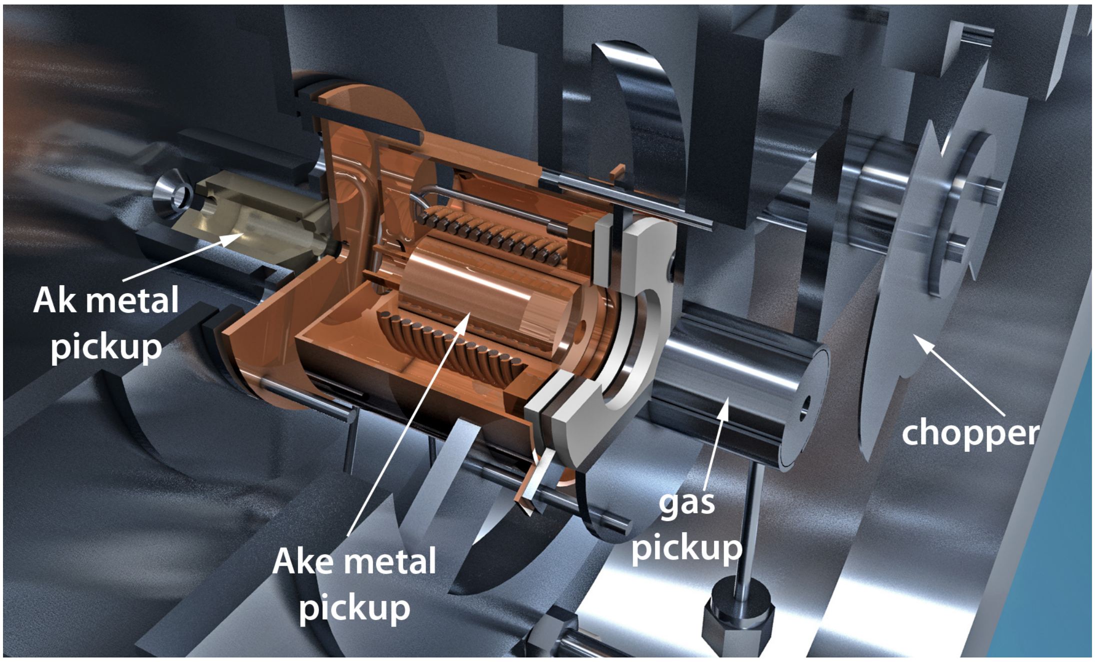

(b)

Figure 6.16.: Photo (a) and CAD drawing (b) of the pickup chamber with installed alkaline earth metal pickup cell including its thermal shielding, as well as the old alkali metal and gas pickup cell.

6.9. Summary: Heating within a Vacuum - Important Things to Know

The aim of this Section is to give the experimenter a quick overview over some different methods of heating within a vacuum and their pros and cons, sorted by their temperature range.

Temp. Range	**Recommended Method**		
<100 °C	**Heater cartridge**	**Pro**: simple system, easy to install, cheap, easy to control;	**Con**: don't work at high temperatures, error shows only slowly;
	Heater cartridges are in use to heat a pickup cell at another beam machine [34] and are tested to work well over a long period of time at a temperature of around 100 °C. They can simply be press-fitted in the object to heat and are inexpensive.		
100-250 °C	**Heater cartridge**		
	The first test runs in the course of this work, were performed with heater cartridges at a temperature of 250 °C, over the time tested, which was in the range of 5 hours. They performed well and no error occurred. However, the evaporation process causing the error at higher temperatures, as explained in the text above, might also occur at 250 °C but it may take a longer time for the error to take effect. Before heater cartridges are used at temperatures between 100-250 °C further long term tests have to be performed.		
250-520 °C	**Thermocoax**	**Pro**: simple system, relatively easy to install, easy to control;	**Con**: rather expensive;
	The thermocoax system described in the tests above has been thoroughly tested and run up to 7 hours without showing any sign of error or failure.		
520-800 °C	**Thermocoax**		
	The thermocoax is specified to bear up to 1000 °C. Test runs showed that it starts to glow dark red at a temperature around 530 °C - measured at the oven. According to glow temperatures of high quality steel this colour should be reached around 650 °C. This implies that the thermocoax is hotter than the copper block. Taking this difference into account, it should safely work up to a temperature of 800 °C - however, no tests have been run at this level.		
800 °C	**Electron bombardment**	**Pro**: works for very high temperatures	**Con**: expensive and elaborate
	Electron bombardment is a sophisticated technique in which electrons are accelerated via a high voltage onto the object to heat. This method requires a high technical and experimental effort. To reach temperatures above 800 °C, however, it is worthwhile. The method has been implemented into a He nanodroplet system and tested up to 1650 °C at another experimental setup [49].		

6.10. Problems and Solutions - Notes to the Experimenter

This Section will state some experimental difficulties which may seem obvious or trivial once one has experienced the problem, but those errors are the ones one spends a long time looking for when they occur for the first time. This Section can be seen as a 'note to the experimenter'.

6.10.1. The Intricate Problem of Measuring Temperature

In the course of this work it turned out that temperature indeed is a hard parameter to measure. There are several ways to measure temperature, mainly distinguished by being either via contact or via radiation. However, the setup was inside a vacuum and only parts of it could be seen through a window. Hence, non-contact temperature measurement devices did not really work here, since an infrared camera can not see through a glass window and other devices such as a pyrometer do not work properly at such low temperatures as 500 °C. Therefore only contact temperature sensors remained. Considering the temperature range to measure, the best and easiest way were thermocouples.

The Detail Box

Thermocouples:

Thermocouples work by using the so called 'Seebeck' or 'thermoelectric' effect. This effect describes the following phenomena: If we take two wires of different metal and connect them on one end to a hot surface, a potential difference (i.e., a voltage) forms on the other end of the wires. This is due to the difference in electrical conductivity of the metals. For an easy explanation let us consider a piece of common wire. As long as both ends are at the same temperature, the free electrons in the wire are more or less equally distributed throughout its length. If one end of the wire is heated, the electrons at that end get a higher (kinetic) energy. This results in an electron flow from the hot to the cold end of the wire, which in turn causes an electric field, counteracting the electron movement. An equilibrium between the electron flow and the electric field forms. However, this electric field cannot be measured directly, since the same effect will form in the measuring wires. But if we use two wires of a different metal with a different electrical conductivity, the effect is not equally strong in both metals. This means, if the two wires are connected with each other and pinned to a hot surface, at the other - cold - end of the wires, a small voltage forms, which depends on the temperature difference between the measurement point and the reference junction (cold end of the wires). Note: A thermocouple always measures a temperature *difference*, however most modern thermocouple thermometers display the absolute temperature. This can either be achieved by using a reference temperature point - so another thermocouple at a known temperature or, as it is usually done nowadays, this reference point is electronically simulated.

The material the thermocouples is connected to does not matter. If it is a metal, the same effect as between the two legs of the thermocouple appears between the thermocouple and the metal surface, however without affecting the potential difference between the two thermocouple legs.

So thermocouples are an easy and cheap way to measure temperature. However, there are some problems. The material the thermocouples are connected to does not matter as long as only one thermocouple is connected. A problem can appear if the temperature of a setup which is electrically conductive is measured at several points of the setup, such as is the case with the pickup cell. If two thermocouples are connected to one electrically conductive material and if only one thermometer (with several inputs) is used to read the temperature out an error will occur if the inputs of the thermometer are not electrically separated. Since this will create an electric loop from one thermocouple over the metal surface to the other thermocouple and back through the mass of the thermometer to the first thermocouple (cf. 6.17) this causes an error in the measured temperature. However, the error can be small (in the range of several 10s of °C), which makes it easy to overlook.

In the course of this experiments it turned out that the 4-channel thermocouple thermometer *Voltcraft K204 Datalogger* does not have this separation of inputs, hence it does measure an incorrect temperature when two or more thermocouples measuring the temperature of an electrically conductive setup are connected to it. This effect does not appear at room temperature, the difference between the actual temperature and the displayed one starts to diverge at about 100 °C. However, it reaches a difference of up to 70 °C at a temperatures in the range of 400 °C. The fact that the error is smaller at lower temperatures might be due to the ‘reference temperature point’ built into the ‘Datalogger’. Since only a temperature difference can be measured with thermocouples, most thermocouple thermometers hold a ‘reference temperature point’ - which is mostly simulated electronically.

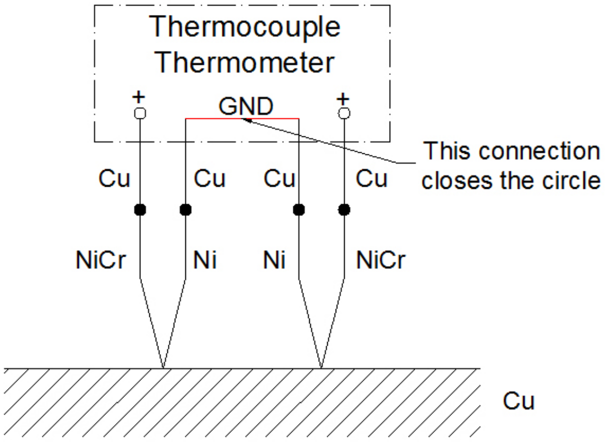

Figure 6.17.: Reading out two thermocouples connected to an electrically conductive surface with one thermometer can cause an error in the temperature measurement. If the inputs of the thermometer are not electrically separated, a stray electric current can flow from one thermocouple over the mass of the thermometer into the other thermocouple, which causes an error.

6.10.2. How to Correctly Measure Voltages

Another maybe useful note to experimenters: It turned out that the only way to correctly measure voltage at a setup including a regulating transformer, solid state relay and a controller is to use an oscilloscope, as shown in Figure 6.8. The problem is that the solid state relay, as explained above, regulates the voltage by periodically switching the power supply on and off. Since this happens in the range of several periods of the 50 Hz supply voltage, the resulting voltage does not have sine-shape anymore and hence cannot be measured by common voltmeters. True root mean square (TRMS) voltmeters are able to correctly measure the mean value of a non-sine-shaped voltage, however, in this case, they fail because the switching period of the SSR relay is too long for the TRMS voltmeter to integrate.

Using an oscilloscope the peak to peak voltage U_{pp} can be read from the display and the effective voltage U_{eff} can be calculated, using the relation: $U_{\mathrm{eff}} = U_{\mathrm{pp}}/(2\sqrt{2})$, this gives the voltage at 100 % power of the PID controller.
Note: when connecting an oscilloscope one has to carefully make sure that the ground connection of the oscilloscope is not connected to the phase of the supply voltage. This was done by supplying the oscilloscope (*HAMEG 203-7*) via an isolating transformer. Another possibility would be to supply the whole heating setup by an isolating transformer.

6.10.3. Unexpected Short-Circuit to Ground

In the initial setup, using heater cartridges to heat the pickup cell, a short-circuit to ground appeared several times. While a connection from the heater cartridge supply wires to the oven could be measured (see above for an explanation to this error), no connection to an earth potential could be measured, since the oven was electrically separated from the rest of the setup by the MACOR discs used as a thermal shielding. It turned out that the earth connection was achieved via the thermocouples. Several of those were connected to the oven and the rest of the setup, which was grounded. The thermocouples were connected to each other via the mass of the *Datalogger* reading out the temperature.
Note: Fault currents via thermocouples can lead to the destruction of the reading device or to wrong temperature results.

6.10.4. Limited Lifetime of Heater Cartridges

The short-circuit to ground had the following cause: The overheating of the resistance wire, due to bad thermal contact to the sheath within a vacuum (see Section 6.3, page 57), caused it to evaporate. The evaporating heating wire material coated some of the MgO, making it electrically conductive. Thus, after operating the cartridges some time at a high temperature (≈300 °C), an electrically conducting path from the heater wire to the steel shell formed. It could be measured as a resistance between a contact of the heater cartridge and the shell. The resistance became smaller the longer the cartridge was operated at high temperatures. Of course, operating a cartridge with an electrical connection to its shell only works if the shell does not have a connection to ground, otherwise an short-circuit to ground occurs. Depending on the quality of the connection, the system might even run properly after an short-circuit to ground occurs. After some time, however, another short-circuit to ground will occur and finally the heater cartridge will break completely.

CHAPTER 7

Results of Spectroscopy on Alkaline Earth Metal Doped Helium Nanodroplets

7.1. Preparation and Tests

The first successful test of the alkaline earth metal (Ake) pickup cell was performed with strontium (Sr). The pickup cell was filled with granular strontium, purchased from *Sigma Aldrich* [54]. Since strontium will build an oxide layer under air, the cell was filled in a glove-bag under argon atmosphere. The Sr granular were cut into pieces (pure Sr is soft enough to cut it with side cutting pliers). Since the granular had been delivered under oil it was washed in n-hexan to clean it from the oil film. The pieces were then simply dropped into the pickup cell and covered with n-hexan, to prevent oxidation (the n-hexan will evaporate in vacuum).

For the test of the Ake metal pickup the old high quality steel pickup cell was used to ensure that no reaction could occur between cell and dopant. However, the heating curve of this cell is much worse than that of the copper cell (cf. Section 6.6), hence further investigations will be made to find, if copper is an applicable material here, or if the heating characteristic of the high quality steel cell can be improved.

For the first detection of Sr doped He droplets the *Extrel C50-Q* quadrupole mass spectrometer (QMS) and a *Stanford Research SR 400* counter were used. The beam was established and adjusted at the usual parameters: nozzle temperature 14 K and He pressure: 60 bar. This corresponds to a droplet size of approximately 10^4 atoms. The beam was chopped, so that a difference signal, filtering out the background, could be acquired.

The Sr pickup oven was heated in steps up to 485 °C. At each step a mass spectrum was recorded from 1-60 amu at a multiplier voltage [1] (U_m) of -1.34 kV and from 60-100 amu at U_m = -1.42 kV[2]. Different multiplier voltages were used because the highest peak in the spectrum is usually the water peak at 18 amu and a high U_m at this position could lead to damage of the channeltron, where a high U_m and hence better gain at the position of the masses of the Sr isotopes (^{88}Sr 82.58 %, ^{86}Sr 9.86 %, ^{87}Sr 7 % and ^{84}Sr 0.56 %) was desired. During each heating period the

---

[1] The multiplier voltage is the voltage applied to the channeltron.

[2] *Note:* Before the mass spectrum could be recorded the considerable delay in heating time between oven and cell had to be taken into account (cf. Section 6.6).

masses 8, 19, 32 and 88 were recorded over time for the following reasons:

- Mass 8 corresponds to He_2, which is a droplet fragment and hence an indicator for the droplet beam.
- Mass 19 corresponds to H_3O which only occurs on the droplet as a result of fragmented water clusters. This provides a good possibility to observe the droplets as well as the water on the droplets.
- Mass 32 corresponds to O_2 and should stay constant over time.
- Mass 88 corresponds to Sr.

Please note that actually the ions (He_2^+, H_3O^8, O_2^2 and Sr^2) corresponding to these masses have been detected. To reach a vapour pressure of 10^{-4} mbar, for Sr a temperature around 400 °C is needed (cf. Figure 6.1). Considering the temperature gradient between the high quality steel cell and the oven of approximately 20 %, shown in Figure 6.14 the appropriate temperature of the oven was estimated to be around 450-500 °C. Figure 7.1 shows the recorded Sr mass during the heating process between 450 °C and 475 °C. It can be clearly seen that the Sr mass (88) rises steeply. To be able to distinguish a Sr atomic beam signal from a Sr doped droplet signal a chopper was used to chop the helium beam before the pickup cell. Hence, the signal achieved, when the chopper is closed corresponds to the 'background', so the atomic beam part of the Sr, while the signal when the chopper is open corresponds to both the atomic beam and the Sr atoms carried by the helium droplets. This means that the difference signal gives the relative number of Sr atoms on He droplets. Figure 7.1 clearly shows that only the chopper open signal and the difference signal significantly rise. This provides a good proof for Sr doped He nanodroplets.
The other recorded masses (8 and 19) slightly decreased. This is due to the pickup process of Sr.

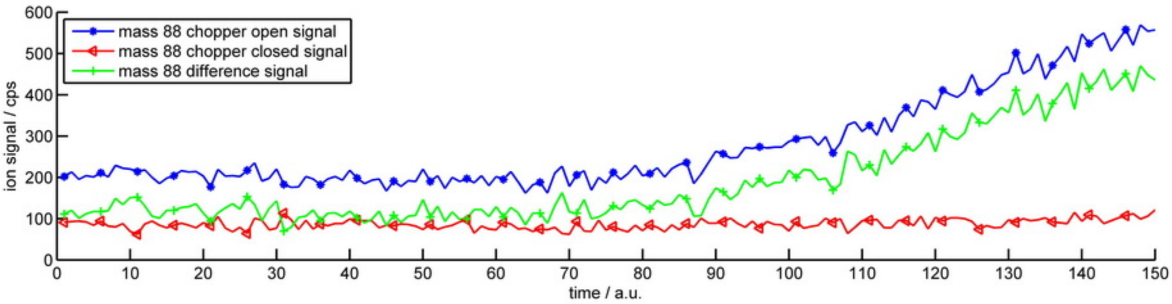

Figure 7.1.: Mass spectrum of Sr doped He droplets while heating the oven from 450 °C-475 °C. It was recorded with a QMS, the development of the Sr mass (88) has been plotted as a function of time. At an oven temperature of 475 °C a steep increase of the Sr signal can be seen, when the chopper is open (i.e., on the droplet).

In order to find the ideal temperature for a maximum monomer pickup, the oven temperature was further increased to 485 °C. However, the signal at a later cool down of the oven (cf. Figure 7.2) showed that the masses of Sr (88) and Sr_2 (176) rose again. The masses corresponding to the helium droplet (8 and 19) also slightly rose. This indicates that the temperature of 485 °C was actually too high, resulting in a too high pressure in the pickup cell. This in turn led to a higher destruction rate of the helium droplets (and hence to a lower signal). This is clearly shown by the difference signal of the Sr mass (green curve with '+' markers in Figure 7.2), which steeply increases. At the crest of the respective signals the temperature of the cell is ideal for monomer or dimer pickup. Hence, with the help of this cool down behaviour, the ideal oven temperature for Sr pickup was estimated to be around 450 °C[3].

The data in Figure 7.2 also confirms the theory of the pickup process, which obeys a Poisson distribution over temperature (see Section 2.3.5). The higher the temperature the higher the vapour pressure, the higher the probability that more than one Sr atom is picked up by one droplet. So the probability to detect dimers is higher at higher temperatures compared to detect monomer (single atom) pickup. This is why the peaks of the Sr and Sr_2 signals are shifted in Figure 7.2. If the temperature is further increased the signal decreases again since the vapour pressure of the Sr atoms in the pickup chamber is so high that a large part of the He droplets is destroyed. This is the reason why fewer dopants (Sr & Sr_2) are recorded at the beginning of the cool-down, cf. Figure 7.2
The data in Figure 7.2 also shows that there probability to find Sr_2 in the atomic beam is very low, since the chopper open signal and the difference signal of the Sr_2 mass are of nearly equal height (i.e., all the detected Sr dimers were on a He droplet).

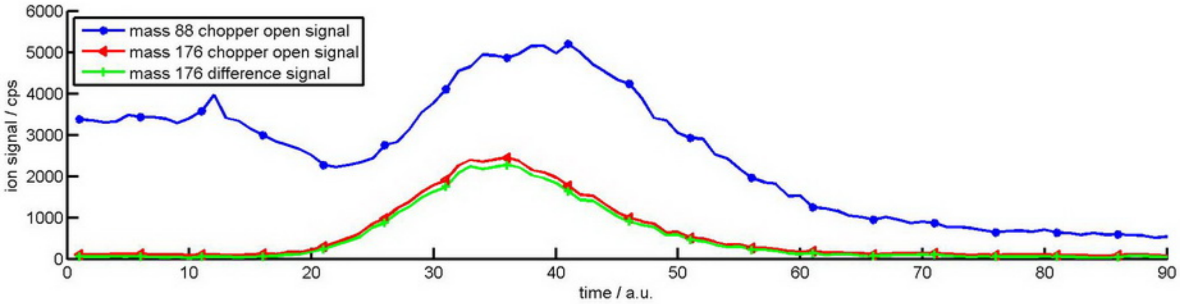

Figure 7.2.: Mass spectrum of Sr doped He droplets while the cool-down of the oven from 485 °C to approx. 300 °C. The development of the Sr (88) and Sr_2 (176) masses have been plotted as a function of time. The rise of the masses corresponding the Sr monomer and dimer masses (88 and 176) indicates that the oven temperature of 485 °C was too high.

7.2. Mass Spectrum, Recorded with a QMS

At the estimated ideal oven temperature for monomer pickup of 450 °C, the mass spectrum depicted in Figure 7.3 was recorded with a QMS. Masses from 80 amu to 360 amu were recorded, the multiplier voltage was set to U_m = -1.6 kV. Please note that only the difference signal has been plotted.
The upper half of Figure 7.3 shows the whole spectrum, while the lower half shows a close-up of the mass range 80-132 amu. As marked in the Figure, the peaks at the masses 84, 86, 87 and 88 correspond to the isotopes of Sr. The peak heights roughly correspond to the natural isotope distribution. The peaks occurring at multiples of 4 from the ^{88}Sr mass onward, correspond to

---

[3] Since the high quality steel pickup cell has a large temperature gradient to the oven and no thermocouple was connected to the cell itself, the actual cell temperature could only be estimated. Further investigations on the pickup cell material and temperature behaviour will solve this issue. However, when heating a material in a pickup cell one always has to take into account that it might form an oxide layer, which has to be removed before the material can be evaporated. If this is the case, the oven has to be slightly overheated in the beginning to remove the oxide layer. Once this layer has been removed it is important to lower the oven temperature again to reach the ideal vapour pressure.

Sr+He$_n$ (n= 1, 2, 3, ...) masses (i.e., to Sr connected to fragments of the He droplet), which proves that the helium droplets have been successfully doped with Sr atoms. The Sr-He compounds can be seen up to the Sr_2 (strontium dimer) mass at 176 amu. The lower signal between the masses 144-208 amu is most probably due to temperature fluctuations of the nozzle.

It is remarkable that beside strontium dimers, also strontium trimers (Sr_3 at 264 amu) and strontium tetramers (Sr_4 at 352 amu) can be seen in the spectrum. A comparison with the background signal shows that all these Sr compounds only exist on the droplet.

At the Sr_2 peak, one can see the single peaks, resulting from the possible combinations of the Sr isotopes. The highest peak should be at 176 amu, but it actually is at 176.8 amu, this is most probably due to a small inaccuracy in the scaling factor of the QMS[4]. The peaks starting from 174 amu and ending with 176 amu correspond to Sr^{86}+Sr^{88}, Sr_2^{88}, Sr^{87}+Sr^{88} and a negligible part of Sr^{86}+Sr^{87}.

The peak triplet in the mass range 104-106 amu corresponds to Sr+He_4, Sr+OH and Sr+H_2O. The latter complex forms when water molecules have been on the droplet. Upon the ionization of the QMS they desorb from the droplet and compounds are formed. The detection of Sr+OH is especially interesting here, because this compound has not been detected with alkali metal doped He droplets and might be a sign of a reaction of Sr and H_2O.

The peaks around 124 amu and around 190 amu also correspond to water or water fragments +Sr_2 and the peak at 280-284 amu corresponds to Sr_3+H_2O.

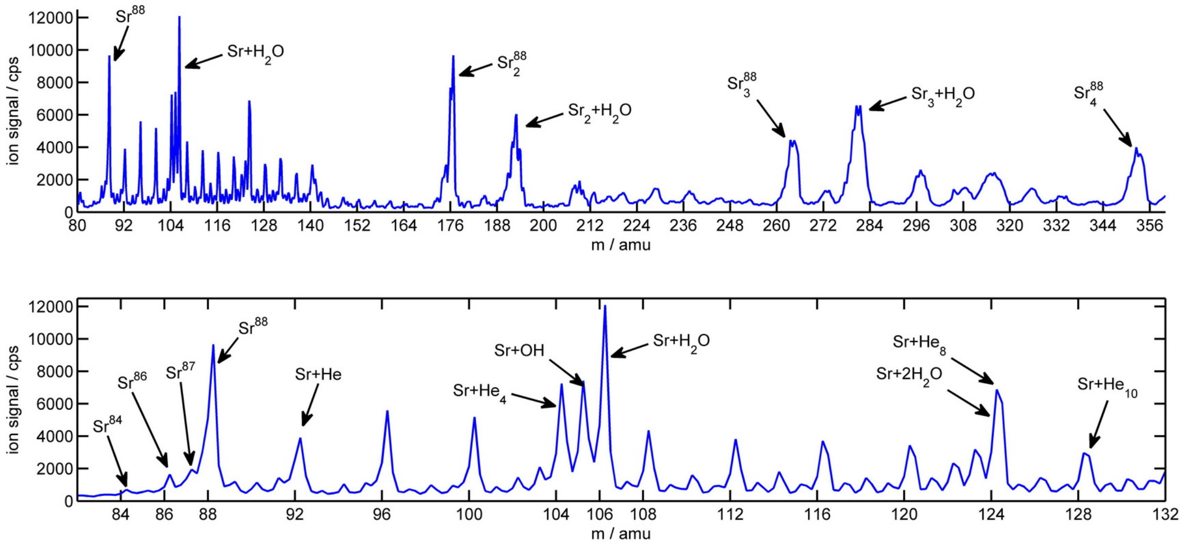

Figure 7.3.: Mass spectrum of Sr doped He droplets from 80-360 amu. The Sr peak at 88 u is clearly visible as are the Sr+He$_n$ compounds up to the Sr_2 peak at 176 amu. The Sr_3 and Sr_4 peaks at 264 amu and 352 amu respectively, are also well defined.

---

[4] The scaling factor translates the voltage output of the QMS into amu. This factor varies over a wide mass range such as 80-360 amu. On average it can be said that the masses are shifted by 0.25-0.5 amu to higher masses, which does not largely affect the interpretation of the spectrum. Since a big peak is expected at 176 amu and the peaks around this mass are conform with the expectations it is safe to assume that the shift of 0.8 amu is due to an inaccuracy of the QMS and the peak at 176.8 amu does corresponds to Sr_2.

7.3. R2PI Spectroscopy on Sr Doped He Droplets

After successfully doping He droplets with Sr, a resonant 2 photon ionization (R2PI) via the first excited energy level (5s5p $^1P_1$) of Sr doped He droplets was attempted. The technique and setting used, are the same as described in Section 4.2[5], however in this case the *Lambda Physik FL3002* pulsed dye laser (as a dye Coumarin 47 was used) was scanned over the 5s5p $^1P_1$ level of Sr and the *Coherent Indigo S* pulsed laser was used to ionize the Sr atoms. The atomic transition 5s5p $^1P_1 \leftarrow 5s^2\ ^1S_0$ of strontium is located at a wavelength of 460.86 nm (21698.5 cm^{-1}) and its ionization threshold is at 217.71 nm (45932.1 cm^{-1}).
The signal shown in Figure 7.4 shows the ion signal recorded with the TOF mass spectrometer while scanning the dye laser from 440-475 nm at a temperature of 15 K without focussing lenses. As a comparison the same spectrum recorded by Stienkemeier et al. [59] is given in Figure 7.5. Therein a shift of 84 cm^{-1} of the 5s5p $^1P_1 \leftarrow 5s^2\ ^1S_0$ line in respect to the atomic line and a broadening of 182 cm^{-1} (FWHM) is recorded. From our experiments we obtained a shift of (120 ± 20) cm^{-1} and a broadening of 395 ± 10 cm^{-1} (FWHM). The shift is well comparable with the findings of Stienkemeier et al., especially considering that the droplet size given in Ref [59] is ≈3000 atoms while we have been working with an average droplet size of ≈15000 atoms. The line broadening we obtained is much larger than recorded by Stienkemeier et al., it is even comparable to the broadening in bulk helium[6]. This is most probably due to the high power of our lasers and the fact that they saturated the transition, while this was not the case for the LIF experiments of Stienkemeier et al. The different droplet sizes between the experiments also affect the linewidth of the transition.

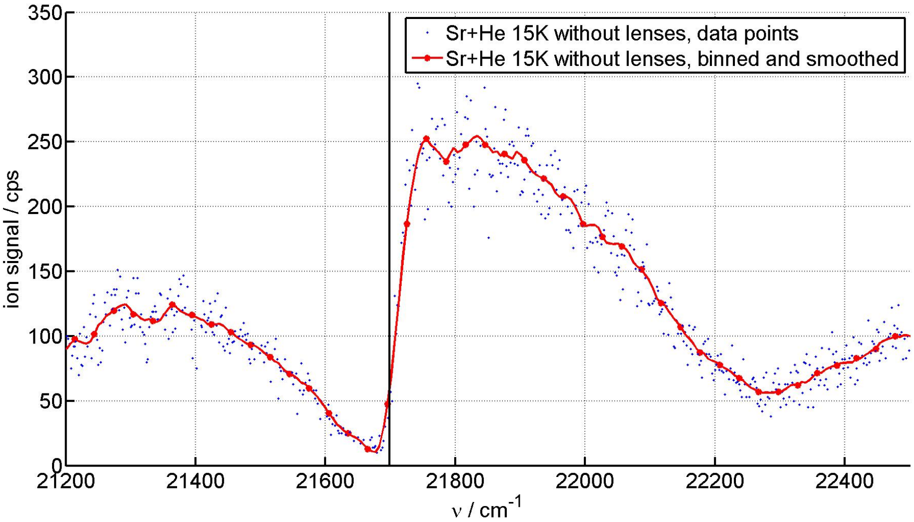

Figure 7.4.: R2PI excitation spectrum of the 5s5p $^1P_1 \leftarrow 5s^2\ ^1S_0$ transition of Sr doped He droplets. The vertical line denotes the bare atom transition. In order to improve the signal, data binning has been used. The solid line has been obtained with data smoothing. The nozzle temperature was 15 K, no focussing lenses were used.

---

[5] Some small modification to the setting have been made during the measurements in order to optimize the signal, most importantly some measurements have been performed with two focussing lenses (f=2 m and f=75 mm for the dye and the indigo laser respectively). The corresponding modification will be noted in the results below.

[6] The shift of the 5s5p $^1P_1 \leftarrow 5s^2\ ^1S_0$ transition for Sr in bulk helium is (252) cm^{-1} and the broadening is (265) cm^{-1} [59].

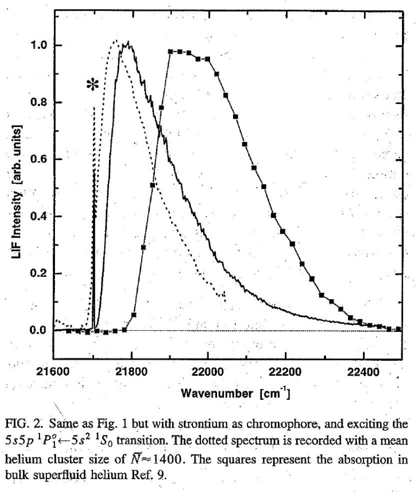

FIG. 2. Same as Fig. 1 but with strontium as chromophore, and exciting the $5s5p\ ^1P_1^o \leftarrow 5s^2\ ^1S_0$ transition. The dotted spectrum is recorded with a mean helium cluster size of $\bar{N} \approx 1400$. The squares represent the absorption in bulk superfluid helium Ref. 9.

Figure 7.5.: LIF spectrum of the 5s5p $^1P_1 \leftarrow 5s^2\ ^1S_0$ transition of Sr doped He droplets, recorded by Stienkemeier et al. [59], used for comparison.

In order to investigate the influence of the droplet size on the transition, the same transition as given above has been recorded at 14 K, 18 K and 20 K (with focussing lenses). Figure 7.6 shows the results. The intensities of the signals have been scaled to provide a better comparison of the signals. As can be seen, the shift only changes for the 14 K signal, however, this might also be due to the supercritical droplet conditions which start around this temperature.
However, the width of the signal clearly decreases for higher temperatures (i.e., for smaller droplets), leading to the assumption that larger droplets have a stronger influence on the dopant.

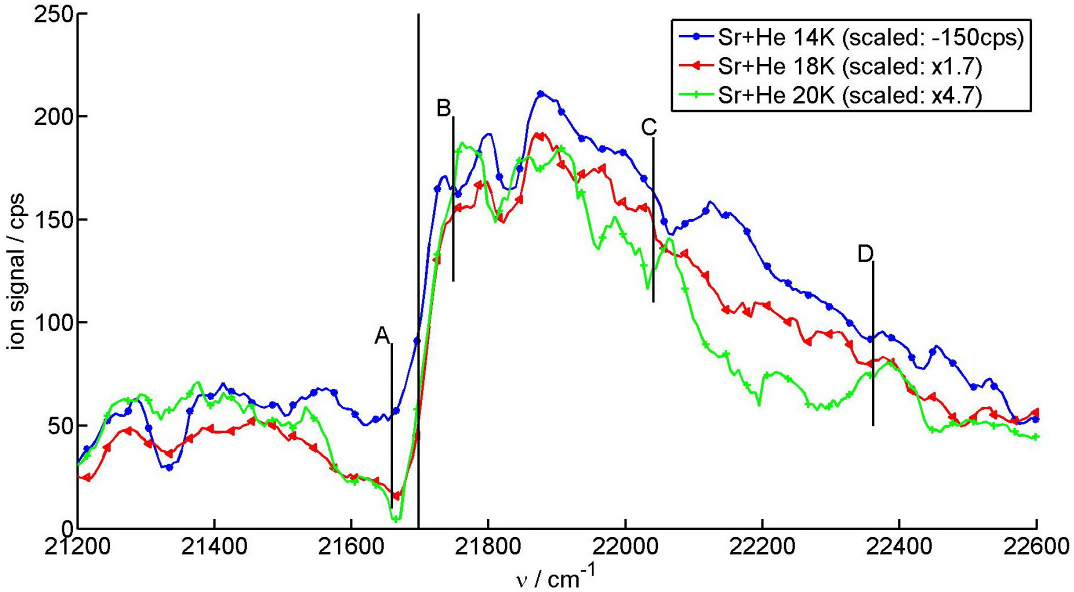

Figure 7.6.: R2PI excitation spectrum of the 5s5p $^1P_1 \leftarrow 5s^2\ ^1S_0$ transition of Sr doped He droplets, at different nozzle temperatures (i.e., droplet sizes). The vertical line denotes the bare atom transition. The line broadening decreases for smaller droplets. In order to improve the signal data binning and smoothing have been used. The nozzle temperatures are given in the legend, no focussing lenses were used.

At the points marked in Figure 7.6 mass scans with the TOF mass spectrometer have been recorded. They are depicted in Figure 7.7. It can bee seen that the Sr+He$_n$ signal is much stronger at the points B and C, so on the 5s5p $^1P_1 \leftarrow 5s^2\ ^1S_0$ transition. This shows that a fraction of the ionized Sr atoms desorbs from the droplet in form of Sr+He$_n$ exciplexes, upon excitation of the 5s5p $^1P_1 \leftarrow 5s^2\ ^1S_0$ transition. However, it also indicates an attractive interaction potential between the Sr atom and the He droplet which leads to the formation of exciplexes (similar to Rb D_2 line [63]). However, this data does not exclude the possibility that some Sr atoms do not desorb from the droplet upon excitation, or even immerse into the droplet, as has been detected by alkali atoms on He droplets. The fact that Stienkemeier et al. [59] did not find any depletion signal, could also indicate that the Sr atoms do stay on the droplet. The exciplexes found in our experiment might also origin from a Sr ion which drags along some He atoms from droplets. One possible way to investigate this, is to detect high masses (in the range of several thousand amu) with a TOF mass spectrometer, which will be done in future work.

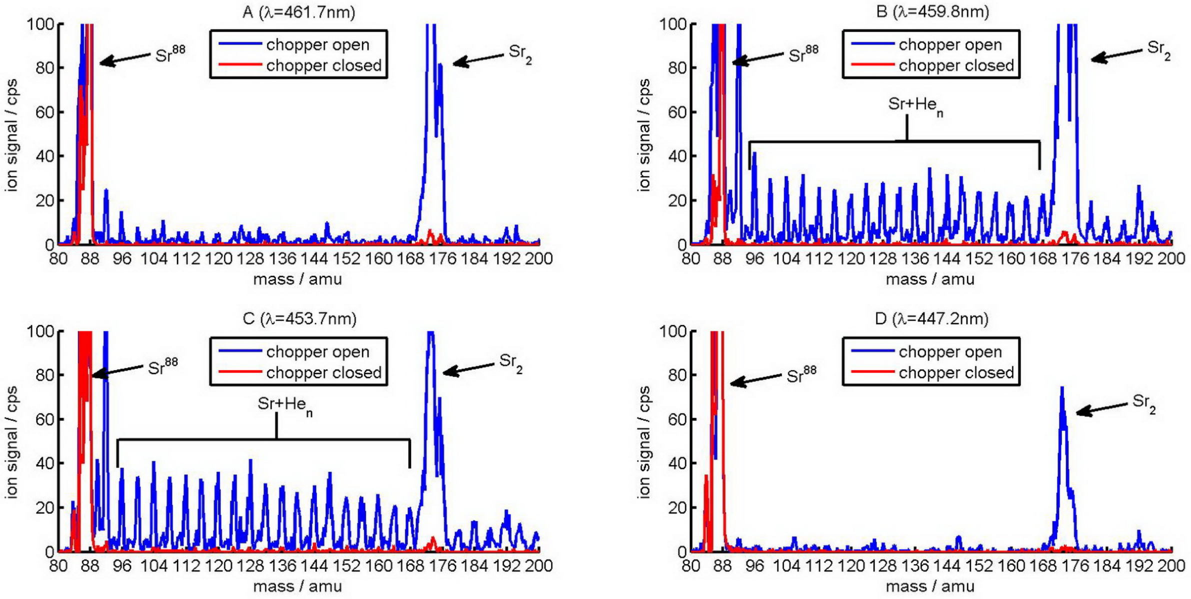

Figure 7.7.: Mass spectra at different points of the 5s5p $^1P_1 \leftarrow 5s^2\ ^1S_0$ transition of Sr doped He droplets, recorded with a TOF mass spectrometer. The position of the single plots in the spectrum is indicated in Figure 7.6.

7.3.1. Excitation of Strontium Dimers On He Droplets

In the course of these experiments, a Sr dimer transition on the He droplet was excited and investigated. Figure 7.8 shows a transition line of the dimer in comparison to the monomer transition. This is a very interesting result, since strontium dimers have not yet been investigated or detected on He droplets (to our knowledge), although some work has been done on bare strontium dimers, a list of publications can be found on the corresponding Section of the NIST homepage in Ref [28]. Recent works [16, 47] deal with the formation of Mg_2 and Ca_2 on He droplets. Some inconsistencies have been found and in one explanation it is stated that Mg atoms on He droplets do not actually form dimers, but are surrounded by a He layer, hence the spectrum between Mg and monomers should look similar. Interestingly the data from our experiment shows that the transition line of the dimer is broadened but not considerably shifted in comparison to the monomer line. The signals of the dimer transition at 15 K and 20 K are also not considerably different (although the recorded 20 K signal was very weak).However, the data are not sufficient to make definite predictions, but they show that Sr dimers can be detected and excited on He droplets with our experimental methods and hence that further investigations are advisable and may bring interesting and important results.

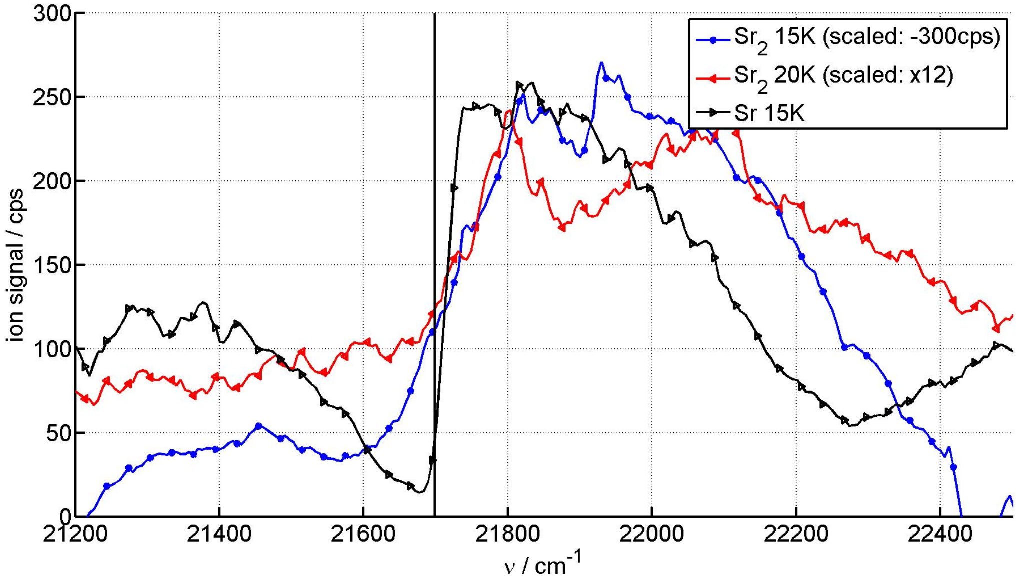

Figure 7.8.: R2PI excitation spectrum of Sr_2 on He droplets. As a comparison the 5s5p $^1P_1 \leftarrow 5s^2\ ^1S_0$ transition of Sr on the droplet at 15 K has been plotted. The vertical line denotes the bare atom transition. In order to improve the signal data binning and smoothing have been used. The corresponding nozzle temperatures are given in the legend. No focussing lenses were used.

CHAPTER 8

Summary and Conclusion

In the course of the work presented in this thesis, the method of REMPI-TOF (resonance enhanced multi photon time of flight spectroscopy) was successfully applied to Cs doped helium nanodroplets. With the help of this measurements, preliminary work done with LIF spectroscopy could be continued and a complete spectrum of Cs doped droplets was obtained. LIF as well as REMPI-TOF measurements used the well-defined and non-desorbing $6^2P_{1/2}$ state as an intermediate state, from which nS, nP and nD states were excited. Individual peaks could be resolved up to the 20S state. The pseudo diatomic model proved to be a good explanation for the states up to the $n = 10$ states, beyond that the Λ-substates start to merge. Around $n = 10$ the shift in energy of the on-droplet states compared to free atom Cs states changes from a blue shift to a red shift and converges for very high Rydberg states to the ionization limit. This indicates the beginning of a strong attraction of the Cs^+ core towards the interior of the droplet as has been observed in a so called snowball formation after the ionization [63].

As a second goal an oven and a pickup system for alkaline (Ake) earth metals was designed, constructed, and installed into the existing setup. A thermocoax wire was used to heat a copper oven up to 520 °C. The cylindric pickup cell has been constructed in order to make it easy to refill and insert into the oven. The cell can be heated up to temperatures necessary to reach the correct vapour pressure for the pickup of Ake metals within very short times (above 500 °C in approx. 15 min). Furthermore, the oven has been shielded so that adjacent elements, especially the alkali pickup cell, are not heated up above 80 °C.

The final objective of this work was to test the Ake oven and pickup cell and to obtain first results for Ake doped helium nanodroplets. This was successfully done with strontium. A QMS spectrum was recorded proving that the doping process worked well, showing Sr+He fragments up to the Sr_2 mass, as well as Sr trimers and tetramers on the droplet.
An excitation spectrum of the $5s5p\ ^1P_1 \leftarrow 5s^2\ ^1S_0$ transition of Sr on He droplets was recorded using R2PI-TOF spectroscopy The results are in accordance with earlier experiments by Stienkemeier et al. [59]. Our experiment showed a line shift of $120 \pm 20\,\mathrm{cm}^{-1}$ and a line broadening of $395 \pm 10\,\mathrm{cm}^{-1}$ (FWHM).
In the course of this experiment the droplet-size dependence of the line broadening was investigated: For smaller droplets the width of the line decreases, which indicates a smaller interaction between the Sr atoms and the He droplet at smaller droplet sizes.

Finally a dimer transition was excited and investigated. It is interesting to dedicate further work in this topic, since only recently questions about dimer formation on Mg doped He droplets [47] appeared.

The promising results of these last experiments, as well as the reliable heating power of the oven up to high temperatures allow for further investigation of the, not yet well known, Ake doped He droplets on the one hand and for the pickup and investigation of other possible dopants on the other hand.

APPENDIX A

Additional Information on Lasers

A.1. Laser gratings

As mentioned in Section 3.4.2, the grating of the Lambda Physik dye laser is aligned in a 'Littrow configuration'. This Section will describe this configuration and its working principle in close detail. At first, some basics about diffraction gratings will be reviewed. Most of the information in this Section has been taken from [11].

The intensity distribution of a wave diffracted at a transmission grating is caused by two effects:

- The interference of the single waves of the slits (cf. Figure A.1 a).
- The diffraction distribution at each single slit (cf. Figure A.1 b). The width of the distribution depends on the ratio of slit-width to wavelength (λ/b).

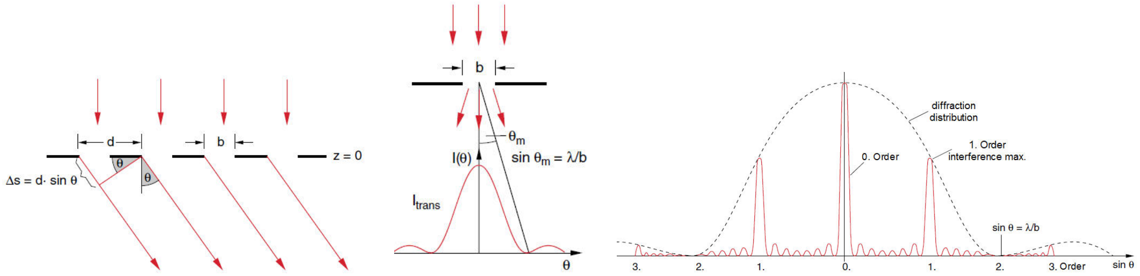

(a) (b) (c)

Figure A.1.: a) Diffraction grating with slit width b and spacing d. The incident beam travels parallel to the grating normal b) Diffraction distribution at a single slit of a grating. c) Combination of the effects of a) and b). Example of an intensity distribution at a grating with 8 slits and a ratio of $d/b = 2$ (all mod. from [11]).

Actually both effects are due to the Huygen's principle - every point reached by a light wave becomes the source of a new elementary (spherical) wave. So with one slit (cf. A.1 b), one can assume a lot of points within this one slit, each is reached by the incident light and each is the source of a new elementary wave. The highest intensity is reached for those waves travelling in a straight line from the slit to the detector plate, since there is no path difference between them. This middle peak is called 0^{th} order peak and is does not depend on the wavelength of the light. This is different for a wave-front travelling at an angle Θ from the surface normal of the slit. The single waves of the wavefront hit the detection plate with a path difference of

$$\Delta s_1 = m\lambda = b \sin\Theta. \tag{A.1}$$

The waves interfere and finally give the distribution indicated in Figure A.1 b), where the width of the distribution is

$$\sin\Theta_m = \frac{\lambda}{b} \tag{A.2}$$

for each order m.

For several slits one can see each slit as one single source of elementary waves and again an interference pattern is created by the interference of these waves (cf. Figure A.1 a). Let us again have a look at the waves diffracted by an angle Θ from the surface normal of the grating. The interference of the elementary waves in this direction forms a plane wave travelling along the arrows. We can imagine that one elementary wave starts from each slit. To see how they interfere in the indicated diffracted direction (Θ from the grating normal), we have to view the path differences for the single waves to reach the plane wave. The left wave has to travel $d \sin\Theta$ farther to reach the plane than the wave to its right. So the path difference between the waves is $\Delta s_1 = d \sin\Theta$. At the same time, constructive interference is only achieved for multiple integers of the wavelength $m\lambda$ where m is called the order of diffraction. This nicely leads us to:

$$\Delta s_1 = m\lambda = d \sin\Theta, \tag{A.3}$$

where d is the slit spacing. The size of the single maxima depends on the diffraction distribution of each slit (indicated in Figure A.1b).

We achieve the actual interference pattern of a grating if we add the two diffraction effects. Figure A.1 c) shows an example of the intensity distribution of a grating with eight slits and a slit spacing to slit width ratio of $d/b = 2$. The single maxima within the diffraction distribution are called maxima of m^{th} order. The highest order is given by (due to equation A.3): $\sin\Theta \leq 0 \rightarrow m_{max} = d/\lambda$ that means by the ratio of slit spacing to wavelength.

This principle also applies to reflective gratings. If we shine light of a certain wavelength λ perpendicularly on a grating, we get the same diffraction distribution as shown in Figure A.1 c). Figure A.2 a) shows a sketch of this, with the 0^{th} and 1^{st} order reflection and the path difference Δs_1 indicated.

If the incident beam is not travelling parallel to the grating normal, but at an angle of incidence α, the situation changes (cf. Figure A.2 b). Now a second path difference Δs_2 occurs, since the incident beams do not reach the grating surface at the same time. This changes equation A.3 to:

$$\Delta s = m\lambda = d(\sin\Theta + \sin\alpha). \tag{A.4}$$

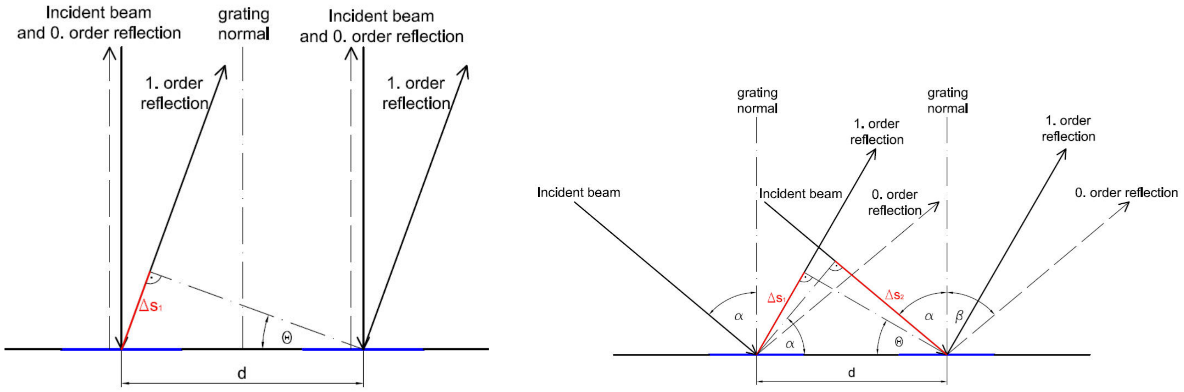

(a)

(b)

Figure A.2.: Sketches of reflective gratings. a) The incident beam is parallel to the grating normal, the path difference is zero for the 0^{th} order ($\Delta s = 0$), for higher orders it is calculated by equation A.3. b) The angle of incidence is α, for the 0^{th} order $\Delta s = 0$ again. For higher order equation A.5 applies.

For the 0^{th} order the path differences cancel out $\Delta s_2 - \Delta s_1 = 0$, so we can not use the 0^{th} order if we want to use the grating as a wavelength selective device, because it is not a function of the angle of incidence α. We have to use the 1^{st} or higher orders, but their intensity is considerably weaker, as can be seen in the distribution in Figure A.1 c). This can be corrected by using a ‘blazed grating’.

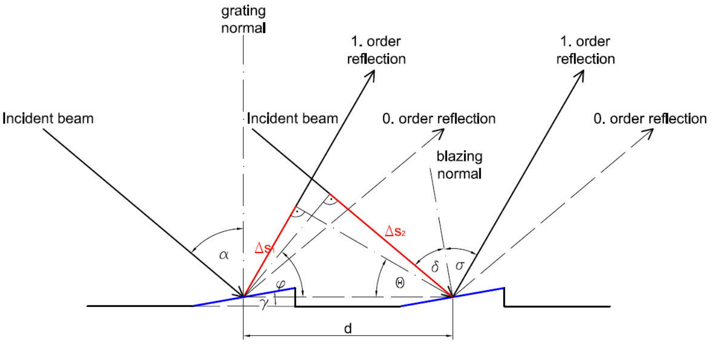

Figure A.3.: Sketch of a blazed grating. The angle of incidence is the same as in b, the path differences do not change compared to a normal reflective grating, as long as the angle of incidence α and the wavelength of the light λ remain the same.

In order to maximize the intensity for the 1^{st} order reflection, we slightly tilt the reflective parts of the grating, constructing a blazed grating with a certain blaze angle γ (indicated in Figure A.3).

We shine light on the grating of the same wavelength λ and the same angle α as above. We still get the same reflections concerning the directions, since the reflection angles are not a function of γ (i.e., equation A.4 is still valid). So we still get the same position for the interference peaks as indicated in Figure A.1 c). However, the position of the diffraction distribution changes. The strongest peak will always result for waves reflected by the reflection condition (angle of incidence is equal to angle of reflection ($\alpha = \beta$)). If the blaze angle γ is chosen so that the direct reflection is going into the direction of the 1^{st} order (indicated in Figure A.3 c), the highest intensity will be reflected in the direction of the 1^{st} order. In this case, the angle of incidence to the blaze normal is equal to the angle of reflection to the blaze normal $\delta = \sigma$. The reflection angle of the m^{th} order can easily be calculated from equation A.4. In this way, a blazed grating can be optimized for the reflection of a certain wavelength by correctly choosing the blazing angle γ.

A special alignment of a blazed grating is the ‘Littrow configuration’ (cf. Figure A.4). In this case the blaze angle is chosen equal to the angle of incidence $\gamma = \alpha$, which means that all the reflective areas are aligned perpendicular to the beam of incidence and hence the m^{th} order reflection is reflected back into the direction of incidence, if:

$$\Delta s = m\lambda = 2d \sin\alpha \tag{A.5}$$

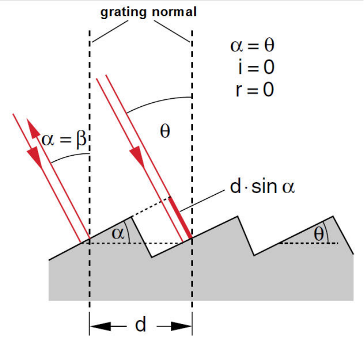

Figure A.4.: Sketch of a Littrow grating. This is a special alignment of a blazed grating, where the blaze angle is equal to the angle of incidence ($\alpha = \gamma$), which results in the m^{th} order reflection being reflected back into the direction of the incident beam, if the condition A.5 is fulfilled (from [11]).

The Lambda Physik dye laser uses a blazed grating aligned in the ‘Littrow-configuration’, within the resonator. The grating can be tilted, changing the angle of incidence, hence the wavelength can be scanned. The 3^{rd} to 8^{th} orders are used and the grating can be tilted from 42.5° to 72.5°.

A.2. Operating the Radiant Dyes RD-EXC-200 Laser

A.2.1. Operation

This Section can be seen as a step by step manual of how to operate the *Radiant Dyes RD-EXC-200* excimer laser. However it only describes the laser as it is used in our laboratory, i.e. controlled by a LabView program.

Switching the Laser on and off

First turn the laser on, by turning the main power switch at the bottom of the laser, next turn the key and at last push the green button. Then start the LabView program of the laser and let it warm up. Do not forget to turn on the cooling water (recommended pressure: 0.7 bar). In order to switch the laser off, proceed the other way around - close the program, switch of the green button, turn the key and finally the main switch. Don't forget to turn off the water.

Operate the Laser by the LabView Control Panel (cf. Figure A.5)

Beside the operation by the LabView program, the laser can be operated by a provided keyboard, or by a terminal program. However both options are less convenient, more elaborate and have not been used in course of this work, hence only the operation by the LabView control panel will be explained here. Figure A.5 shows a screenshot of the LabView control panel.

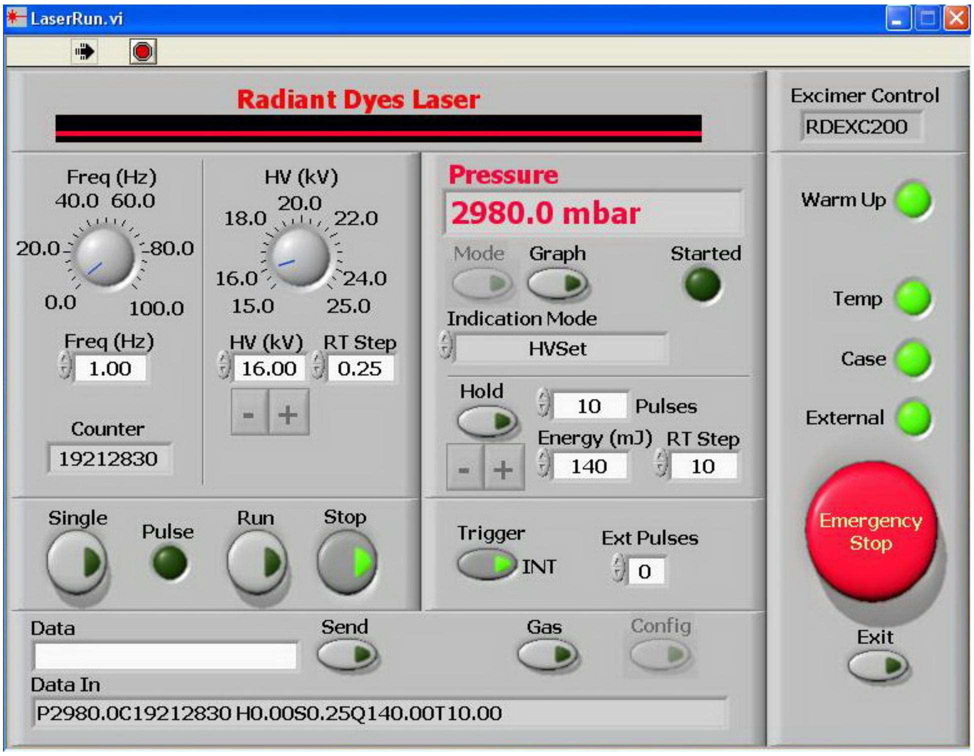

Excimer Control: RDEXC200
Pressure: 2980.0 mbar
Freq (Hz): 1.00
HV (kV): 16.00
RT Step: 0.25
Counter: 19212830
Indication Mode: HVSet
Pulses: 10
Energy (mJ): 140
RT Step: 10
Trigger: INT
Ext Pulses: 0
Data:
Data In: P2980.0C19212830 H0.00S0.25Q140.00T10.00

Figure A.5.: Screenshot of the LabView control panel of the *Radiant Dyes RD-EXC-200* excimer laser

Most of the options are self-explanatory, however some important notes shall be mentioned here:

- In the 'Freq. (Hz)' Section, obviously the frequency of the laser pulses can be adjusted (range: 1-100 Hz).

- A little to the right the high voltage control is situated ‘HV. (kV)’, a value between 16-25 kV is suggested. The value can be increased (decreased) while the laser is running by clicking on the plus (minus) button. The voltage in- or decreases by the step size given in the ‘RT’ field.
- In the text field at the left bottom of the control panel inquiries for laser parameters can be sent to the laser, e.g. ‘p?’ sends a request for the pressure of the discharge chamber to the laser. After the ‘Send’ button has been pressed, the actual pressure is displayed in the ‘Data In’ field. The commands which can be sent to the laser are given in the manual [48].
- With the ‘Indication Mode’ selection, one can choose which parameter of the laser is displayed in the red display above, as well as in the graph (which can be switched on and off by the corresponding button ‘Graph’[1]). Clicking button ‘Mode’ changes the display of the field above, the following parameters will be shown: Energy Averaged, EnAv+HV Meas (energy averaged and measured high voltage, the value of the latter is sometimes not correct), HV set (set value of high voltage), HV Meas (measured high voltage, again sometimes not correct), Counter, Pressure, Energy set and Energy Measured.
- In the field ‘Energy (mJ)’ the desired energy of the laser pulses can be entered. Like the voltage the energy can be in- or decreased by clicking on the plus or minus button. Again the step size is chosen by the field ‘RT’. It is suggested to control the energy by the voltage - using a voltage of e.g. 16 kV will automatically produce a certain energy value.
- If a certain number is entered in the field ‘Pulses’ and the button ‘Hold’ is activated, the laser should hold the energy selected below over an average of the pulses given in the field.
- The ‘Gas’ button opens a second panel, which can be used to administer the gas - see Section A.2.3 for more information.

A.2.2. Changing the Trigger from Intern to Extern

The Excimer laser uses two trigger impulses, one to trigger the charge of the capacitors and one to trigger their discharge. Both impulses can be sent by an internal trigger or an external. This is set in the ‘Trigger’ Section: Pressing the button ‘Trigger’ switches the trigger from extern to intern. When it is set to extern the number of trigger pulses can be given. 1 means that only the charge impulse comes from an extern trigger. 2 means the discharge, as well as the charge impulse come from an external source. In the course of the experiments described in Section 4.2, it was necessary to send both trigger impulses from an extern source. The first extern trigger is connected to the *RD-EXC-200* via an optical fibers. At the back of the setup there are several optical fiber plugs, one of which is labelled ‘trigger’, this is the connection for the extern charge trigger. To connect an optical fiber to also trigger the discharge trigger externally is a little more difficult. The housing of the laser has to be opened - act with extreme care, high voltage up to 30 kV is produced in the laser and stored in capacitors. At the top left of the inner shielding the housing of the trigger is mounted. At its back end an optical fiber is connected and another one hangs loosely close by. To change the trigger from intern to extern, simply exchange those two optical fiber - unscrew the holding screw of the connected optical fiber, pull it out carefully and connect the other one.

Finally do not forget to adjust the trigger mode accordingly in the control panel - ‘Trigger’ should be ‘EXT’ and the ‘Ext Pulses’ should be set to ‘2’.

---

[1] If no signal can be seen at the graph, check the y scaling.

A.2.3. Refilling the Gas

This Section provides a step-by-step description of the procedure to refill the gas mixture in the *RD-EXC-200* laser, since the description given in the manual is not very detailed. Please note that this description is only valid for refilling the laser with a gas ‘premix’.

Before starting the whole process:

- ACT WITH CARE! The laser gas is toxic!
- Open the gas control panel of the LabView control of the excimer laser, by clicking on the ‘Gas’ button and choose the ‘Manual Fill’ in the ‘Fill Mode’, as shown in Figure A.6.
- Hang the exhaust pipe of the pump out the window, for security reasons. The gas used to fill the laser is toxic, however the pump does have a corresponding filter. Hanging the pipe out the window further minimizes the risk of intoxication.

A. Flushing the pipes:
The following process is called ‘flushing’, as it flushes all the pipes with helium. In principle, all pipes between the laser and the gas bottles and then the pipes inside the laser have to be flushed wit inert helium gas. The process has to be repeated several times during the refilling the laser, hence it will be only described once and only referenced to in the text below.
Proceed as follows:

1. Start the vacuum pump (P in Fig. A.7) by clicking on start button on the right bottom of the gas control panel.
2. Make sure that the gas mixture bottles (HCl) and V5 are closed! All valves inside the laser (V1-V4) are also closed .
3. Open the helium bottle (He), valves V6, V8, V9 and the vacuum valve. Check the He pressure at MTU2[2], regulate it to ≈3 bar.
4. Open V7 (this pumps out all the pipes outside the laser). Check the pressure at MTU1, regulate it to ≈3 bar, in case open the MTU2 regulating valve wider.
5. Close V7.
6. Open the vacuum valve via the control panel (this pumps out all the pipes inside the laser).
7. Close the vacuum valve.
8. Open V5 (pumps helium in the pipes outside the laser).
9. Open valve 4 (inert gas) via the control panel (pumps helium in the pipes inside the laser).
10. Close V4 and V5.
11. Repeat steps 4-10.

B. Exhaust the old gas:
Before refilling the laser, the old gas has to be exhausted from the reservoir:

---

[2] The maintenance units (MTU) contain two manometers giving the pressure before and after the regulating valve in the middle. MTU1 regulates the HCl gas flow, MTU2 the He flow.

1. Flush the gas pipes three times as described in A. above, ending the last cycle with step 10 (all pipes filled with He).
2. Make sure that V4, V6 and V7 are closed.
3. Open the vacuum valve and then the head valve via the control panel, the laser head is now being pumped out, wait until the pressure reaches 10 mbar, then close the head valve and then the vacuum valve.

C. Refill the laser:

1. Open V7 (this pumps out all the pipes outside the laser).
2. Make sure that V6 and V7 and the vacuum valve are closed. (All others may be closed as well, except valves 8 and 9, they need to be open).
3. Open the gas mixture bottle (HCl) - carefully make sure that the pressure at MTU2 is ≈3 bar.
4. Open valve 1 and the head valve via the control panel, refill the laser head up to a pressure of 3070 mbar.
5. Close the head valve, and V1 .
6. Close the gas mixture bottle.
7. Flush the pipes three times as described in A.
8. In the end fill all pipes with helium close all valves, turn back the regulating valve of MTU2 and turn off the pump (P).

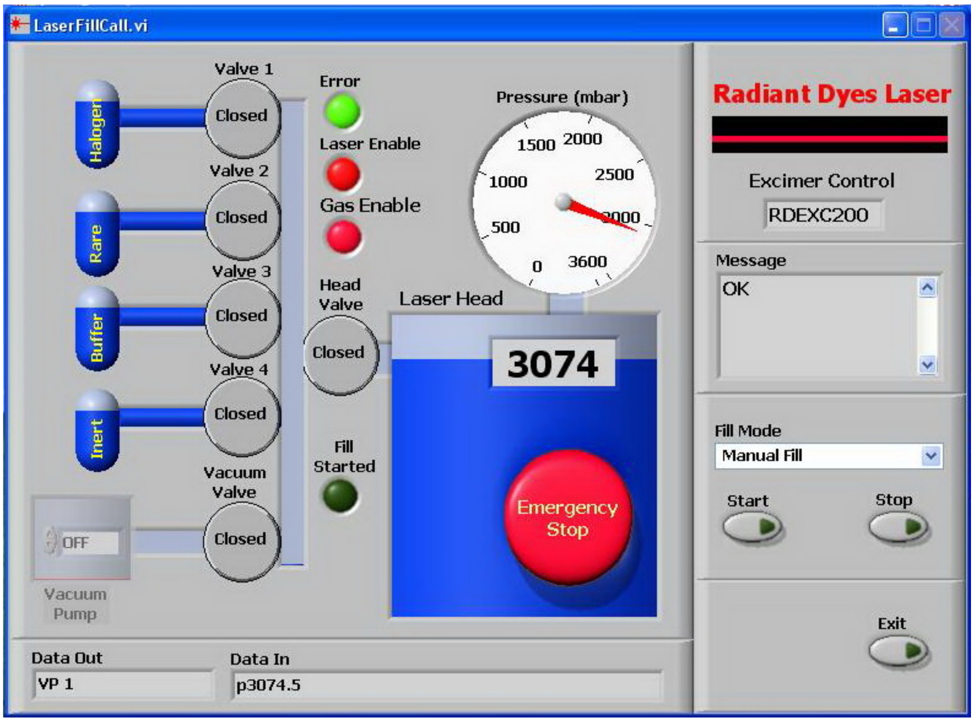

3074

Excimer Control: RDEXC200

Message: OK

Fill Mode: Manual Fill

Data Out: VP 1

Data In: p3074.5

Figure A.6.: Screenshot of the Gas control panel of the LabView control of the *Radiant Dyes RD-EXC-200* excimer laser.

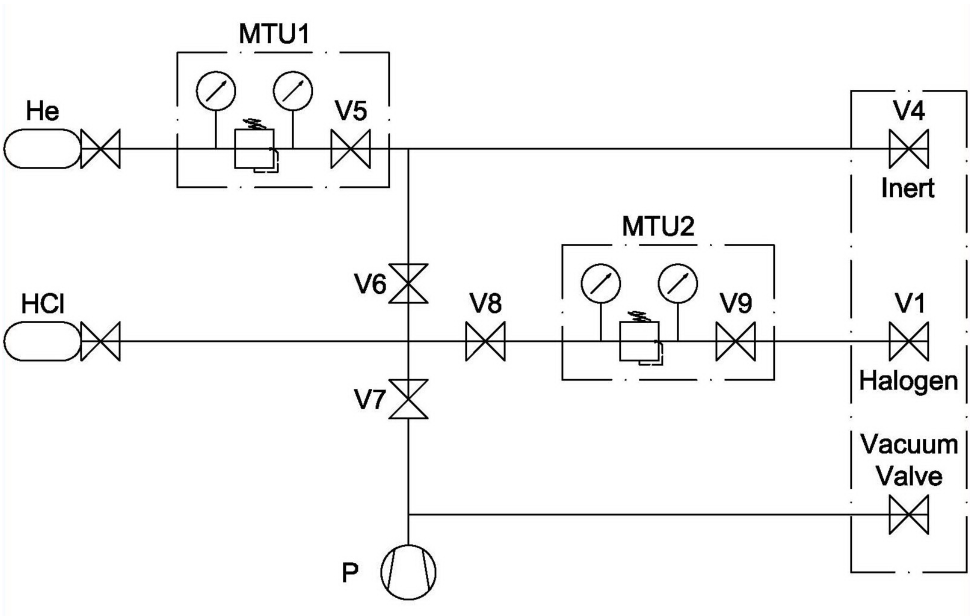

Figure A.7.: Diagram of the valve system of the *RD-EXC-200* laser, see below for the description of the symbols.

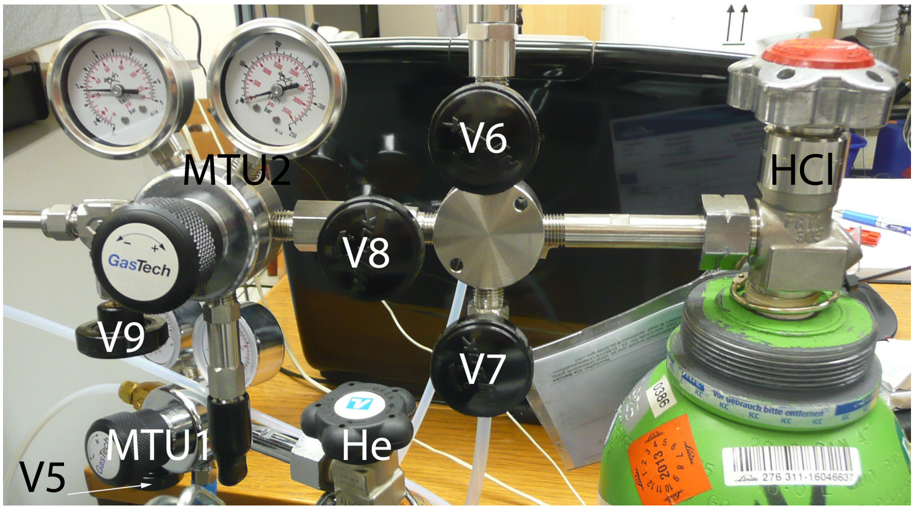

Figure A.8.: Photo of the valve system of the *RD-EXC-200* laser, in accordance with the diagram in Fig. A.7 above.

Figure A.7 and A.8 show the valve system of the *RD-EXC-200* laser. The following abbreviations have been used as labels:

He ... He gas bottle;
HCl ... Gas mixture bottle;
MTUx ... Maintenance units (contain two manometers a pressure control valve and a lock valve);
Vx ... Valves (V1-V4 are located within the laser and can be controlled via the control panel; V5-V9 are located outside and also marked on the photo in Figure A.7 b);
P ... Rotary vane pump;

A.3. Setting up the *Lambda Physik FL3002* Laser - The Short Way

This Chapter provides a description of how to set up the *Lambda Physik FL3002* pulsed dye laser (cf. Section 3.4.2). This is also described in the manual [32]. However some things are not stated very clearly, or are explained in a long and cumbersome way. Therefore this Chapter will provide a scheme to setup this laser as short and exact as possible. The information is mostly based on the manual, only some personal experiences of the author have been incorporated. Since this is basically a summary of the manual, some sentences might be direct quotations.

The manual is structured quite clearly and offers a lot of useful information, the Chapters II to VI-2 are important for the setup. The first part of each Section provides some technical information about the corresponding laser part (pump beam path, oscillator, etc.). At some points complex adjustments are explained in more detail in the manual. A reference to the corresponding page of the manual will be given at these points.

Safety Notes

At any point of this description, if not stated otherwise: Make sure that the pump laser (in this case the *Radiant Dyes RD-Exc-200*) is set to a low frequency (1 Hz or 10 Hz) and to a low power (80-100 mJ). Of course all other safety precautions (safety goggles, watch out for reflexes) also apply. At any point you can lower the intensity of the pump beam by swinging in the attenuators (AT1 and AT2 in Figure A.9). Use them at your own judgement, do not strictly refer to the manual for this, sometimes the laser beam can not be seen properly if the attenuators are swung in.
Concerning safety goggles: It might be necessary to take them off in the first part of the alignment since the beam is too weak to see with goggles, however they should be worn at the latest when adjusting the main amplifier.

Description of the Elements of the *Lambda Physik* Dye Laser, as Indicated in figure A.9:

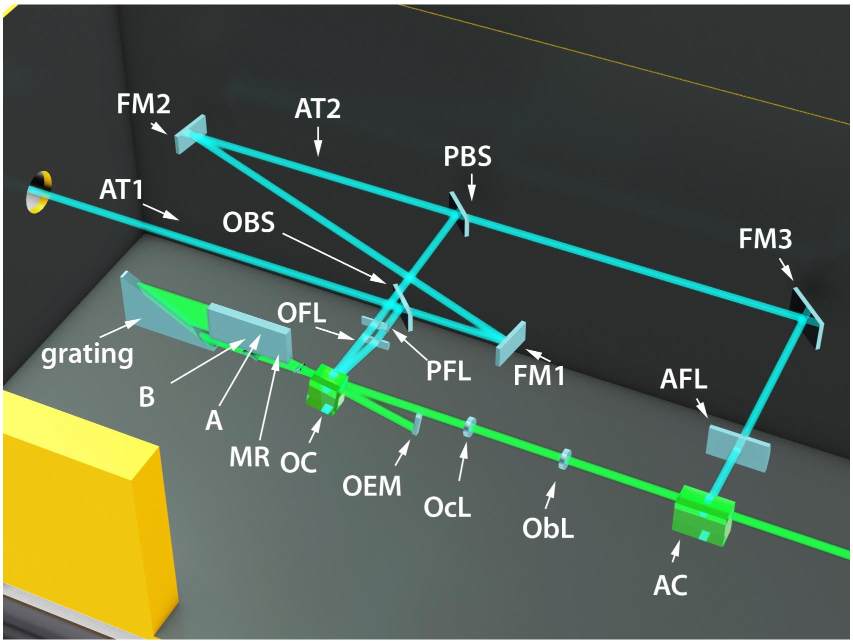

Figure A.9.: CAD drawing of the *Lambda Physik FL3002* dye laser. The single elements are marked and explained in the text below and in Section 3.4.2. A schematic of the Resonator itself is shown in Figure 3.9 in Section 3.4.2.

FM1-3	...	folding mirrors;
AT1-2	...	attenuators;
A,B	...	prism beam expander controls, A tilts the whole platform, B only the exit prism
OC	...	oscillator cuvette and/or its crate;
OBS	...	oscillator beam splitter;
OFL	...	oscillator focussing lens;
PBS	...	preamplifier beam splitter;
PFL	...	preamplifier focussing lens;
AFL	...	amplifier focussing lens;
AC	...	amplifier cuvette and/or its crate;
MR	...	monitor reflex;
OEM	...	oscillator end mirror;
ObL	...	objective lens;
OcL	...	ocular lens;

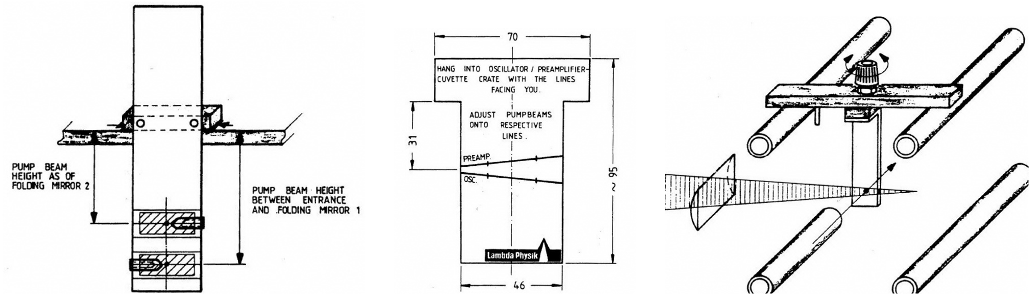

(a) (b) (c)

Figure A.10.: Beam tools necessary for the alignment of the *Lambda Physik FL3002* dye laser (from [32]).

A.3.1. Pump Beam Setup

At first the pump beam has to be aligned, this is described in Section II-3 on page 20 of the manual [32]. Note: this is not necessary when the only the dye is changed. The following steps have to be performed:

1. The dye laser setup should be aligned as parallel as possible to the pump beam and the pump beam has to enter the dye laser setup unobstructed.
2. Remove both cuvettes from their crates.
3. Block the pump beam before it enters the dye laser setup. Exchange FM1 by the pump beam tool a (cf. Figure A.10 a), remove the beam blocker and adjust the pump beam so that it hits the lower mark of the pump beam tool at its center.
4. Block the pump beam; set FM1 back in and exchange FM2 with the pump beam tool. Unblock the pump beam and adjust FM1 so that the it hits the upper mark of the pump beam tool at its center.
5. Block the pump beam; set FM2 back in and hang the pump beam tool on the amplifier plate between the two lines (along the pump beam path in front of FM3). Unblock the pump beam and adjust FM2 so that the it hits the upper mark of the pump beam tool at its center.

   Now the pump beam has to be aligned so that it hits the cuvettes at the correct height.
6. Insert the card shown in Figure A.10 b) into the crate of the oscillator cuvette (OC) so that the lines are facing you and use the V (vertical) and H (horizontal) controls of the OBS and the H and R (rotation) controls of the OFL alternately to align the pump beam with the lower line on the card, then bring the pump beam down about 5 mm below this line (empirical value). Make sure that the pump beam still hits the OFL approximately at its center, this can be tested by loosening the M5 screw holding the OFL in place and shifting the lens back and forth. The pump beam should not move but only become more and less focused. If this is not the case it does not hit the OFL at its center.
7. Repeat the last point for the preamplifier beam, using the corresponding beam splitter (PBS) and focusing lens (PFL).
8. Use the beam tool c (cf. Figure A.10 c) to align the beam tool at the main amplifier. Hang the tool on the two upper rods of the 4-rod optical bench, into the main amplifier crate (AC) and align the pump beam with the control of FM3 and AFL so that it hits the beam tool at the pinhole.

A.3.2. Oscillator Setup

In order to properly understand the oscillator it is recommended to read through Section III of the manual [32], page 24. Appendix A of this work also holds some interesting information. The alignment is done as follows:

1. Block the pump beam and install the oscillator dye cuvette into the crate (OC). Tune the laser to the lasing maximum of the dye used. Make sure the output of the laser setup is closed.
2. Block the preamplifier pump beam by hanging pump beam tool a) in front of the PFL with the short leg. Also block the main amplifier pump beam.
3. Unblock the pump beam, if the adjustments of the pump beam were done correctly, the laser should work immediately. A light ribbon with speckle should appear on the grating and the monitor reflex should appear at the location indicated in Figure A.9 (MR). Adjust the height of OFL if the laser does not work.
4. If the laser still does not work check if the correct wavelength is set and if the oscillator end mirror (OEM) has been set to the correct wavelength range (red-610-860 nm, silver-420-640 nm, blue-320-450 nm). Also check if the pump beam has been aligned correctly (step 6 of the pump beam alignment).
5. This point is unfortunately a little tricky. However, by the personal experience of the author its effect is not very significant. The point of this step is to separate the actual laser light of the cavity and the light coming from amplified spontaneous emission. Swing in AT1, and slide a piece of stiff paper between the cuvette (OC) and the output mirror (OEM) from below until the monitor reflex just disappears. Now turn the R-control of OFL, until it looks like in Figure A.11 a). If done correctly the reflex of the cuvette window as well as the fluorescence of the pumped region indicated in Figure A.11 a) should have decreased in intensity.
6. Hang the pump beam tool b into the 4-rod optical bench between the oscillator and the ocular lens (OcL). Use the knob A (indicated in Figure A.9) to obtain a reflex like in Figure A.11 b).
7. Adjust knob B and the focus and height of OCL so that the monitor reflex reaches its highest intensity and contrast.
8. Carefully move the grating manually from maximum to threshold emission, the monitor reflex should remain steady, if not adjust knob B until it does.
9. The last two steps might have altered the reflex of the laser beam on the beam tool, if this is the case repeat the last three steps. Out of personal experience the best adjustment seems to be achieved when the middle reflex of the three reflexes visible on the beam tool (cf. Figure A.11 b) is the strongest (turning A, changes the intensity of the reflexes).

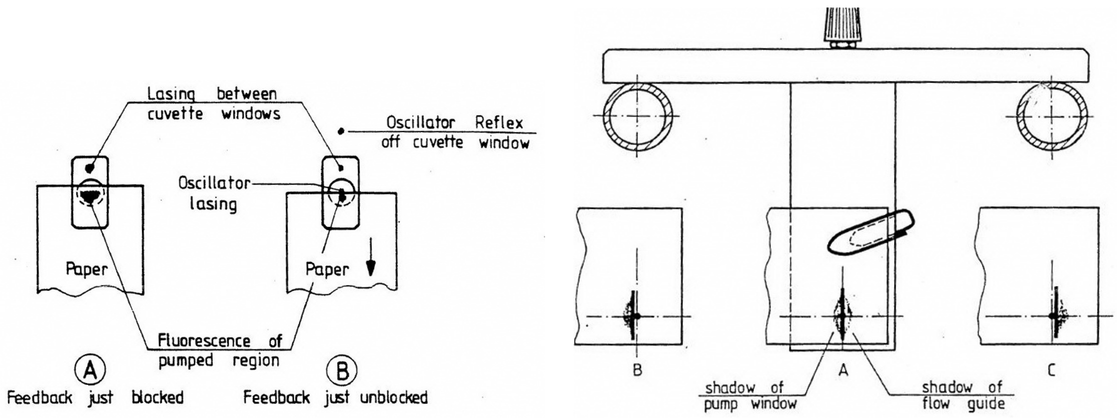

(a) (b)

Figure A.11.: Alignment of the oscillator (from [32]).

A.3.3. Preamplifier

1. Swing in AT1 and AT2.
2. Hang the beam tool c) in front of the main amplifier. (The main amplifier pump beam is still blocked.)
3. Unblock the preamplifier pump beam.
4. Probably both attenuators have to be swung out to see the laser beam. Unblocking the preamplifer beam should result in a much brighter spot on the beam tool. Mostly this can not be seen in the beginning, since the preamplifier pump beam is set to high. Adjust with the H-control of PFL. Once the bright spot of the preamplifier can be seen, alternately block and unblock the preamplifier pump beam and overlap the dye laser beam and the preamplifier beam. The picture on the beam tool should still resemble the one in Figure A.11 b). If it does not, steps 6-8 of the oscillator setup might have to be repeated.
5. Shift PFL. The preamplifier output should not move, if it does PFL and PBS alignments have to be corrected. If the preamplifier output moves up, turn the V-control of the PFL cw and then the V-control of the PBS cw to bring the beam back to its original height. Repeat this step until the preamplifier output does not move anymore.

A.3.4. Intermediate Telescope

1. Hang the beam tool c in behind the objective lens in the direction of the beam. Use the H and V-control of the ocular lens (OcL) to position the beam on the pinhole of the beam tool.
2. Hang the beam tool c in at the very end of the 4-rod optical bench. Use the H and V-control of the objective lens (ObL) to position the beam on the pinhole of the beam tool.
3. Repeat these two steps until proper alignment is achieved.

A.3.5. Main Amplifier

1. Use goggles.
2. Block the pump beam.
3. Swing in AT2.
4. Insert the main amplifier cuvette (AC).
5. Place the beam tool c at the very end of the optical bench.
6. Unblock the pump beam (the main amplifier pump beam remains blocked)
7. Turn the H-control of OcL ccw until it hits the shadow of the pump window.
8. Move the beam tool in front of the main amplifier in beam direction. Draw a vertical line at the preamplifier output.
9. Move the beam tool back to the very end of the optical bench and us the H-control of ObL to bring the beam on the vertical line.
10. Make sure that the output of the dye laser setup is blocked and unblock the main amplifier pump beam.
11. Adjust the height of AFL for maximum brightness.
12. Adjust the H-control of ObL for maximum brightness and beam shape.

A.3.6. Power Optimization

The optimization of the output energy is basically performed by following the steps of the alignment. The best method to measure the output power is to use put a dispersing lens and a Joulemeter in front of the laser output and connect the Joulemeter to an oscilloscope. In short the steps to maximize the power are:

1. Adjust the focus and height of the preamplifier (PFL), defocus by 2-5 mm in the direction of the cuvette to improve the background performance.
2. Adjust the tilt of PFL, this will be insensitive over a large range, tilt the lens until the output starts to drop.
3. Alternately adjust A and B for maximum output. For every change in A, change B for maximum intensity and contrast of the monitor reflex.
4. Swivel the cuvette with an allenhead driver (does usually not have a lot of effect).
5. Adjust the height, tilt and focus of the main amplifier pump beam with the help of AFL.
6. Turn the H-control of Ocl and ObL alternately until maximum output is achieved.
7. Take a burn pattern of the laser (use a marker to blacken a piece of paper) 1-2 cm behind the amplifier. It should resemble the sketch in Figure A.12

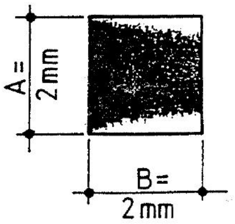

Figure A.12.: Burn pattern of the *Lambda Physik FL3002* dye laser. If A is narrower the focus is too tight, if B is shorter the dye concentration is too high (from [32]).

APPENDIX B

Common Errors

When working in a laboratory naturally errors occur from time to time. Many errors can be solved quickly and easily thanks to the experience of colleagues who have been working in the laboratory for some time. Without this experience one would spend a long time looking for the cause and solution of these errors. Hence, in this Chapter, a list of (common) errors and their solution are given.
Good luck!

- *No helium beam:* Check if the QMS is in correct mode of operation (manual/computer);
- *LastTrig7 does not work properly:* Check if the BNC cable loop is closed (resistance at open ends);
- *MCA does not work properly:* Check RS232 connection;
- *Helium beam signal of QMS is too low:* The nozzle might be frozen, another indicator for this is that the pressure in the fore-vacuum pipe is low (i.e., if it is clearly below $5.8 \cdot 10^{-2}$ mbar - values only valid for 14 K nozzle temperature and 60 bar helium pressure). If the nozzle is frozen, there is less helium in the chamber, hence the pressure is lower. To solve the problem, turn off the cooling helium, wait for 30 min (let the nozzle warm up) and switch it on again - watch the pressure, if it rises up to about $5.8 \cdot 10^{-2}$ mbar the nozzle should be free again. If not, try again, if it still does not work the apparatus has to be warmed up to room temperature again.
- In case of doubt: Relocate new devices and check some cables.

APPENDIX C

Technical Drawings

Exact technical drawings are important for any device, but especially for a vacuum apparatus, because its inside can not be accessed easily. Thus, a secondary task of this work was to continue and complete the CAD drawings of Florian Lackner, who previously had measured and drawn the detection chamber, including the TOF mass spectrometer and the LIF detector. The complete 2D and 3D drawings can be found on the included data CD. All drawings of the detection and pickup chamber as well as all outer dimensions of the source chamber and the laser setup are on scale. The positions of the laser mirrors, lenses and other optical devices are also on scale. The cooling rod and skimmer within the source chamber are the only things not on scale, since their dimensions could not be measured.

In this Chapter, only the drawings of the pieces which had to be newly constructed in the course of this work are included. The technical drawings are printed on scale (given on the drawing), hence no header and footer could be included, therefore the list below gives a short description of the objects on the drawings.

1. Oven - copper block serving as oven for the alkaline earth metal pickup cell
2. Pickup Cell - alkaline earth metal pickup cell;
3. Flange - suspension of the alkaline earth metal oven;
4. MACOR Disc - thermal insulation of the suspension;
5. Gas Pickup Suspension - new suspension for the gas pickup cell
6. Radiation Shield 1 - shielding the whole oven;
7. Gas Pickup Cell - new and shorter from of the gas pickup cell;
8. Radiation Shield 2 - shielding the alkali metal pickup cell;
9. Copper Feedthrough - feedthrough for the cooling copper cable connected to radiation shield 1;

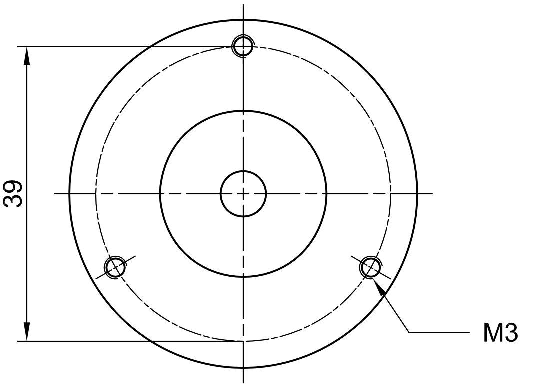

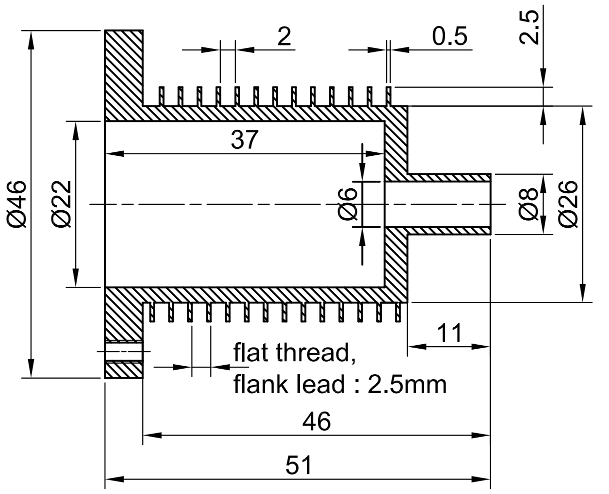

Assembly of Oven and Thermocoax

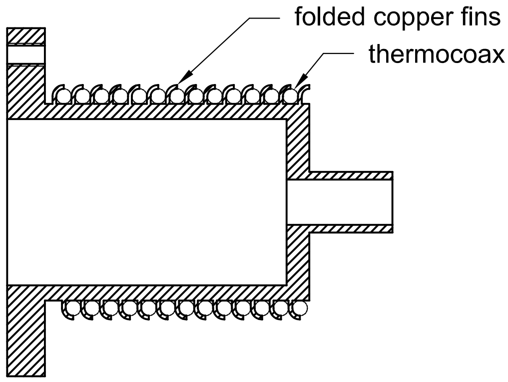

1 Piece

Material: Copper

	Dat.	Name
Editor	2011	Krois

Scale
1:1

Pickup Oven

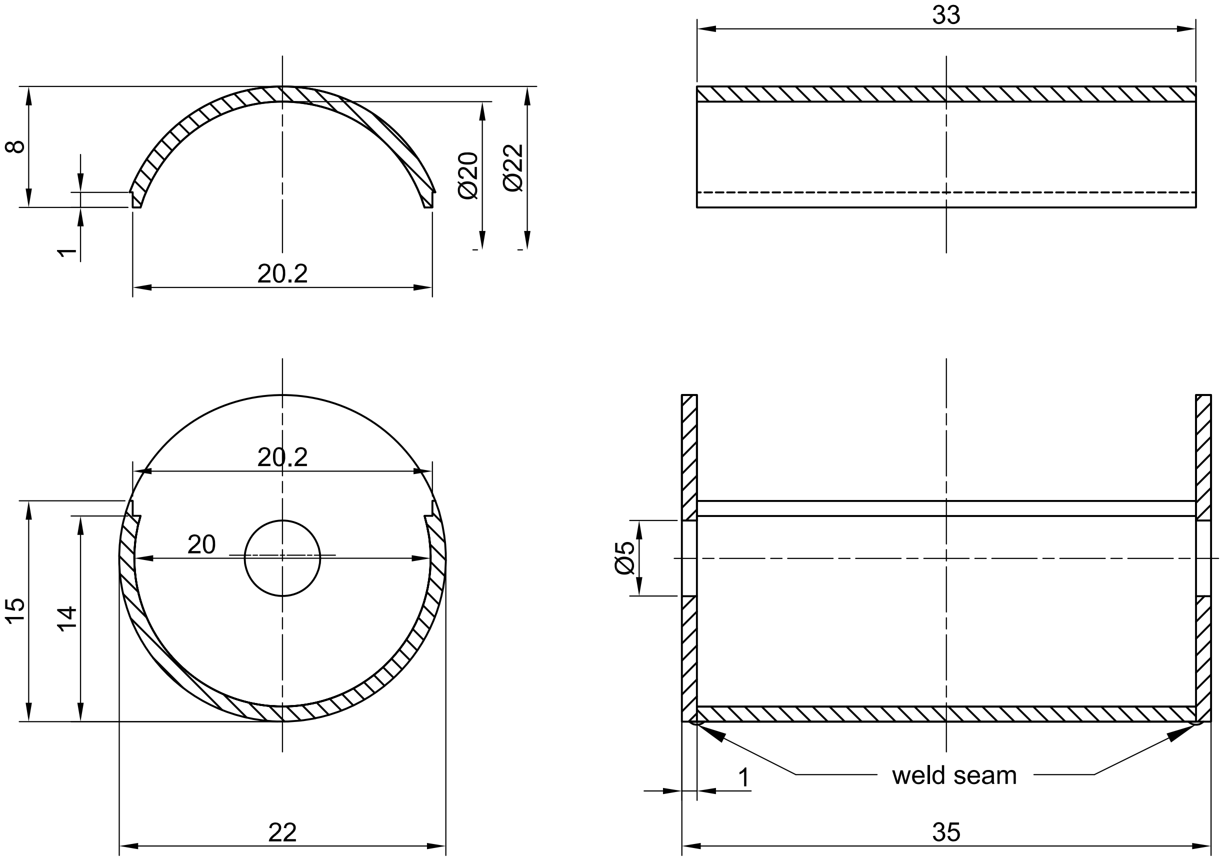

1 Piece

Material: Copper

	Date	Name
Editor	2010	Krois

Scale
2:1

Pickup Cell

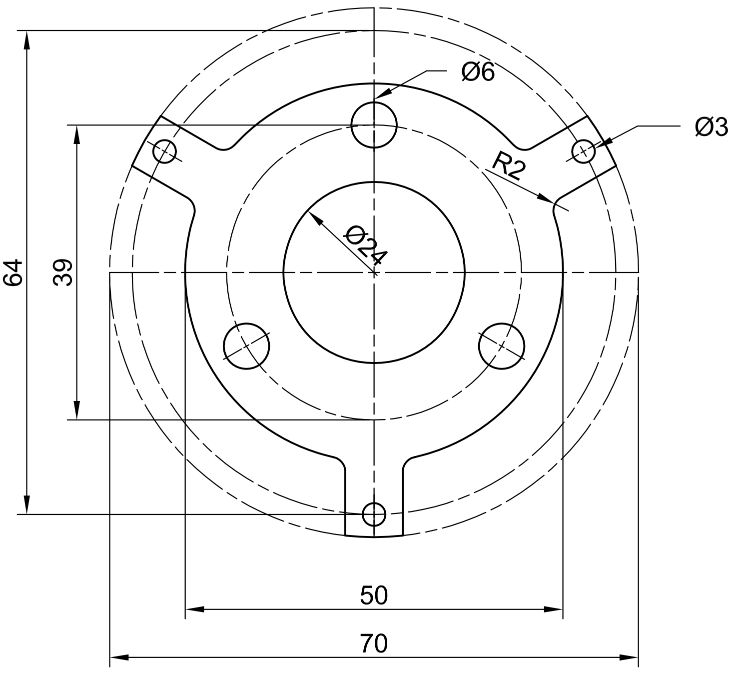

1 Piece

Material: High quality steel

	Date	Name
Editor	2010	Krois

Thickness: 2mm

Scale
1:1

Flange

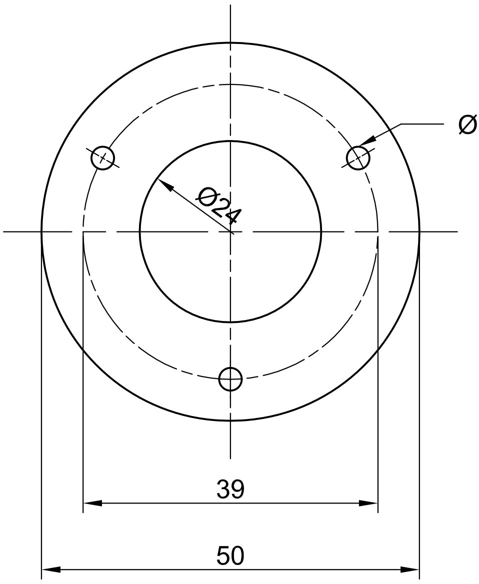

1 Piece				Material: Macor-ceramics	

	Date	Name	
Editor	2011	Krois	Thickness: 3mm

Maßst.
1:1

Macor Disc

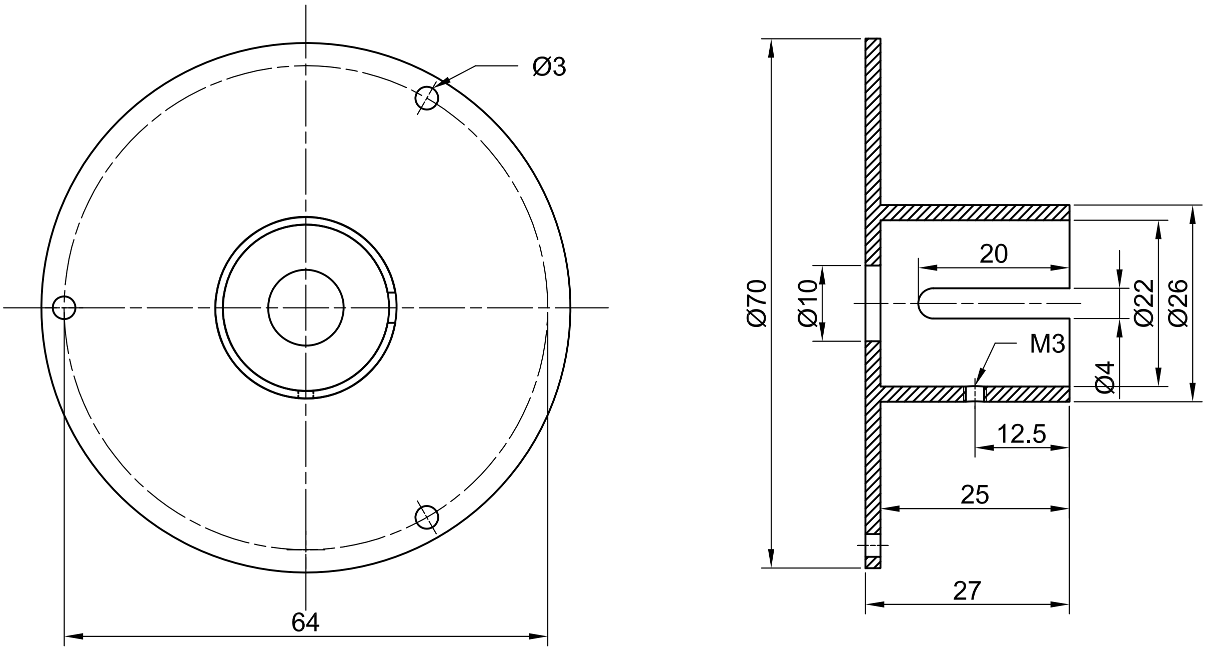

1 Piece				Material: High quality steel	

	Date	Name
Editor	2011	Krois

Scale
1:1

Gas Pickup Suspension

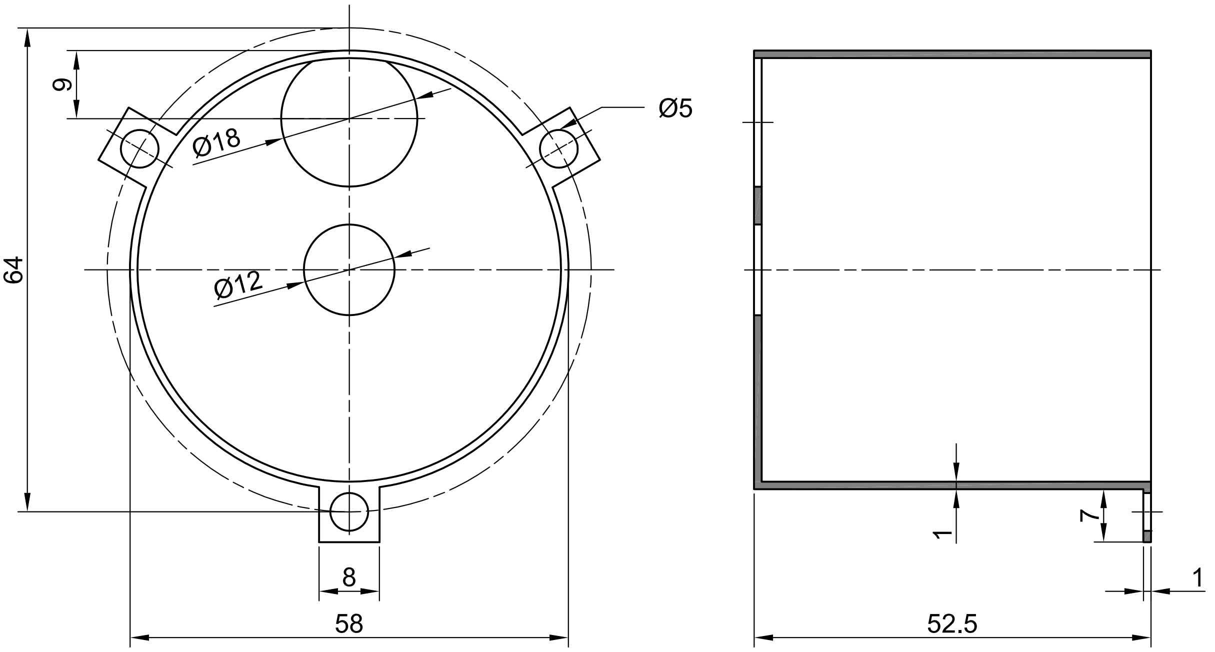

1 Piece				Material: Polished copper	

	Date	Name
Editor	2011	Krois

Thickness: 0.5 mm

Scale
1:1

Radiation Shield 1

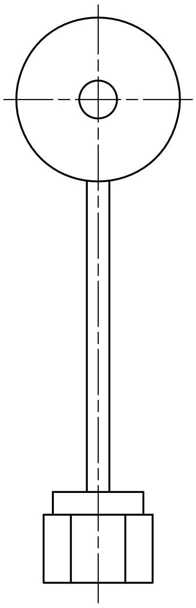

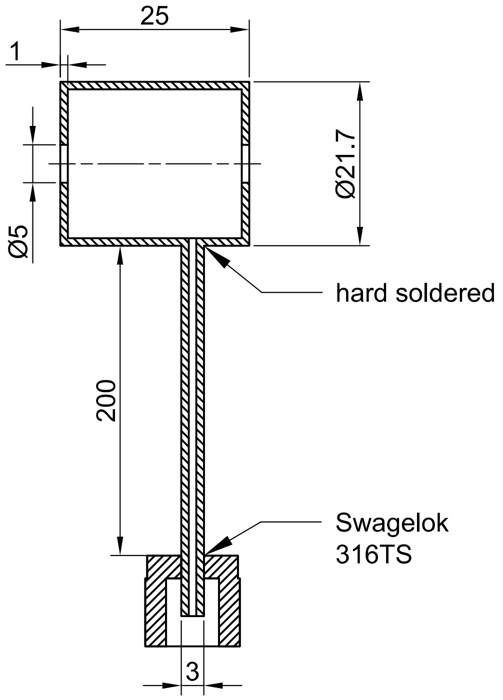

1 Piece

Material: High quality steel

	Date	Name
Editor	2011	Krois

Scale
1:1

Gas Pickup Cell

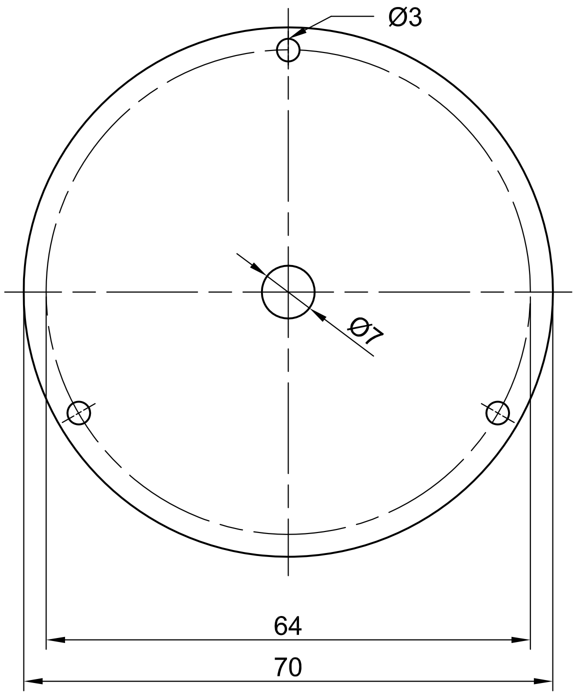

1 Piece

Material: polished copper

	Date	Name
Editor	2011	Krois

Thickness: 1mm

Scale.
1:1

Radiation Shield 2

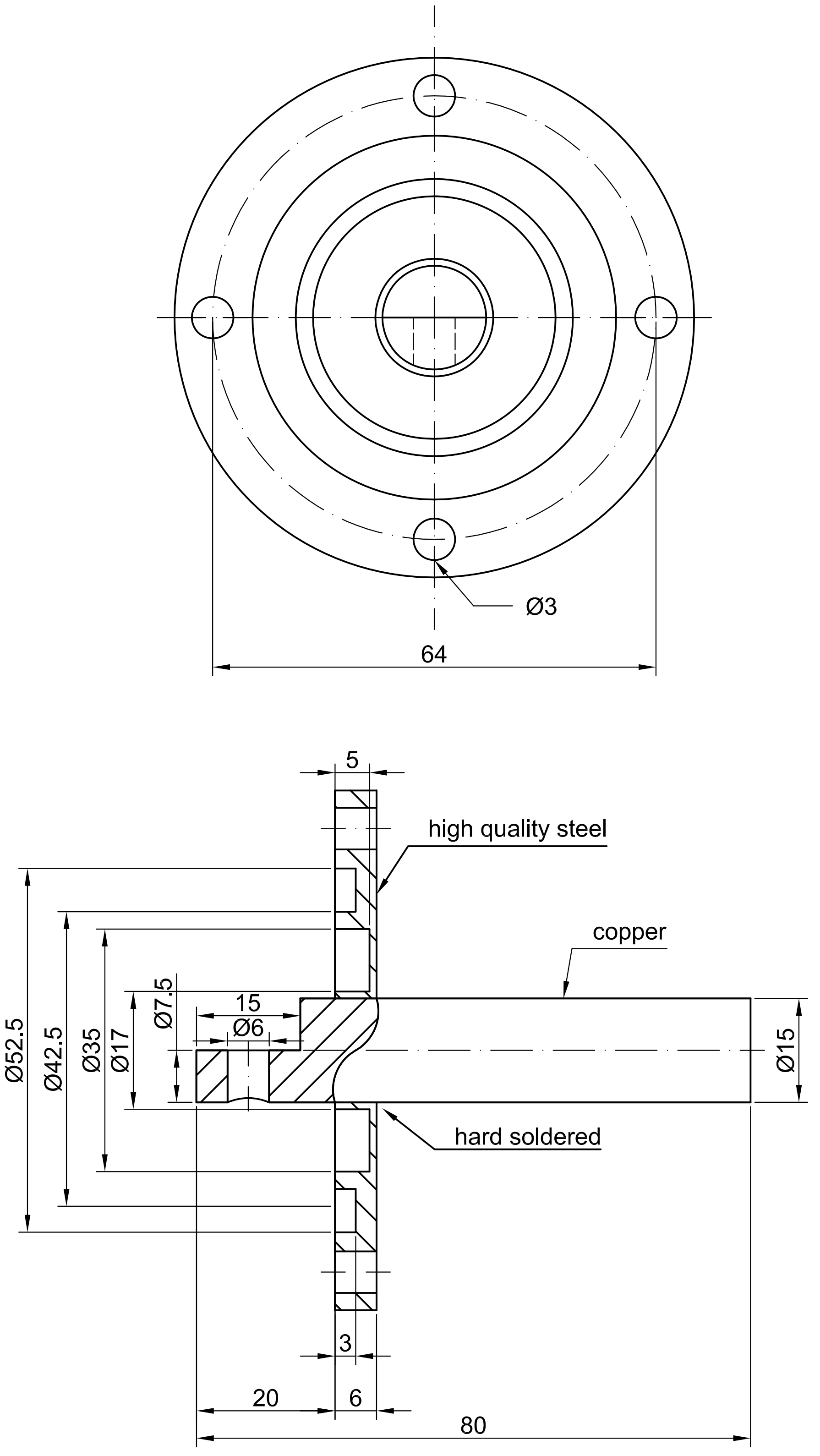

1 Piece	Material: Copper / high quality steel

	Date	Name
Editor	2011	Krois

Scale
1:1

Copper Feedthrough

List of Figures

List of Tables

Bibliography

[1] J. Allen and D. Misener. Flow of Liquid Helium II. *Nature*, 141:75, 1938.

[2] P. Atkins. *Molecular Quantum Mechanics.* Oxford University Press, 1983.

[3] G. Aubock, J. Nagl, C. Callegari, and W. E. Ernst. Electron spin pumping of Rb atoms on He nanodroplets via nondestructive optical excitation. *Physical Review Letters*, 101(3):035301, July 2008.

[4] E. W. Becker, K. Bier, and W. Henkes. Strahlen aus kondensierten Atomen und Molekülen im Hochvakuum. *Zeitschrift Fur Physik*, 146(3):333–338, 1956.

[5] S. Bergmann. *Lehrbuch zur Experimentalphysik Band 4.* Gruyter, 1998.

[6] Bernhard Halle Nachfolger GmbH. Glan-Polarisationsprismen für Hochleistungslaser. Website, 2011. Available online at `www.b-halle.de`; visited on July 1$^{\text{st}}$ 2011.

[7] C. Callegari and F. Ancilotto. Perturbation Method to Calculate the Interaction Potentials and Electronic Excitation Spectra of Atoms in He Nanodroplets. *J. Phys. Chem. A*, J. Peter Toennies Festschrif, March 24 2011. Special Issue: J. Peter Toennies Festschrift Received: November 22, 2010 Revised: March 7, 2011.

[8] C. Callegari and W. E. Ernst. *in Handbook of High-resolution Spectroscopy.* Wiley-VCH, 1st ed., 2011. Vol. 3, , p. 1551-1594.

[9] A. Conjusteau. *Spectroscopy in Helium Nanodroplets: Studying Relaxation Mechanisms in Nature's Most Fascinating Solvent.* PhD thesis, Princeton University, NJ USA, 2002.

[10] W. Demtröder. *Molekülphysik: Theoretische Grundlagen und experimentelle Methoden.* Oldenbourg, 2003.

[11] W. Demtröder. *Experimentalphysik 2 - Elektrizität und Optik.* Springer, 2009.

[12] R. J. Donnelly. The two-fluid theory and second sound in liquid helium. *Physics Today*, 62(10):34–39, Oct. 2009.

[13] R. J. Donnelly. The Discovery of Superfluid Helium. *Physics Today*, pages 30–35, July 1995.

[14] R. P. Feynman. Superfluidity and Superconductivity. *Reviews of Modern Physics*, 29(2):205–212, 1957.

[15] T. Fliessbach. *Statistische Physik; Lehrbuch zur Theoretischen Physik IV.* Spektrum, 2010.

[16] M. A. Gaveau, J. M. Mestdagh, T. Bouissou, G. Durand, M. C. Heitz, and F. Spiegelman. Evidence for a non-Rydberg molecular doubly excited state of Ca-2. *Chemical Physics Letters*, 467(4-6):260–264, Jan. 2009.

[17] B. Glück. *Strahlungsheizung - Theorie und Praxis.* Verlag C.F. Müller Karlsruhe, 1982. ISBN: 3-7880-7157-5.

[18] T. E. Gough, M. Mengel, P. A. Rowntree, and G. Scoles. Infrared spectroscopy at the surface of clusters: SF6 on Ar. *Journal of Chemical Physics*, 83:4958, 1985.

[19] S. Goyal, D. L. Schutt, and G. Scoles. Vibrational spectroscopy of sulfur-hexafluoride attached to helium clusters. *Physical Review Letters*, 69(6):933–936, Aug. 1992.

[20] S. Goyal, D. L. Schutt, and G. Scoles. Infrared-spectroscopy in highly quantum matrices - vibrational-spectrum of (SF6)n=1,2 attached to helium clusters. *Journal of Physical Chemistry*, 97(10):2236–2245, Mar. 1993.

[21] S. Grebenev, B. Sartakov, J. P. Toennies, and A. F. Vilesov. Evidence for superfluidity in para-hydrogen clusters inside helium-4 droplets at 0.15 kelvin. *Science*, 289(5484):1532–1535, Sept. 2000.

[22] S. Grebenev, J. P. Toennies, and A. F. Vilesov. Superfluidity within a small helium-4 cluster: The microscopic Andronikashvili experiment. *Science*, 279(5359):2083–2086, Mar. 1998.

[23] M. Hartmann, R. E. Miller, J. P. Toennies, and A. Vilesov. Rotationally Resolved Spectroscopy of SF6 In Liquid-helium Clusters - A Molecular Probe of Cluster Temperature. *Physical Review Letters*, 75(8):1566–1569, Aug. 1995.

[24] A. Hernando, R. Mayol, M. Pi, M. Barranco, F. Ancilotto, O. Bunermann, and F. Stienkemeier. The structure and energetics of He-3 and He-4 nanodroplets doped with alkaline earth atoms. *Journal of Physical Chemistry A*, 111(31):7303–7308, Aug. 2007.

[25] L. Kapitza. Viscosity of liquid helium below the λ-point. *Nature*, 141, 1938.

[26] J. Kinast, S. Hemmer, M. E. Gehm, A. Turlapov, and J. E. Thomas. Evidence for Superfluidity in a Resonantly Interacting Fermi Gas. *Phys. Rev. Lett.*, 92:150402, 2004.

[27] M. M. Kleinekathöfer U.; Lewerenz M. Long Range Binding in Alkali-Helium Pairs. *Physical Review Letters*, 83:4717–4720, 1999.

[28] S. Kotochigova and P. Julienne. NIST Potential Energy Surface Database of Group II Dimer Molecules. Website, Aug. 2010. Available online at `http://physics.nist.gov/PhysRefData/PES/RefData/Sr.html`; visited on August 26th 2011.

[29] K. J. Kuhn. *Laser Engineering.* Prentice Hall, Inc., 2008.

[30] F. Lackner. Laserspektroskopie und Flugzeitmassenspektrometrie an Rubidium-dotierten Heliumnanotröpfchen. Master's thesis, Graz University of Technology, 2009.

[31] F. Lackner, G. Krois, M. Theisen, M. Koch, and W. E. Ernst. Spectroscopy of nS, nP and nD Rydberg series of Cs atoms on helium nanodroplets. *Physical Chemistry Chemical Physics*, in press, 2011.

[32] Lambda Physik. *Lambda Physik AG; FL3002 Dye Laser Manual.* Lambda Physik AG, Hans-Böckler-Str. 12 37079 Göttingen Germany. www.lambdaphysik.com.

[33] L. Landau. Theory of the Superfluidity of Helium II. *Physical Review*, 60:356, 1941.

[34] J. Lanzersdorfer. Assembly and Test of a Helium Cluster Beam Apparatus for Magnetic Field Studies of Atom and Molecule Doped Helium Nanodroplets. Master's thesis, Graz University of Technology, 2008.

[35] K. K. Lehmann and G. Scoles. Superfluid helium - The ultimate spectroscopic matrix? *Science*, 279(5359):2065–2066, Mar. 1998.

[36] M. Lewerenz, B. Schilling, and J. P. Toennies. A New Scattering Deflection Method For Determining and Selecting the Sizes of Large Liquid Clusters of He-4. *Chemical Physics Letters*, 206(1-4):381–387, Apr. 1993.

[37] D. R. Lide. *CRC Handbook of Chemistry and Physics, 84th Edition.* CRC Press. Boca Raton, 2003.

[38] E. Loginov, C. Callegari, F. Ancilotto, and M. Drabbels. Spectroscopy on Rydberg States of Sodium Atoms on the Surface of Helium Nanodroplets. *J. Phys. Chem. A*, 115:6779–88, 2011.

[39] D. E. Milligan and M. E. Jacox. Infrared Spectroscopic Evidence For Species Hnc. *Journal of Chemical Physics*, 39(3):712–&, 1963.

[40] D. E. Milligan and M. E. Jacox. Infrared Spectroscopic Evidence For Species Ho2. *Journal of Chemical Physics*, 38(11):2627–&, 1963.

[41] C. Mortimer and U. Müller. *Chemie; Das Basiswissen der Chemie.* Thieme, 2003.

[42] J. Nagl. Aufbau und Test einer Duesenstrahlapparatur zur Spektroskopie an alkalimetalldotierten Edelgasclustern. Master's thesis, Graz University of Technology, 2004.

[43] H. Pauly. *Atom, Molecule, and Cluster Beams 1: Basic Theory, Production and Detection of Thermal Energy Beams.* Springer, 2000.

[44] H. Pauly. *Atom, Molecule, and Cluster Beams II: Cluster Beams, Fast and Slow Beams, Accessory Equipment and Applications.* Springer, 2000.

[45] A. Pifrader. Pulsed laser spectroscopic investigations of rubidium atoms attached to helium nanodroplets. Master's thesis, Graz University of Technology, 2009.

[46] A. Pifrader, O. Allard, G. Aubock, C. Callegari, W. E. Ernst, R. Huber, and F. Ancilotto. One- and two-photon spectroscopy of highly excited states of alkali-metal atoms on helium nanodroplets. *Journal of Chemical Physics*, 133(16):164502, Oct. 2010.

[47] A. Przystawik, S. Gode, T. Doppner, J. Tiggesbaumker, and K. H. Meiwes-Broer. Light-induced collapse of metastable magnesium complexes formed in helium nanodroplets. *Physical Review A*, 78(2):021202, Aug. 2008.

[48] Radiant Dyes. *Radiant Dyes Laser Accessories GmbH; RD-EXC-200 Excimer Laser Manual.* Radiant Dyes Laser Accessories GmbH.

[49] M. Ratschek, M. Koch, and W. E. Ernst. Doping helium nanodroplets with high temperature metals: Formation of Cr clusters. *in preparation*, 2011.

[50] J. Reho, U. Merker, M. R. Radcliff, K. K. Lehmann, and G. Scoles. Spectroscopy of Mg atoms solvated in helium nanodroplets. *Journal of Chemical Physics*, 112(19):8409–8416, May 2000.

[51] Y. Ren and V. V. Kresin. Surface location of alkaline-earth-metal-atom impurities on helium nanodroplets. *Physical Review A*, 76(4):043204, Oct. 2007.

[52] G. Scoles. *Atomic and Molecular Beam Methods Volume 1.* Oxford University Press, 1988.

[53] G. Scoles. *Atomic and Molecular Beam Methods Volume 2.* Oxford University Press, 1988.

[54] Sigma-Aldrich Co. LLC. Sigma Aldrich. Website, 2011. Available online at `www.sigmaaldrich.com`; visited on August 15th 2011.

[55] P. Sindzingre, M. L. Klein, and D. M. Ceperley. Path-integral Monte-carlo Study of Low-temperature He-4 Clusters. *Physical Review Letters*, 63(15):1601–1604, Oct. 1989.

[56] F. Stienkemeier, J. Higgins, C. Callegari, S. I. Kanorsky, W. E. Ernst, and G. Scoles. Spectroscopy of alkali atoms (Li, Na, K) attached to large helium clusters. *Zeitschrift Fur Physik D: Atoms Molecules and Clusters*, 38(3):253–263, Oct. 1996.

[57] F. Stienkemeier, J. Higgins, W. E. Ernst, and G. Scoles. Laser Spectroscopy of Alkali-doped Helium Clusters. *Physical Review Letters*, 74(18):3592–3595, May 1995.

[58] F. Stienkemeier and K. K. Lehmann. Spectroscopy and dynamics in helium nanodroplets. *Journal of Physics B-atomic Molecular and Optical Physics*, 39(8):R127–R166, Apr. 2006.

[59] F. Stienkemeier, F. Meier, and H. O. Lutz. Alkaline earth metals (Ca, Sr) attached to liquid helium droplets: Inside or out? *Journal of Chemical Physics*, 107(24):10816–10818, Dec. 1997.

[60] F. Stienkemeier, F. Meier, and H. O. Lutz. Spectroscopy of barium attached to superfluid helium clusters. *European Physical Journal D*, 9(1-4):313–315, Dec. 1999.

[61] M. Theisen, F. Lackner, F. Ancilotto, C. Callegari, and W. E. Ernst. Two-step excitation of Rb atoms on He nanodroplets. *European Physical Journal D*, 61(2):403–408, Jan. 2011.

[62] M. Theisen, F. Lackner, and W. Ernst. Cs atoms on helium nanodroplets and the immersion of Cs^+ into the nanodroplet. *Journal of Chemical Physics*, 135:074306, 2011.

[63] M. Theisen, F. Lackner, and W. E. Ernst. Forming Rb^+ snowballs in the center of He nanodroplets. *Physical Chemistry Chemical Physics*, 12(45):14861–14863, 2010.

[64] J. Tiggesbaumker and F. Stienkemeier. Formation and properties of metal clusters isolated in helium droplets. *Physical Chemistry Chemical Physics*, 9(34):4748–4770, 2007.

[65] L. Tisza. Transport phenomena in helium II. *Nature*, 141:913–913, Jan. 1938.

[66] J. P. Toennies and A. F. Vilesov. Superfluid helium droplets: A uniquely cold nanomatrix for molecules and molecular complexes. *Angewandte Chemie-international Edition*, 43(20):2622–2648, 2004.

[67] J. P. Toennies, A. F. Vilesov, and K. B. Whaley. Superfluid helium droplets: An ultracold nanolaboratory. *Physics Today*, 54(2):31–37, Feb. 2001.

[68] L. Vegard. Light emitted from solidified gases and its relation to cosmic phenomena. *Nature*, 114:357–359, July 1924.

[69] E. Whittle, D. A. Dows, and G. C. Pimentel. Matrix Isolation Method For the Experimental Study of Unstable Species. *Journal of Chemical Physics*, 22(11):1943–1943, 1954.

Acknowledgements

This section is... personal, so I will allow myself to let go of the strict technical formalism here and write more freely: At first, of course, I want to thank my supervisor Prof. Ernst. Thank you, for taking me up in your group and giving me the chance to do this interesting thesis. (The fact that I will stay for the next three years in the same group may be taken as a proof that this is not only a flowery phrase.) It is pleasure to work in your group.

Next I need to thank Flo. Without you I still wouldn't know how half of the things in our Lab work and I still would be far from finished. It is really inspiring to work with you. Besides: It's fun! Bist a guata Chef!
Special thanks also to Markus, for taking time for me whenever I had questions. And they were as various as numerous. Thanks for your patience, may it last!
Another special thanks to Rupert! Without you this whole work would have been quite theoretical.
I would also like to thank Prof. Windholz and Prof. Leisch for their helpful experimental advices.

Then I would like to thank the whole group of the Institute of Experimental physics: Alex, Martin, Michi, Mike, Moritz, Patrick and Toni (in alphabetical order, so that nobody feels offended) Thanks for always having an open ear to listen to my problems... and for sometimes solving them. Thanks for the food and the coffee and the muffins and over all, thanks for socializing!

Apart from my friends at work there are some other people I want to thank:
Gernot , thanks for getting me through this study, I'd still be stuck in the very first 'Uebung' without you. And I still wouldn't like Linux.
Babsi, without you, I probably wouldn't even have started with this study. Thinking about it, there are a whole lot of things I wouldn't have done if it wasn't for your advice. Thanks for giving me ideas!

At the bottom of this section, because the pillars supporting a structure are always at the bottom:
To Conny, because without you life beside work would only have been half as much fun. Thanks for the animation!
And finally to Mama und Papa, dafür dass ihr mich immer unterstützt habt, in allem was ich machen wollte. Danke!